A Study of $\nu_\mu \leftrightarrow \nu_\tau$ vs. $\nu_\mu \leftrightarrow \nu_s$ Neutrino Oscillation In Atmospheric Neutrinos Using a K2K Near Detector Measurement

A Dissertation Presented

by

Christopher Michael Mauger

to

The Graduate School

in Partial Fulfillment of the Requirements

for the Degree of

Doctor of Philosophy

in

Physics

State University of New York
at
Stony Brook

December 2002

State University of New York
at Stony Brook

The Graduate School

Christopher Michael Mauger

We, the dissertation committee for the above candidate for the Doctor of Philosophy degree, hereby recommend acceptance of the dissertation.

Dr. Chang Kee Jung
Professor of Physics

Dr. Robert Shrock
Professor of Physics

Dr. Luis Orozco
Professor of Physics

Dr. Laurence Littenberg
Senior Physicist, Brookhaven National Laboratory

This dissertation is accepted by the Graduate School.

Dean of the Graduate School

Abstract of the Dissertation

A Study of $\nu_\mu \leftrightarrow \nu_\tau$ vs. $\nu_\mu \leftrightarrow \nu_s$ Neutrino Oscillation In Atmospheric Neutrinos Using a K2K Near Detector Measurement

by

Christopher Michael Mauger

Doctor of Philosophy

in

Physics

State University of New York at Stony Brook

2002

Super-Kamiokande has reported evidence for $\nu_\mu \leftrightarrow \nu_\tau$ or $\nu_\mu \leftrightarrow \nu_s$ neutrino oscillation from studies of atmospheric neutrinos. One way to distinguish between the two hypotheses is by looking at the neutral current (NC) rate. Single-π^0 production is a clean NC signal in large water Cherenkov detectors for neutrino energies $\sim 1GeV$ like atmospheric neutrinos. Since the energy spectrum of the K2K beam is similar that of atmospheric neutrinos, measurements of π^0 production in the 1 kton water Cherenkov near detector at

K2K are used to lower the systematic error on a $\nu_\mu \leftrightarrow \nu_\tau$ vs. $\nu_\mu \leftrightarrow \nu_s$ atmospheric neutrino analysis at Super–Kamiokande.

For my family.

Contents

List of Figures **xi**

List of Tables **xxii**

Acknowledgements **xxiii**

1 Introduction **1**

1.1 Direct Searches for Neutrino Mass 2

1.2 Neutrino Oscillation Phenomenology 4

1.3 Experimental Evidence for Oscillations 7

1.3.1 Solar Neutrinos 7

1.3.2 Atmospheric Neutrinos 9

1.3.3 LSND 10

1.4 Sterile Neutrinos 11

2 Neutrino Sources **22**

2.1 Atmospheric Neutrinos 22
2.1.1 Primary Cosmic Ray Flux 22
2.1.2 How This Makes neutrinos 23
2.2 K2K Beam 24
2.2.1 How Is It made? 25
2.2.2 How Is It Measured/Calculated? 26

3 Super–Kamiokandeand K2K 1kt Water Cherenkov Detectors 39

3.1 Water Cherenkov Methodology 39
3.2 SK Detector 40
3.2.1 The PMTs 42
3.2.2 The Water System 44
3.2.3 Electronics 45
3.3 1kt Detector 48
3.4 Calibrations 50
3.4.1 PMTs 51
3.4.2 Water transparency: direct, muons 51
3.4.3 Energy Calibration 55

4 Simulation 62

4.1 Coherent Pion Production 63

4.2 Elastic and Quasi-Elastic Scattering 64

4.3 Resonant Single-Meson Production 66

4.4 Multi-π Production and Deep Inelastic Scattering 68

4.5 Nuclear Effect 71

4.6 Detector Simulation 73

5 Data Reduction and Reconstruction 75

5.1 SK Reduction 76

5.1.1 First Reduction 77

5.1.2 Second Reduction 77

5.1.3 Third Reduction 77

5.1.4 Fourth Reduction 79

5.1.5 Scanning 79

5.2 1kt Reduction 79

5.2.1 Good Spills 79

5.2.2 FADC 80

5.3 Reconstruction 80

5.3.1 Vertex Fitting 80

5.3.2 Ring Finding 81

5.3.3 Particle Identification 81

5.3.4 MS Vertex Fitter 83

5.3.5 Momentum Reconstruction 84
5.3.6 FC Selection 84

6 1kt π^0 **89**

6.1 π^0 Events 89
6.2 FC Single Muons 96
6.3 Systematic Uncertainties 97
6.3.1 Particle ID FC μ 100
6.3.2 Particle ID π^0 100
6.3.3 Ring Counting FC μ 102
6.3.4 Ring Counting π^0 103
6.4 Results 104

7 Super–Kamiokande π^0 Analysis **105**

7.1 π^0 Events 105
7.2 FC Single Muons 107
7.3 Systematic Uncertainty on R_{π^0} 109
7.4 Using the 1kt Measurement in SK 110
7.5 Analysis: $\nu_\mu \leftrightarrow \nu_\tau$ vs. $\nu_\mu \leftrightarrow \nu_s$ Discrimination 113

8 Conclusions and Future **117**

8.1 Conclusions 117

8.2 The Near Future 117

8.3 Future 118

Bibliography **119**

List of Figures

1.1 The MAC-E-filter detector [8]. As the β electrons pass through the detector, the magnetic field weakens adiabatically, converting the transverse momentum of the electrons to longitudinal momentum. 13

1.2 The Feynman diagram of the NC interaction which creates the forward scattering potential for ν_{e}, ν_{μ}, and ν_{τ}(as well as the charge conjugates of each). 14

1.3 Since matter contains electrons, there is an additional contribution to the potential for ν_{e} from this CC interaction. There is a similar CC contribution for $\bar{\nu}_{\mathrm{e}}$. 14

1.4 Solar neutrino energy spectrum [16]. 15

1.5 The Super–Kamiokande solar neutrino allowed region. 16

1.6 Atmospheric neutrino zenith angle distribution. The green lines are the fit to these data of the $\nu_\mu \leftrightarrow \nu_\tau$ oscillation hypothesis. The red line is the null hypothesis. 17
1.7 Atmospheric neutrinos 18
1.8 Atmospheric neutrinos 19
1.9 LSND 20
1.10 Super–Kamiokande $\nu_\mu \leftrightarrow \nu_\tau$ vs. $\nu_\mu \leftrightarrow \nu_s$ Discrimination 21

2.1 A Summary of Cosmic ray data with predictions from [34]. The references for the data are: crosses [35], upward triangles [36], open circles [37], vertical diamonds [39], downward triangles [40], circles [41], squares [42], horizontal diamonds [43], downward open triangles [44], upward open triangles [45], open diamonds [46], and open squares [47]. 29
2.2 The fluxes we use at Super–Kamiokande. Honda is from [50] and Bartol is from [51]. 30
2.3 Overview of the K2K experiment. 31
2.4 The beam structure from events recorded in the 1 kt water Cherenkov detector described in Chapter 3. 32
2.5 The pion monitor. 33
2.6 Cherenkov radiation. 34

2.7 The K2K neutrino spectrum from MC studies at low energy and pion monitor data at higher energies. The far/near ratio is a measure of the difference in K2K beam fluxes at Super–Kamiokande (250 km away) and at the near detector array. . 35
2.8 The ionocopter. 36
2.9 The ionocopter data. 37
2.10 The muon monitor. 38

3.1 Super–Kamiokande while being filled in 1996. 40
3.2 Super–Kamiokande. 41
3.3 The Inner PMTs with black sheeting. 42
3.4 The OD PMTs on the top. 43
3.5 The OD PMTs on the side while under water. 44
3.6 The ID PMTs. 45
3.7 The ID PMT Quantum Efficiency. 46
3.8 The water purification system. 47
3.9 Super–Kamiokande DAQ with arrows showing the flow of data. 48
3.10 The K2K Near Detector Array. 49
3.11 1kt Detector. 50
3.12 A sample TQ map. Higher T means earlier time. As light levels increase, hits are earlier and the timing resolution is better. . 52

3.13 The relative gain measurement setup. 53

3.14 The relative gain measurement in 1996. The corrected charge, normalized by the mean is plotted for all PMTs. 54

3.15 Direct water attenuation length measurement apparatus . . . 55

3.16 Water attenuation length results from one set of measurements. 56

3.17 Water attenuation length measurements (points) with the model used in the detector simulation (lines). 57

3.18 Effective observed charge as a function of the path-length. . . 58

3.19 Michel electrons from muon decay. 59

3.20 Low Energy Stopping muons. 60

3.21 High Energy Stopping muons. 61

4.1 The coherent π^0 production cross-sections used in NEUT. The solid line is for CC while the dashed line is for NC. 63

4.2 The quasi-elastic cross-section used in NEUT for neutrinos shown with data from several experiments [64, 65, 66, 67]. 65

4.3 The quasi-elastic cross-section used in NEUT for anti-neutrinos shown with data from several experiments (See Figure 4.2 for data references). 66

4.4 The cross-section for $\nu_\mu + p \rightarrow \mu^- + p + \pi^+$. Data are from [70, 71, 72]. 67

4.5 The cross-section for $\nu_\mu + n \rightarrow \mu^- + p + \pi^0$. (See Figure 4.4 for data references). 68

4.6 The cross-section for $\nu_\mu + n \rightarrow \mu^- + n + \pi^+$. (See Figure 4.4 for data references). 69

4.7 The cross-section for $\nu_\mu + p \rightarrow \nu_\mu + p + \pi^0$. 70

4.8 The cross-section for $\nu_\mu + n \rightarrow \nu_\mu + n + \pi^0$. 71

4.9 The cross-section for $\nu_\mu + n \rightarrow \nu_\mu + p + \pi^-$. (See Figure 4.4 for data references). 72

4.10 The cross-section for $\nu_\mu + p \rightarrow \nu_\mu + n + \pi^+$. 73

4.11 KNO scaling. 74

5.1 Super–Kamiokande event types. 76

5.2 Super–Kamiokande Δ position distribution for the first stage fitter. The upper figure shows FC one-ring events. The lower figure shows FC multi-ring events. 82

5.3 The fit - true vertex distribution for π^0 events in the 1kt. The left figure shows the distribution along the track while the right figure shows the distribution perpendicular to the track. The red line on each shows the mean deviation from the true vertex position, while the blue lines show the resolution around deviation. 83

5.4 The angular deviation from the true direction in radians for π^0 events. The red line shows 1 σ deviation. 84

5.5 The cyan circles represent PMTs. The blue ring is a Cherenkov ring. Red circles denote some of the hit PMTs. By putting circles of a radius characteristic of the pattern expected from a Cherenkov ring emanating from the vertex centered on each hit PMT, we create a constructive interference at the center of the actual Cherenkov ring. 85

5.6 The figure on top shows a single electron, while the one on the bottom shows a single muon. 86

5.7 The 50 ton fiducial volume used for π^0 events is the $4m \times 4m$ cylinder shown in blue. The red lines denote the 25 ton fiducial volume used for FC muons. 87

5.8 The *pomax20deg* distribution for all events passing the reduction in which the reconstruction successfully found a vertex. . 88

6.1 The invariant mass distributions of events with two e-like FC rings for data (black dots) and MC (boxes) in the 1kt detector. The arrows show the invariant mass cut. The MC is normalized to the data by entry. 91

6.2 The figure on the left is the difference of the reconstructed and true opening angle of the gamma rays as a function of momentum. It shows no momentum dependence. The figure on the right is $\frac{\sqrt{1-\cos\left(\theta_{reconstructed}\right)}}{\sqrt{1-\cos\left(\theta_{true}\right)}}$ as a function of momentum. The mean values are also plotted and exhibit a momentum dependence. 92

6.3 The efficiency to reconstruct a single π^0 in the fiducial volume as a function of momentum. 93

6.4 The figure on the left is the true opening angle of the gamma rays vs. the true momentum of the π^0 for events reconstructed as a π^0. The figure on the right is the same for events which were not reconstructed as a π^0. 94

6.5 Momentum ratio and opening angle distribution of the gamma rays. The data are shown as red dots and the MC blue squares. 95

6.6 Distribution of π^0's in the fiducial volume. Data are red dots, MC is shown with blue squares. 96

6.7 The figure on the left is the composition of the π^0 sample by production mode. “Others” is predominantly from CC-induced events. The figure on the right shows events with a π^0 in the final state in blue, and those without in green. 97

6.8 The momentum distribution of the π^0 data and MC samples where the MC is normalized by the data. On the left, the data are shown with the MC with statistical errors for both. On the right, the simulated data are shown by production mode. "Others" is predominantly CC single-pion production. 98

6.9 The angular ($cos\theta$) distribution with respect to the neutrino beam of the π^0 data and MC samples where the MC is normalized by the data. On the left, the data are shown with the MC with statistical errors for both. On the right, the MC is shown by production mode. "Others" is predominantly CC single-pion production. 98

6.10 The FC muon momentum distribution. Red dots are data, blue squares are MC. The data and MC agree well. 99

6.11 The PID likelihood distributions for MC (above) and data (below). Muon-like events are positive, electron-like events are negative. The middle line on each plot shows the nominal cut value. The lines to either side show alternative cuts used to define a systematic error. The total number of FC single-ring muons changes by less than one percent for each case. 101

6.12 The invariant mass distributions for standard cuts on the left, and no-PID cut on the right. The upper figures are for data, while the lower figures are for MC. The continuous lines show the fits for the background and background plus signal. . . . 102

6.13 The invariant mass distributions for standard cuts on the left, and three-ring e-like events on the right. The upper figures are for data, while the lower figures are for MC. The continuous lines show the fits for the background and background plus signal. 103

7.1 The invariant mass distributions of events with two e-like FC rings for data (red dots) and MC (boxes) in Super–Kamiokande. The arrows show the invariant mass cut. The MC is normalized to the live-time of the data. 106

7.2 The π^0 momentum distribution in Super–Kamiokande. The data are shown in red dots and the MC in blue boxes. The MC is normalized to the live-time of the data. 108

7.3 Energy spectrum of neutrinos producing the π^0 samples at SK and K2K. Most of the π^0 sample at K2K comes from neutrinos between 500 and 2500 MeV. The π^0 sample at Super–Kamiokande has a low energy shoulder and a high energy tail from which 20% of the sample originates. The arrows show the region of neutrino energies where the 1kt result is applied. Details are in the text. 111

7.4 The KT composition as a function of neutrino energy. The left figure shows the energy spectrum while the right figure shows the fraction. "Others" is predominantly CC single-pion production. The arrows show the region of neutrino energies where the 1kt result is applied. Details are in the text. 112

7.5 The SK composition as a function of neutrino energy. The left figure shows the energy spectrum while the right figure shows the fraction. "Others" is predominantly CC single-pion production. The arrows show the region of neutrino energies where the 1kt result is applied. Details are in the text. 112

7.6 For maximal mixing, these are the predictions of R_{π^0} for $\nu_\mu \leftrightarrow \nu_\tau$ and $\nu_\mu \leftrightarrow \nu_s$. The R_{π^0} for data is shown with statistical errors only. All of the systematic error is shown on the predictions. The error bars are 1 σ. The empty box on the bar corresponding to the data R_{π^0} is the Super–Kamiokande 95 % confidence limit from the single-ring sample [97, 92]. 115

7.7 The same as Figure 7.6 but without using the result from the 1kt detector. The uncertainties are prohibitive. 116

List of Tables

6.1 π^0 Sample Production Mode 94

6.2 1kt Systematic Uncertainty on R_{π^0} 97

7.1 SK π^0 Sample Production Mode 107

7.2 SK FC μ Sample Production Mode 109

7.3 $R_{\pi^0}^{SK}$ Systematic Error Before 1kt 109

7.4 Cross-Section Uncertainties 110

7.5 $R_{\pi^0}^{SK}$ Systematic Error After 1kt 114

Acknowledgements

When one spends eight years in graduate school, there are many people to thank. Though I will surely only scratch the surface of what should be said, I will try to thank those who have helped me become who I am.

First, I thank my advisor, Chang Kee Jung. He involved me with the most exciting experiments in high energy physics, SK and K2K. It has been an extraordinary time in physics and for me. He has guided me through thick and thin - sometimes with the carrot and others with the stick - to become a physicist. As I continue working in the field, I will strive to emulate his example.

Yoji Totsuka has shown what it means to be the leader of an experiment. While I had always admired his leadership, I came to truly appreciate it in our darkest hour one year ago. Our experiment and our field are better because of him. Ko Nishikawa has been an inspiration, outlasting even the toughest graduate students and always insisting on answers to the important questions.

Hank Sobel and Jim Stone have ably led the U.S. group on SK. I am so grateful to them for involving us in SK. Chang Kee and Jeff Wilkes have led the U.S. group on K2K. Again, to participate in these experiments is a gift.

All of my collaborators have contributed to my development through their discussions, criticisms and humor. On SK, I was in the atmospheric neutrino analysis group and benefited from all of the members, especially Takaaki Kajita, Ed Kearns, Yoshitaka Itow, Masato Shiozawa, Dave Casper, Jun Kameda, Danka Kielczewska, Yoshinari Hayato, Kimihiro Okumura, Kenji Ishihara, Masayuki Etoh, Mark Messier, Yoshihisa Obayashi, Chiaki Yanagisawa, Clark McGrew and Brett Viren. In K2K, I was in the 1 kiloton analysis group, where I worked closely with Yoshitaka, Makoto Miura, Shun'ichi Mine, Clark, Tsuyoshi Nakaya, Issei Kato, Atsuko Ichikawa, Joanna Zalipska, and Shoei Nakayama. Clark, Yoshitaka, Shun'ichi, Shoei and I worked very closely on π^0 analyses. It has been a pleasure.

Makoto Miura and I worked very closely on the water transparency measurement at SK. His disposition was always bright both at work and at karaoke. His friendship has been a source of comfort to me.

Many members outside of these particular analysis groups have been very important for the quality of the analysis. Makoto Sakuda, through his comments and questions, has made this a better analysis. In addition, as the primary organizer of NuInt01, he has got the ball rolling again on neutrino-nucleus interactions which promises to be a fertile field for the next several decades. Chris Walter has also made important contributions to this effort. In addition, because of his intimate knowledge of the ring-finding algorithms, work on π^0 analysis at SK, and general interest in physics he has been a partner in many important discussions. Yoichiro Suzuki and Kenzo Nakamura have always been available for advice and discussions and always make important contributions at analysis meetings. I also hope to emulate their examples as physicists. Masayuki Nakahata has ably led the calibration group at SK. His work-ethic and experimental knowledge are an inspiration to the whole collaboration. I know of nobody who loves doing physics more.

Despite the help from many people, I must make special mention of a few. Yoshitaka Itow has been like an advisor for much of the π^0 work and for many other analysis and detector issues on which we have worked. Some of my fondest moments of doing physics have been standing with him in front of a white board at 2 in the morning working intently on a problem. I have also had many fun episodes discussing the nitty-gritty details of analysis and systematic uncertainty with Clark McGrew. He is the only person I know who makes systematic errors fun. He has guided much of my work. When I was just getting started, Brett Viren showed me the ropes. He taught me the nuts and bolts of software at a physics experiment. If it were not for him, I would still be trying to read data files.

Spending time in Japan has been a pleasure because of the company of many. In the early days, John Flanagan showed me the ropes of working on an experiment and living in Japan. After SK was running, Rob Sanford, Eric Blaufuss, Mark Messier, Matt Earl and I shared rides into the mine, days of hiking, and evenings of "meat, beer and fire".

On SK and on K2K, John Learned has been generous with both his time and his advice. It has been a pleasure sharing a drink and fine physics discussions with him.

Mark Vagins and I have been close friends since the very early days. If there is anyone who can approach adversity with humor it is Mark. The world needs more people like Bill Kropp. He is kind, fun, demanding and hardworking. Bill Kropp, Mark and I have spent more than one evening sipping whiskey and eating a wide assortment of otsumami in Osawano. I look forward to continuing this tradition, as long as there is coordination there.

The social environment at K2K has been fantastic. It would be hard to find a crowd with the work hard, play hard ethic more firmly etched in their brains. Takasumi Maruyama, Takahiro Inagaki, Shun'ichi Mine, Atsumu Suzuki, Chris Walter, Taku Ishida, Makoto Yoshida, June Ho Choi, Eun-Ju Jeon, Asia Zalipska, Taiki Iwashita, Yoshinari Hayato, Takashi Kobayashi, and Mitsuhiro Kohama and others have all been part of this environment. I thank them. Steve Boyd, though sometimes not as social as the rest of the K2K crowd, has been a good friend.

Eric Sharkey has tolerated me badgering him about computer issues for years. He installed linux on the very laptop on which I have written this thesis. At K2K, we became close friends. We discussed physics, commiserated on our many walks around the TRISTAN ring, and bucked each other up when the other was down. In Japan, he even shared some of his Calorie-mate with me. I am fortunate to have his continued friendship.

When I first arrived at Stony Brook, Chiaki Yanagisawa lent me his house. Little did he know it would start a tradition. He has been a generous friend, both in New York and in Japan. I am looking forward to working with him in the future.

Jim Hill has been a friend, advisor and drinking mate since the very early days. I am happy he now has a permanent position and hope the best for him.

Though Kai Martens' time as a SUNYite was not so long, he had been on SK and was already a good friend when he started at our institution. I look forward to working with him again.

There are many students who have worked or are working here at SUNY.

Bjorn Einarsson, Matthew Malek, Megumi Kinoshita, Fumi Kato and Dan Kerr have all been good friends and comrades. I wish them well for the future.

The SUNY group could not function without Joan Napolitano, Alice Dugan, Pat Peiliker and Diane Siegel. Without them I would not have made it.

Many times one is never sure from why one makes certain decisions. Why did I choose one project over the other or one graduate program over the other. The first semester here was very difficult for me. I can say without any doubt without the support and encouragement I had from my advisor, my classical mechanics teacher, George Sterman, and my close friend from Rutgers, Ellen Yang, I would never have continued in this field.

Finally, I would not be who I am without my family and indeed I would not be at all without my parents. From an early age, my parents encouraged me to reach higher and satisfy my curiosity. My grandparents continued to influence my family even after their passings. As my family grew from the traditional to an extended family, I was embraced by new members and have received much support from all of them. I give my thanks and my love to all of you.

Chapter 1

Introduction

Of all the known particles in the universe, we know the least about neutrinos. They are extremely light and do not interact via electromagnetic interactions making them quite difficult to detect at all. Their discovery by Reines and Cowan [1] came twenty-five years after they were first postulated by Wolfgang Pauli to solve a problem with nuclear β-decay [2]. At the time, there were three known nuclear decay processes labelled α, β and γ. The first process occurs when an α-particle, a helium nucleus, escapes from a larger atomic nucleus. Since it is a two-body decay, the α-particle has a well defined momentum. The last, γ-decay, is also a two-body process where a high-energy photon is emitted from a nucleus. While only two bodies were seen in β-decay, the β-particle, an electron or positron, was not emitted with a well defined observed momentum. In 1930, Pauli proposed a third particle was involved in the decay. The particle had to be light, since the β-decay momentum endpoint seemed to account for all of the energy loss of the original particle, and it had to be neutral, or else it would be seen in the experiments studying β-decay [3]. Enrico Fermi called the postulated particle a neutrino – Italian for small neutral object.

The neutrino was not discovered until twenty-five years later, when Frederick Reines and company put a detector with a mixture of water and cadmium chloride close to the nuclear reactor at Savannah River, South Carolina, to measure:

$$\bar{\nu} + p \rightarrow e^{+} + free\ neutron$$

The positron emitted in the inverse β-decay is detected when it annihilates with electrons in the detector medium. The neutron slows down until it is captured by a cadmium nucleus about 15 μs later. There are several γ-ray associated with the capture. Scintillation light from both the γ-rays from positron-electron annihilation and those from the capture are detected by photomultiplier tubes (PMTs). Since the signal has a *delayed coincidence* structure, the background can be kept very low - a requirement of all neutrino experiments since neutrinos are so difficult to detect. Similar experimental signatures are used in current experiments to measure neutrinos of energies on the order of several MeV.

In the Standard Model of Particle Physics, which incorporated the strong, weak and electromagnetic forces, all elementary particles into three categories: quarks, leptons and force mediators. The quarks and leptons are all spin one half fermions while the mediators are all spin one bosons. The quarks interact via the the strong, weak and electromagnetic forces and the charged leptons interact via the weak and electromagnetic forces. Neutrinos are neutral leptons and interact exclusively via the weak force. A schematic of the model is shown below:

QUARKS

$$\begin{pmatrix} u \\ d \end{pmatrix} \begin{pmatrix} c \\ s \end{pmatrix} \begin{pmatrix} t \\ b \end{pmatrix}$$

LEPTONS

$$\begin{pmatrix} \nu_{\mathrm{e}} \\ e \end{pmatrix} \begin{pmatrix} \nu_{\mu} \\ \mu \end{pmatrix} \begin{pmatrix} \nu_{\tau} \\ \tau \end{pmatrix}$$

From the β-decay experiments which puzzled Pauli into postulating its existence in the first place, it is clear neutrinos are very light. In addition, helicity measurements indicated neutrinos are always left handed, while anti-neutrinos are always right-handed [4], consistent with a massless neutrino. Direct searches for neutrinos mass use particle decays where a neutrino is present and look for inconsistencies with the zero neutrino mass hypothesis at the kinematic limit of the decay. No evidence has been found for neutrino mass using these methods. The only evidence for neutrino mass so far comes from an indirect approach - experiments examining neutrino oscillation hypotheses. Direct searches and neutrino oscillations are described in the next sections.

1.1 Direct Searches for Neutrino Mass

In this discussion of direct searches, there is an underlying assumption the neutrino mass eigenstates and weak eigenstates are the same. As Shrock has pointed out [5], this is not correct if there is neutrino mixing as described in the next section. The limits derived here would be for a superposition of mass eigenstates.

The best limits on electron neutrino mass come from measuring the endpoint spectrum of the tritium β-decay:

$$^3H \rightarrow\ ^3He^+ + e^- + \bar{\nu}$$

A thin film tritium source is placed in a large spectrometer where the β-decay electrons are guided toward a detector. For example, the Mainz Neutrino Mass Experiment uses a device called MAC-E-filter, magnetic adiabatic collimation followed by an electrostatic filter, shown in Figure 1.1. The non-uniform magnetic field is designed to convert the transverse momentum of the electrons into longitudinal momentum as the electrons pass through the cavity. The electric field acts as a high-energy pass filter. Electrons without enough energy are reflected. Those with enough energy are re-accelerated toward the detector. By tuning the electric field, the tritium β-decay endpoint spectrum is measured. The Mainz and Troitsk experiments have been recently operated and yield the following results on the electron neutrino mass:

$$\begin{array}{ll} m_\nu c^2 \leq 2.2eV & [6] \\ m_\nu c^2 \leq 2.5eV & [7] \end{array}$$

With the current detectors and more data, it might be possible to reach $m_\nu c^2 \sim 2eV$; however, with a much larger spectrometer the groups hope to probe the sub-eV range of neutrino mass.

Charged pion decay yields the best limit on the muon neutrino mass because it is a two-body decay:

$$\pi^+ \rightarrow\ \mu^+ + \nu_\mu.$$

The momentum of the muon is measured and the total energy is calculated and compared with the rest mass of the charged pion. An experiment carried out at PSI in Switzerland measured the muon momentum to be:

$$p_\mu = (29.79200 \pm 0.00011) MeV/c \text{ [9]}.$$

The mass limit derived from the measurement is:

$$m_\nu c^2 \leq 170keV \quad [10].$$

At collider experiments at CLEO and LEP, τ's are produced copiously. By looking for τ decays of high multiplicity, the experiments can approach the kinematic limit. Events where a τ decays into three or five charged particles and zero or more neutrals are called three-pronged or five-pronged events, respectively. By reconstructing the mass of the τ from these decays, limits are set on the tau neutrino mass. The higher the multiplicity of particles, the more likely it is the decay will be close to the kinematic limit; however, the cross-sections are lower. CLEO used three-prong decays of the τ:

$$\tau^- \rightarrow \pi^-\pi^+\pi^-(\pi^0)\nu_\tau.$$

At LEP, ALEPH uses both three-pronged and five-pronged decays:

$$\tau^- \rightarrow 3\pi^- + 2\pi^+(\pi^0)\nu_\tau.$$

The resulting mass limits are:

$m_\nu c^2 \leq 28 MeV$ for CLEO (3-prong) [11]
$m_\nu c^2 \leq 18.2 MeV$ for ALEPH (LEP) (3,5-prong) [12]
$m_\nu c^2 \leq 15.5 MeV$ combined [13]

1.2 Neutrino Oscillation Phenomenology

While there is no evidence for massive neutrinos from experiments searching directly, there has been more success using an indirect method. In 1969, Gribov and Pontecorvo suggested if neutrinos have mass, then like quarks, their mass eigenstates might not be the same as their weak eigenstates and they could mix, or oscillate [14]. If we represent the three known neutrino flavors with α, then the relationship between the weak (flavor) eigenstates and the mass eigenstates can be expressed by a unitary matrix, U:

$$|\nu_\alpha\rangle = \sum_{i=1}^{3} U_{\alpha i}\,|\nu_i\rangle\,, for\ \alpha = e, \mu, \tau$$

where the $|\nu_i\rangle$ are the mass eigenstates.

Since neutrinos are created by weak interactions, when a neutrino is born, it is in a flavor eigenstate. The energy of a free neutrino is $\sqrt{p^2+m^2}$, so if we propagate a free neutrino in time by applying the quantum mechanical time evolution operator we get:

$$|\nu_\alpha(t)\rangle = \sum_{i=1}^{3} U_{\alpha i} \exp{(-i\hat{H}t)}\, |\nu_i\rangle$$

where we have used natural units, $\hbar, c = 1$. We start with a flavor eigenstate, but the propagation through time is through states of definite energy, that is definite mass.

At some later time, we make a measurement to determine if the state is still the same flavor by examining the *survival probability* of the flavor state:

$$P_{\nu_\alpha \rightarrow\ \nu_\alpha} = |\, \langle \nu_\alpha | \nu_\alpha(t) \rangle\, |^2$$

To get a flavor for oscillation, let us assume one of the mass eigenstates is a pure flavor eigenstate. For example, if $|\nu_\tau\rangle = |\nu_3\rangle$, the simplified structure of U is then:

$$\begin{pmatrix} \cos\theta & \sin\theta & 0 \\ -\sin\theta & \cos\theta & 0 \\ 0 & 0 & 1 \end{pmatrix}$$

and the only mixing possible is between two flavors:

$$\begin{pmatrix} \nu_e \\ \nu_\mu \end{pmatrix} = \begin{pmatrix} \cos\theta & \sin\theta \\ -\sin\theta & \cos\theta \end{pmatrix} \begin{pmatrix} \nu_1 \\ \nu_2 \end{pmatrix}$$

Let us make a beam of neutrinos in a pure $|\nu_e\rangle$ state, let them propagate in time, and calculate the survival probability. We know neutrinos are very light, so if we make the assumption $p \gg\ m_1, m_2$,

$$\sqrt{p^2 + m^2}\ =\ p\sqrt{1 + \frac{m^2}{p^2}}\ \approx\ (p + \frac{m^2}{2p})$$

We then have:

$$\langle \nu_e | \nu_e(t) \rangle\ =\ e^{-ip}(\cos^2\theta\ e^{-im_1^2 t/2p} + \sin^2\theta\ e^{-im_2^2 t/2p}).$$

Since the neutrinos are ultra-relativistic, t is equivalent to L, the distance from the production to the detection point. The survival probability then becomes:

$$P_{\nu_e \rightarrow\ \nu_e}\ =\ |\, \langle \nu_e | \nu_e(t) \rangle\, |^2\ =\ 1 - \sin^2 2\theta \sin^2{(1.27 \Delta m^2 \frac{L}{E})}$$

where $\Delta m^2\ =\ m_2^2 - m_1^2$, and following the ultra-relativistic assumption we have equated the neutrino momentum p with its energy E. The 1.27 comes from a factor of $1/4\hbar c$ and in the conversion of L and E to km and GeV, while Δm^2 is in units of eV^2.

The parameters $\sin^2 2\theta$ and Δm^2 are given to us by nature. The survival probability above reveals we must design experiments where L and/or E are varied if we wish to search for neutrino oscillation. Also, if $\Delta m^2 \frac{L}{E} \ll \pi/2$, flavor change by neutrino oscillation cannot be observed. If $\Delta m^2 \frac{L}{E} \sim \pi/2$ and the experimental precision is sufficient, the oscillation might be observable. If $\Delta m^2 \frac{L}{E} \gg \pi/2$ it is likely the oscillations in the survival probability will be washed out by finite resolution of a detector and the energy spread of the beam, so:

$$\sin^2 (1.27 \Delta m^2 \frac{L}{E}) \ \rightarrow \ 1/2.$$

For an arbitrary number of flavor and mass eigenstates, the transition probability ($P_{\nu_\alpha \rightarrow \ \nu_\beta}$) is:

$$P_{\nu_\alpha \rightarrow \ \nu_\beta} \ = \ \delta_{\alpha\beta} - \sum_{i<j} U_{\beta i} U^*_{\alpha i} U^*_{\beta j} U_{\alpha j} \sin^2 (1.27 \Delta m^2_{ij} \frac{L}{E})$$

The discussion above has been for free neutrinos traveling through a vacuum; however, many experiments measure neutrinos after they have passed through a considerable amount of matter. The matter creates a weak potential which alters the Hamiltonian of the otherwise free neutrino. Since ordinary matter contains a lot of electrons, but no muons or τ's, $\nu_{\rm e}$'s and $\bar{\nu}_{\rm e}$'s feel a different potential than ν_μ's, $\bar{\nu}_\mu$'s, ν_τ's, and $\bar{\nu}_\tau$'s. Figure 1.2 shows the neutral current (NC) interaction which causes this forward scattering potential. Figure 1.3 shows the charged current (CC) interaction which contributes to the potential for $\nu_{\rm e}$.

Since the potential is the same for ν_μ and ν_τ, if we consider oscillations between these two flavors, the matter effect cancels out and we have the same equations governing their behavior as for the vacuum case. If, however, we consider flavor oscillations which include $\nu_{\rm e}$, matter effects can have an important role. In addition, if we consider oscillations from any active flavor of neutrino to a “sterile” neutrino (ie. one which is an isosinglet of the weak interaction and thus does not interact via the CC or NC), we must also consider matter effects. This issue will be discussed in more detail later in this chapter.

1.3 Experimental Evidence for Oscillations

There are two general types of neutrino oscillation experiments.

- *Appearance* experiments are those where one searches for the appearance of a flavor not produced in the original beam. For example, if we start with a pure ν_{e} beam and are testing a $\nu_e \leftrightarrow \nu_\mu$ hypothesis, we would search for events induced by ν_μ in excess of experimental background.

- *Disappearance* experiments are those where one starts with one flavor and measures a deficit of neutrinos with the same flavor as the beam. For example, if we search for $\nu_\mu \leftrightarrow \nu_\tau$ oscillation with a ν_μ beam using CC events, we could be below the energy threshold to make a τ. In this case, the evidence for $\nu_\mu \leftrightarrow \nu_\tau$ oscillation would be "missing" ν_μ neutrinos.

1.3.1 Solar Neutrinos

Solar neutrinos are produced in the core of the sun in the fusion reactions which power the star:

$$p + p \rightarrow \ {}^2H + e^+ + \nu_e \ (pp\ neutrinos)$$

$$OR$$

$$p + e- + p \rightarrow \ {}^2H + \nu_e \ (pep\ neutrinos)$$

$${}^2H + p \rightarrow \ {}^3He + \gamma$$

$${}^3He +^3 He \rightarrow \ \alpha \ + 2p$$

$$OR$$

$${}^3He +^4 He \rightarrow \ {}^7Be + \gamma$$

$${}^7Be + e^- \rightarrow \ {}^7Li + \nu_e \ ({}^7Be\ neutrinos)$$

$${}^7Li + p \rightarrow \ 2\alpha$$

$$OR$$

$${}^7Be + p \rightarrow \ {}^8B + \gamma$$

$${}^8B \rightarrow \ {}^8Be^* + e^+ + \nu_e \ ({}^8B\ neutrinos)$$

$${}^8Be^* \rightarrow \ 2\alpha$$

$$OR$$

$$^3He + p \rightarrow\ ^4He + e^+ + \nu_e\ (hep\ neutrinos)$$

The resultant spectrum of electron neutrinos is shown in Figure 1.4. All solar neutrinos are ν_{e}'s. The ^7Be and *pep* neutrinos give us three lines in energy, ^7Be has two, and the *pp*, ^8B, and *hep* neutrinos give a wide spectrum up to almost 20 MeV. The wide energy spectrum and long baseline from the core of the sun to the earth allows us to explore a large area of the Δm^2 - $\sin^2 2\theta$ parameter space. By far the most numerous are the *pp* neutrinos, but these are hard to detect because their energies are very low.

The first experimental hint that neutrinos might undergo flavor transformation came with measurements by Ray Davis and collaborators in 1968 [15]. Davis had developed a technique to separate argon from large volumes of perchloroethylene (cleaning fluid), C_2Cl_4. To search for the inverse β-decay $^{37}Cl + \nu_e \rightarrow e^- +^{37}Ar$ from solar neutrinos, Davis put a tank of 100,000 gallons of perchloroethylene in the Homestake mine in South Dakota. Figure 1.4 shows the energy threshold of several experiments including Homestake (Chlorine in the figure). Though there are several available channels, ^8B and ^7Be are the primary sources of neutrinos detected in Homestake. The first results put an upper limit of 3 SNU (Solar Neutrino Unit: $10^{-36} captures/second/atom$), in conflict with the theoretically predicted value of 7.5 ± 3 [17].

In the 1980's and 1990's, several other experiments observed solar neutrinos and confirmed the deficit. Radio-chemical gallium experiments, Gallex [18] and SAGE [19], are the only ones to have observed the *pp* neutrinos. They have confirmed the sun is shining. Kamiokande [20], a 3 $kiloton (kt)$ water Cherenkov detector located in the Kamioka mine in Japan, was the first experiment to see solar neutrinos in real time. Kamiokande observed Cherenkov light from elastic scattering, $\nu_e + e \rightarrow\ \nu_e + e$. Since at these energies, the electron direction is correlated with the neutrino direction, Kamiokande was able to point back to the sun and confirm the events were indeed due to solar neutrinos.

Super–Kamiokande [21], a larger version of Kamiokande with a 5 MeV energy threshold, also sees a large deficit of ν_{e}'s coming from the sun. Details of the detector are described in Chapter 3. The SNO experiment [22], which began running in 2000 employs D_2O. In addition to elastic scattering measurements like those of Super–Kamiokande, SNO also measures inverse β-decay which is only sensitive to ν_{e}.

$$\nu_e + d\ \rightarrow\ \ e^- + p + p$$

By comparing these results with Super–Kamiokande's elastic scattering results (sensitive to all flavors), SNO has shown solar neutrinos oscillate into another active flavor(s) [23].

Figure 1.5 shows the allowed region for two-flavor mixing combining results from all solar neutrino experiments. The allowed region is $3 < \Delta m^2 < 25 \times 10^{-5}\ eV^2$ and $0.21 < \tan^2\theta < 0.67$ [24].

1.3.2 Atmospheric Neutrinos

When cosmic rays collide with nuclei in the upper atmosphere, the interactions create hadronic showers resulting in many charged pions. Since charged pions decay:

$$\pi^+ \rightarrow \ \mu^+ + \nu_\mu$$

followed by:

$$\mu^+ \rightarrow \ e^+ + \bar{\nu_\mu} + \nu e,$$

one expects a large number of atmospheric neutrinos where the ratio, $\frac{\nu_\mu + \bar{\nu_\mu}}{\nu_e + \bar{\nu_e}} \approx 2$. Atmospheric neutrinos are described in more detail in Chapter 2.

Originally, the IMB [25] and Kamiokande [26] experiments studied atmospheric neutrinos as backgrounds to an expected proton decay signal. The signal did not show its face, but the "atmospheric neutrino anomaly" became the strongest indication for neutrino flavor oscillation. IMB was an 8 *kt* water Cherenkov detector located in the Morton salt mine near Cleveland, Ohio. Both IMB and Kamiokande measured a double ratio:

$$R \equiv \frac{\mu_{data}/\mu_{MC}}{e_{data}/e_{MC}}$$

where μ represents events which appear to be the result of a CC ν_μ interactions, and e represents events which appear to come from CC ν_{e} interactions. MC is the Monte Carlo simulation program. The double ratio compares the flavor ratio predicted by simulations to that measured in the detector. Both IMB and Kamiokande measured the R value significantly lower than 1. Later experiments, NUSEX [27], Frejus [28] and Soudan [29], using iron calorimeters did not initially measure significant deviation from 1, though Soudan 2 later, with a much larger event sample also measured a low R [29].

In addition to the total double ratio, Kamiokande measured a zenith angle dependence of R in its high-energy sample. The individual samples for Super–Kamiokande, measured to much higher precision, are shown in Figure 1.6. The red line is the MC prediction for no oscillations. The green line is the best fit using these data to the $\nu_\mu \leftrightarrow \nu_\tau$ oscillation hypothesis. Clearly something is "happening" to the ν_μ's on their way to the detector.

As shown in Figure 1.7, the zenith angle of a neutrino corresponds to L, its distance from the production point of neutrinos. Thus, by measuring zenith angle distributions, atmospheric neutrinos experiments "vary" L. Consequently, Figure 1.6 represents the most convincing evidence for flavor oscillation. The allowed region obtained by analyzing these data for neutrino oscillation parameters is shown in Figure 1.8. Atmospheric muon neutrinos seem to undergo maximal mixing with $1.9\times 10^{-3}eV^2 < \Delta m^2 < 3.9\times 10^{-3}eV^2$.

To confirm the observations of Super–Kamiokande and other atmospheric neutrino experiments, long-baseline neutrino experiments have been constructed. The first long-baseline experiment to test the Super–Kamiokande allowed region is the K2K (KEK to Kamioka) experiment. A beam of muon neutrinos with an energy spectrum similar to atmospheric neutrinos is created at KEK and steered through the earth toward Super–Kamiokande, 250 km away. Preliminary results confirm the Super–Kamiokande result and data will be collected until 2005. More details of this experiment are discussed in the rest of this thesis.

1.3.3 LSND

The Liquid Scintillation Neutrino Detector (LSND) was operated at Los Alamos National Lab from 1993 to 1998 to search for $\bar{\nu}_\mu \rightarrow \bar{\nu}_\mathrm{e}$ oscillation. The detector was an approximately cylindrical tank filled with 167 metric tons of mineral oil doped with 0.031 g/l of $b - PBD$. The low concentration of scintillator allowed the measurement of both Cherenkov and scintillation light. The proton beam created large numbers of charged pions which were then passed through a beam dump, leaving mostly π^+'s and μ^+'s which decay to make a neutrino beam consisting of ν_μ, ν_e, and $\bar{\nu}_\mu$ with almost no $\bar{\nu}_\mathrm{e}$. If, $\bar{\nu}_\mu \leftrightarrow \bar{\nu}_\mathrm{e}$ oscillation is occurring, The $\bar{\nu}_\mathrm{e}$'s can be detected by inverse β-decay:

$$\bar{\nu}_e + p \;\rightarrow\; e^+ + n$$

where the neutron gets captured with a capture time of 186 μs. The capture on a proton creating a deuteron causes the emission of a 2.2 MeV gamma ray, and this delayed coincidence keeps background low.

LSND observed an excess of $87.9 \pm 22.4 \pm 6.0$ $\bar{\nu}_\mathrm{e}$ -like events. Figure 1.9 shows the allowed region by interpreting this excess and neutrino oscillation. The Δm^2 allowed is in the range $0.4 \sim 10$ eV^2 [30]. Also shown in the figure are the excluded regions for other experiments. Notably, the Karmen experiment which has a sensitivity similar to that of LSND has excluded a large fraction of the LSND allowed region.

1.4 Sterile Neutrinos

In summary, assuming these experiments are correct, we have three sets of experiments favoring three different Δm^2's, which imply at least four neutrino mass states. Let us define active particles to be ones interacting via Standard Model interactions and light particles to be ones with mass less than half of the Z boson mass. If there were four generations of light, active neutrinos, the fourth generation would contribute to the width of the Z mass. By measuring the width, LEP experiments have shown the number of active neutrino flavors to be three [31]. Thus, if there is a fourth generation of light neutrino, it must be a sterile neutrino (ν_s) - one which does not interact via Standard Model interactions, especially, the weak interaction. It is important to note a "sterile" neutrino could interact with matter via non-Standard Model forces.

Clearly, the neutrino oscillation experimental signature from active to sterile flavors must be disappearance, but how can active to active and active to sterile hypotheses be distinguished when all one observes is active flavors disappearing? The reason active flavors can "disappear" is the oscillation takes place at neutrino energies where the new active flavor is below threshold for CC interactions. The same is not true for NC interactions because a charged lepton is not produced. We can distinguish the active-active vs. active-sterile cases in a disappearance experiment by looking at the rate of NC interactions. If the oscillation is active-active, the NC rate should be the same as if there were no oscillation. In the active-sterile case, there should be an attenuation of the NC signal.

Another way to distinguish between the two cases is looking for matter effects. In section 1.2, it was noted the forward scattering potential for electron neutrinos is different from the potential for muon and tau neutrinos. Since by definition, sterile neutrinos do not interact at all via the weak force, the potential is different for active flavors than for sterile ones. For $\nu_\mu \leftrightarrow \nu_s$, the matter effect modifies the oscillation probability:

$$P(\nu_\mu \to \nu_s) = \frac{\sin^2 2\theta}{R} \times \sin^2\left(\pi \frac{L\Delta m^2}{\frac{4\pi E_\nu}{\sqrt{R}}}\right),$$

where $R = (\mp \frac{\sqrt{2} G_F N_n E_\nu}{\Delta m^2} - \cos 2\theta)^2 + \sin^2 2\theta$, N_n is the neutron density of the medium, G_F is the Fermi constant

Super–Kamiokande has exploited these differences to distinguish between the $\nu_\mu \leftrightarrow \nu_\tau$ and $\nu_\mu \leftrightarrow \nu_s$ hypotheses using atmospheric neutrinos. While the cross-sections of NC interactions at atmospheric neutrino energies which produce identifiable signals are not well known, high-energy NC events carry directional information of the parent neutrino. The distance to the point of production for neutrinos produced above the detector is only $\sim 15km$, while the distance for neutrinos produced below the detector is $\sim 13,000km$. Therefore, for high neutrino energies, the down-going neutrinos have not had time to oscillate. If the $\nu_\mu \leftrightarrow \nu_\tau$ hypothesis is correct the expectation of the up-down ratio of high-energy NC events is near-symmetry, while if the $\nu_\mu \leftrightarrow \nu_s$ hypothesis is correct the ratio should be less than one. For the neutron densities of the earth, $\nu_\mu \leftrightarrow \nu_s$ oscillation becomes suppressed for neutrino energies of $\sim 15GeV$ due to the matter effect. Below these energies, the probability is similar in both the matter and vacuum case. By selecting event samples produced by high-energy muon neutrinos, one can search for matter effects. In this case, one expects near-symmetry for the $\nu_\mu \leftrightarrow \nu_s$ case because oscillation of high-energy neutrinos is suppressed. Super–Kamiokande has used up-down ratios of a high-energy NC sample and two CC ν_μ samples produced by high energy neutrinos to exclude the $\nu_\mu \leftrightarrow \nu_s$ hypothesis at the 99% confidence level [32]. Figure 1.10 shows up-down ratios for the three samples with predictions for $\nu_\mu \leftrightarrow \nu_\tau$ and $\nu_\mu \leftrightarrow \nu_s$.

Another way to discriminate between the two hypotheses is to measure the ratio of a NC rate with respect to a CC rate and compare it with predictions for each possibility. Single-π^0 production by atmospheric neutrinos is a clean NC signature in Super–Kamiokande. Until recently, the systematic error on NC to CC ratios due to single pion cross-section uncertainties was larger than 20% [33], while the predicted difference between $\nu_\mu \leftrightarrow \nu_\tau$ and $\nu_\mu \leftrightarrow \nu_s$ oscillations at Super–Kamiokande's best-fit point is on the order of 20%. Since the K2K beam neutrino energy spectrum is similar to the atmospheric neutrino energy spectrum, we can measure a NC to CC ratio at the K2K near detector and use it to lower the systematic error for a $\nu_\mu \leftrightarrow \nu_\tau$ vs. $\nu_\mu \leftrightarrow \nu_s$ analysis using the Super–Kamiokande atmospheric neutrino sample.

K2K uses a pure ν_μ beam, so we define a ratio (π^0/μ) using the single-π^0 sample and the fully-contained (FC) single-ring muon-like events. We then define a double ratio $R_{\pi^0} \equiv \frac{(\pi^0/\mu)_{data}}{(\pi^0/\mu)_{MC}}$. This thesis describes the measurement of R_{π^0} made in the K2K 1-kiloton water Cherenkov detector and the $\nu_\mu \leftrightarrow \nu_\tau$ vs. $\nu_\mu \leftrightarrow \nu_s$ analysis of atmospheric neutrinos using the single-π^0 measurement at Super–Kamiokande.

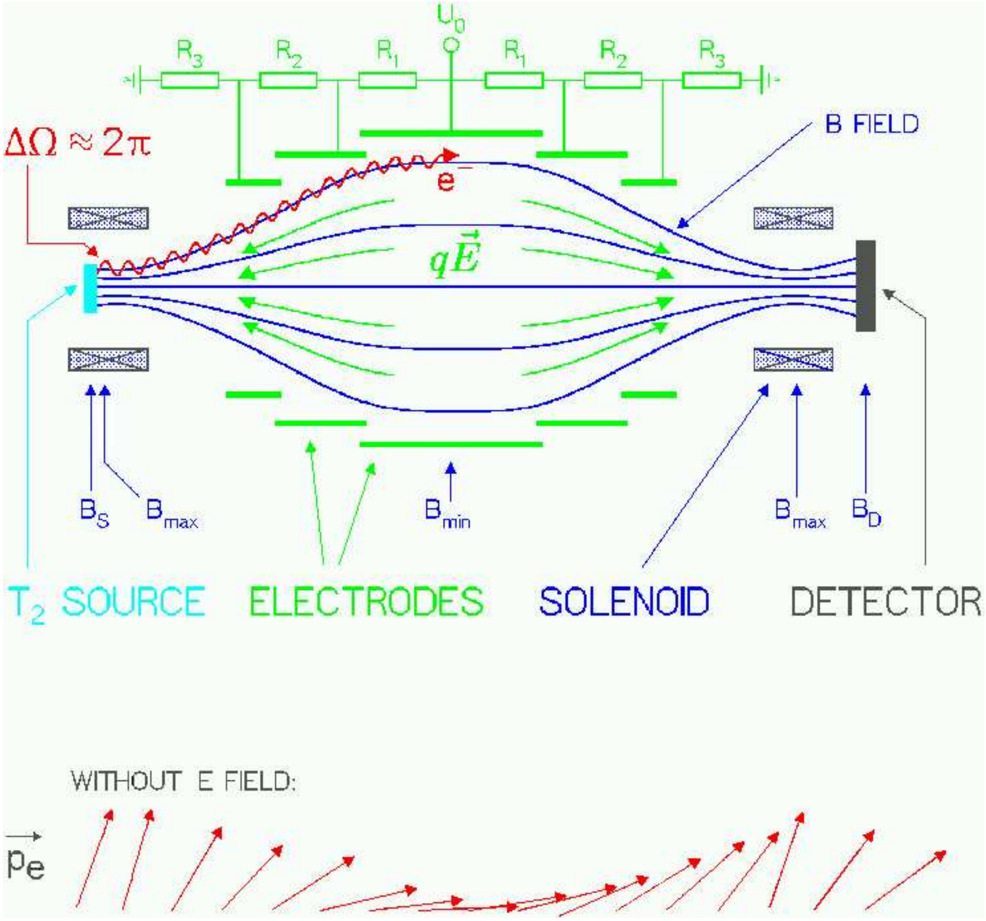

Figure 1.1: The MAC-E-filter detector [8]. As the β electrons pass through the detector, the magnetic field weakens adiabatically, converting the transverse momentum of the electrons to longitudinal momentum.

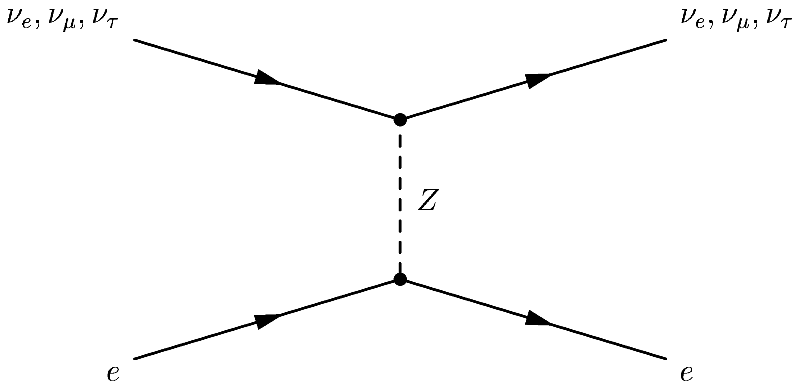

Figure 1.2: The Feynman diagram of the NC interaction which creates the forward scattering potential for ν_{e}, ν_μ, and ν_τ(as well as the charge conjugates of each).

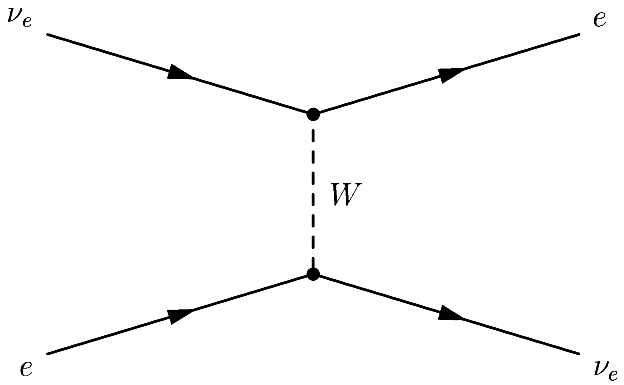

Figure 1.3: Since matter contains electrons, there is an additional contribution to the potential for ν_{e} from this CC interaction. There is a similar CC contribution for $\bar{\nu}_{\mathrm{e}}$.

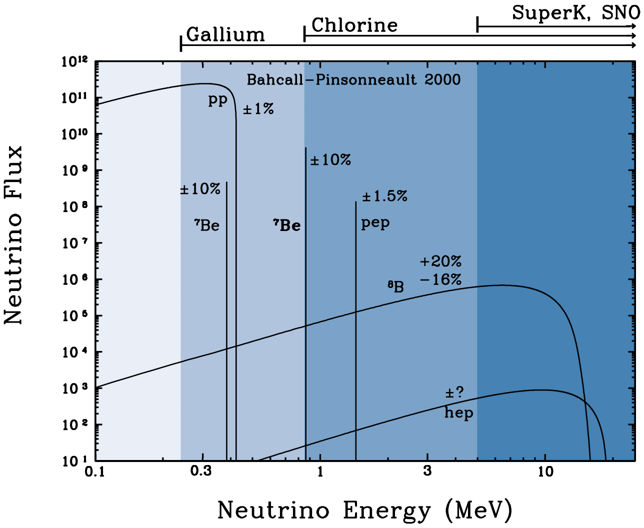

Figure 1.4: Solar neutrino energy spectrum [16].

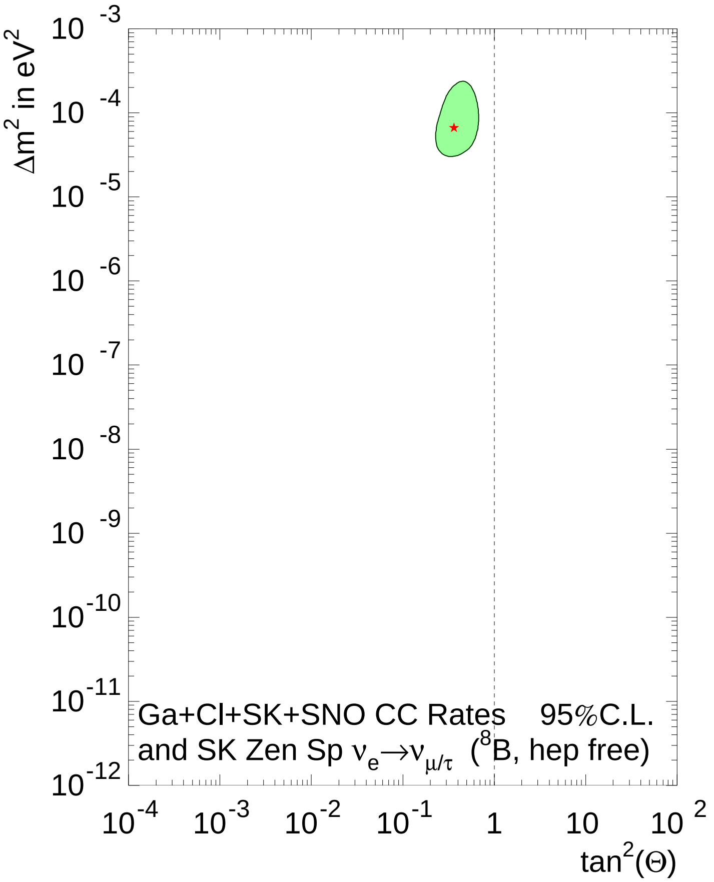

Figure 1.5: The Super–Kamiokande solar neutrino allowed region.

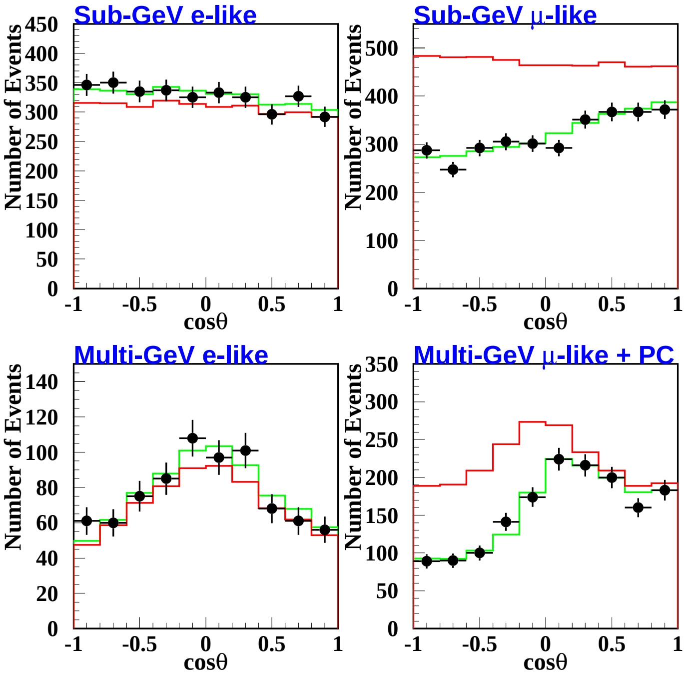

Figure 1.6: Atmospheric neutrino zenith angle distribution. The green lines are the fit to these data of the $\nu_\mu \leftrightarrow \nu_\tau$ oscillation hypothesis. The red line is the null hypothesis.

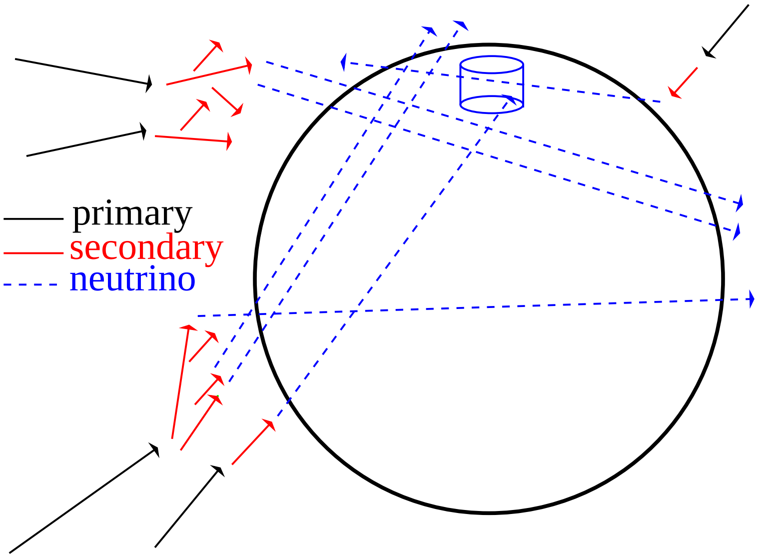

Figure 1.7: Different zenith angles imply different L, which allow atmospheric neutrino experiments to probe neutrino flavor oscillation. In the figure, the circle is the earth and the cylinder is the (not-quite-to-scale) Super–Kamiokande detector.

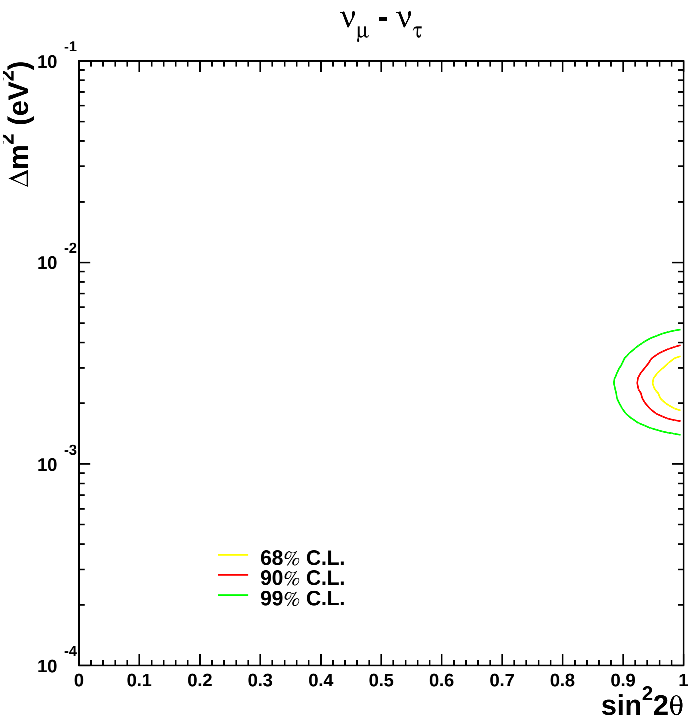

Figure 1.8: The Super–Kamiokande atmospheric neutrino combined allowed region.

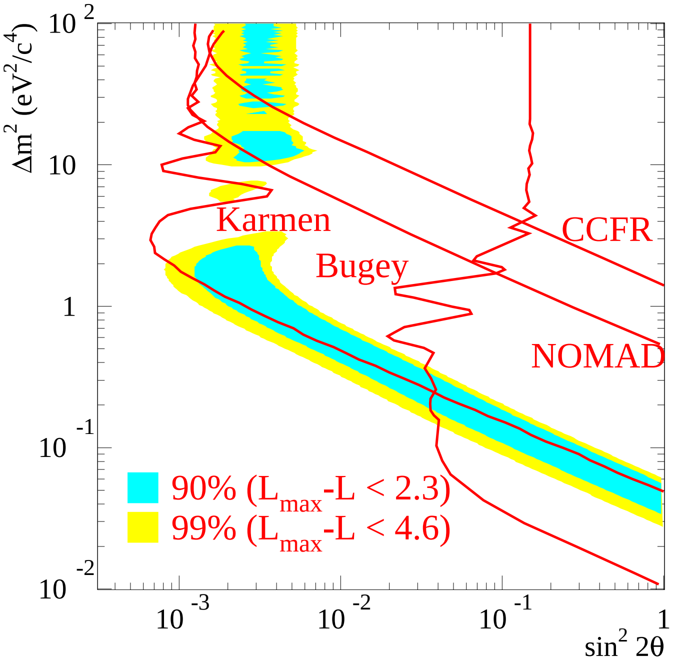

Figure 1.9: The LSND allowed region with excluded regions from other experiments: KARMEN, NOMAD and BUGEY. The figure is taken from Ref. [30]

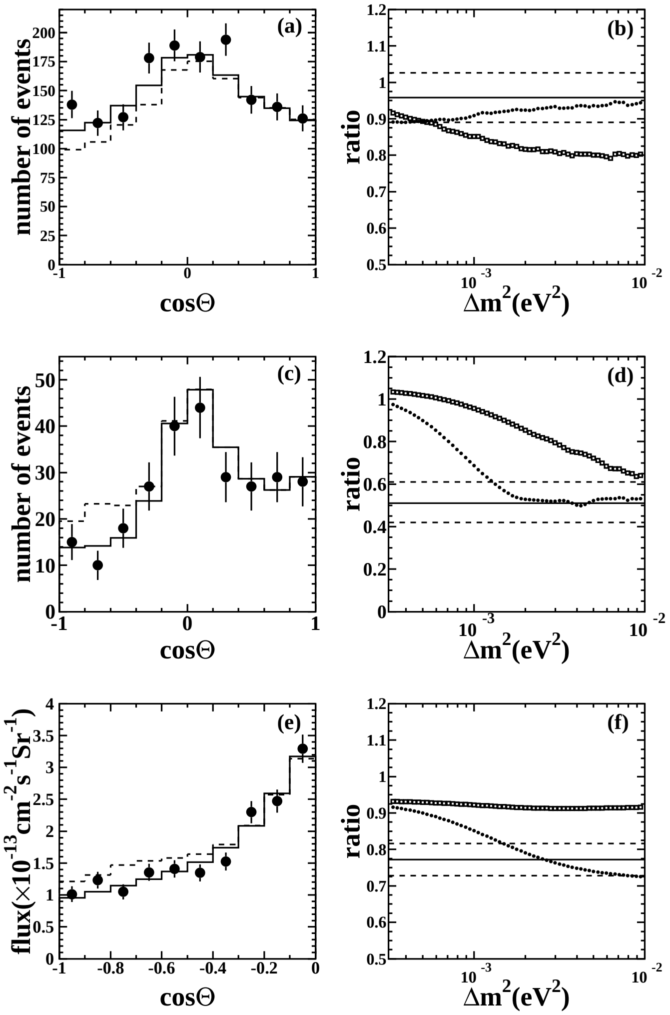

Figure 1.10: The figures on the left are zenith angle distributions, while the figures on the right are up-down ratio plots. In the zenith angle distributions, the solid lines are the $\nu_\mu \leftrightarrow \nu_\tau$ oscillation hypothesis, while the dashed lines are the $\nu_\mu \leftrightarrow \nu_s$ hypothesis. In the up-down ratio plots, the solid horizontal line is the measured value and the dashed horizontal lines represent the 1 σ error bars. The $\nu_\mu \leftrightarrow \nu_\tau$ and $\nu_\mu \leftrightarrow \nu_s$ predictions for the ratios are shown as a function of Δm^2. Black dots correspond to the $\nu_\mu \leftrightarrow \nu_\tau$ prediction while open squares show the $\nu_\mu \leftrightarrow \nu_s$ prediction. The top figure is the NC enhanced sample. The middle figure is PC events. The bottom figure is upward-going muons. For the upward-going muons, the ratio is horizontal vs. upward-going.

Chapter 2

Neutrino Sources

While neutrinos can be created through a variety of processes, the neutrino beams used in this thesis are primarily from charged pion decay. The charged pions are produced by smashing nucleons into target nuclei at high energies. While the resulting cascade includes other mesons, pions are by far the most numerous.

2.1 Atmospheric Neutrinos

When cosmic rays (primary) pass close to the earth, they interact with the nitrogen, oxygen, carbon, helium and hydrogen nuclei of the upper atmosphere and create hadronic showers. Large numbers of charged pions are produced. Since they almost always decay into a muon and neutrino, large numbers of muons and muon neutrinos are generated. When the muons decay they produce another (anti)muon neutrino and an electron neutrino. Thus, naively, one would expect a 2:1 ratio of muon-type neutrinos to electron-type neutrinos in atmospheric neutrinos.

2.1.1 Primary Cosmic Ray Flux

While the origin of primary cosmic rays is not very well known, many measurements have been made of their energy and composition. They were discovered in 1912 when Victor Hess found evidence for penetrating radiation in a balloon at 5000 meters.

Cosmic rays consist primarily of protons with the remainder is mostly helium ions. For neutrino production it is the total number of nucleons which is relevant. The composition of $\sim 10\ GeV$ primary cosmic rays is 4/5's hydrogen and 1/6 helium. The rest is from carbon, nitrogen, oxygen and heavier nuclei [34].

In order to measure the primary cosmic ray flux, detectors are either flown on high altitude balloons or on Space Shuttle flights. A summary of current measurements is shown in Figure 2.1. Below 100 *GeV*, measurements are made with magnetic spectrometers [35, 36, 37, 38, 39, 40, 41, 42]. Above 100 *GeV*, measurements have been made using calorimeters [43, 44, 45, 46, 47].

The sun emits a magnetized plasma called the "solar wind". Cosmic rays must pass through the solar wind to reach the earth. High energy particles lose energy, while very low energy particles do not reach the earth. The strength of the solar wind changes over the course of the solar cycle. At solar maximum, the flux of particles from the sun is at its peak, which prevents large quantities of low energy particles of cosmic origin from reaching the earth. The spectrum and flux of cosmic rays at high energies is stable with respect to solar modulation, but at low energies (below 10 *GeV/nucleon*) the flux and spectral shape of cosmic rays changes dramatically. At 1 *GeV*, for example, the proton flux changes by more than a factor of four between solar minimum and solar maximum [48].

Since the earth has a magnetic field, particles with a low momentum will be deflected. Except for these geomagnetic effects, the flux of cosmic rays is isotropic to 0.1% [49].

2.1.2 How This Makes neutrinos

When cosmic rays enter the atmosphere, they interact with atmospheric nuclei and create hadronic showers. The hadronic end-products of these showers which are responsible for most neutrino production up to at least multi-TeV neutrino energies are pions and kaons:

$$\pi^{\pm} \rightarrow \mu^{\pm} + \nu_{\mu}(\bar{\nu}_{\mu}),$$

followed by:

$$\mu^{\pm} \rightarrow e^{\pm} + \nu_{e}(\bar{\nu}_{\mathrm{e}}) + \bar{\nu}_{\mu}(\nu_{\mu}).$$

Neutral kaons contribute via:

$$K_L^0 \rightarrow \pi^{\mp} + \mu^{\pm} + \nu_{\mu}(\bar{\nu}_{\mu}),$$

$$K_L^0 \rightarrow \pi^{\mp} + e^{\pm} + \nu_{e}(\bar{\nu}_{\mathrm{e}}),$$

$$K_L^0 \rightarrow \pi^{+} + \pi^{-} + \pi^{0},$$

$$K_S^0 \rightarrow \pi^{+} + \pi^{-}.$$

Charged kaons contribute via:

$$K^{\pm} \rightarrow \mu^{\pm} + \nu_{\mu}(\bar{\nu}_{\mu}),$$

$$K^{\pm} \rightarrow \mu^{\pm} + \nu_{\mu}(\bar{\nu}_{\mu}) + \pi^{0},$$

$$K^{\pm} \rightarrow e^{\pm} + \nu_{e}(\bar{\nu}_{e}) + \pi^{0},$$

$$K^{\pm} \rightarrow \pi^{\pm} + \pi^{0},$$

$$K^{\pm} \rightarrow \pi^{\pm} + \pi^{0} + \pi^{0},$$

$$K^{\pm} \rightarrow \pi^{\pm} + \pi^{+} + \pi^{-}.$$

Production of charmed mesons dominates the neutrino flux at very high energies - somewhere above 10 to 100 TeV [34].

Theoretical calculations of the absolute flux vary by $\sim 20\%$, mostly due to differences in the pion production models used. With the BESS and AMS data [41, 42], the primary cosmic ray flux uncertainties are down to 5 % below 100 $GeV/nucleon$ for the proton fluxes and 15 % for the helium fluxes. This is the range of primaries which produces most neutrinos with energies below 10 GeV [34]. The $\frac{\nu_{\mu}+\bar{\nu}_{\mu}}{\nu_{e}+\bar{\nu}_{e}}$ ratio is known to 5 % over a broad range of neutrino energies, $0.1 \sim 10$ GeV, since they are dominated by charged pion decay. The $\nu/\bar{\nu}$ ratio, which depends on the proton/neutron ratio of the primaries is known to 10 % [50]. The resulting neutrino fluxes are shown in Figure 2.2.

2.2 K2K Beam

In the late 1980's and early 1990's, Kamiokande and IMB atmospheric neutrino data indicated there might be $\nu_{\mu} \leftrightarrow \nu_{\tau}$ or $\nu_{\mu} \leftrightarrow \nu_{e}$ flavor oscillation [25, 26]. The KEK to Kamioka long-baseline neutrino oscillation experiment (K2K) was built to study this question using accelerator-produced neutrinos. K2K uses an intense, high-purity wide-band muon neutrino beam (98.2% ν_{μ}, 1.3% ν_{e}, and 0.5% $\overline{\nu}_{\mu}$) with an average energy $\langle E_{\nu} \rangle \approx 1.3$ GeV [52] to investigate neutrino flavor oscillation. The K2K neutrino energy spectrum was designed to be similar to the atmospheric neutrino energy spectrum and is indeed produced using similar physical mechanisms. The primary beam for K2K is the 12 GeV kinetic energy proton beam from the KEK proton-synchrotron (KEK-PS)[53]. Every 2.2 s, approximately 6×10^{12} protons in nine bunches are fast-extracted in a single turn, making a $1.1\mu s$ beam spill. It is smashed into an aluminum target creating large numbers of charged pions which are focused down a decay-pipe using a horn magnet system. (Figure 2.3). The pions decay into a μ^+ and a ν_μ. The muons are filtered out by a beam stop. The resultant neutrino beam passes through a series of near detectors before making the 250*km* journey to the Super–Kamiokande detector. Using Global Positioning System satellites, interactions due to the K2K neutrino beam can be tagged and analyzed. More information about the near neutrino detectors is found in the next chapter.

2.2.1 How Is It made?

The KEK Proton Synchrotron (PS) injects its protons into the neutrino beam line every 2.2 seconds by fast extraction. The nine bunches are about 120 *ns* apart, so one beam spill is about 1.1 μs. The bunch structure is shown in Figure 2.4.

After being guided down the beam line, the protons are focused onto the target, an aluminum rod 66 *cm* long and 3 *cm* in diameter. The target is a current-carrying element of the first of two horns. The first horn is a hollow shell of aluminum with the target rod inside and is 0.7 *m* in diameter and 2.37 *m* in length. A pulsed current is supplied to the shell and returned an inner conductor and the target rod creating a toroidal magnetic field. The field focuses positively charged particles inward and deflects negatively charged particles out of the beam. The second horn is also a hollow shell and inner conductor of aluminum with diameter 1.65*m* and length 2.76*m*. It is designed to collect positively charged pions and focus them toward the decay-pipe. Both horns are pulsed every 2.2 seconds in time with the beam spill reaching a current of 250 kA. The total pulse duration is 3 ms. They are pulsed to avoid thermal melt-down and to minimize energy consumption.

After the second horn is a region where calibration detectors can be placed, followed by the decay-pipe. Beam monitors which are not in place during normal running, are described in the next subsection.

The decay-pipe begins 19*m* downstream from the target. The first section is 10*m* in length and 1.5*m* in diameter, followed by 90*m* section 2*m* in diameter pipe, and finally a 100*m* section 3*m* in diameter. The pipe is filled with helium gas to minimize absorption losses and secondary uncontrollable pion production.

At the end of the pipe is a beam dump consisting of 3.5*m* of iron, 2*m* of concrete and 60*m* of soil.

2.2.2 How Is It Measured/Calculated?

While there are many instruments used to measure the intensity and size of the primary proton beam, there are two systems used to measure the pions and protons after the target and horns. These systems are not in place during normal running because they would change the beam characteristics. There is an additional system at the end of the decay-pipe which measures the muons produced from pion decay. This system of detectors collects data during normal operation.

The pion monitor is a gas filled vessel with a wedge of a spherical mirror mounted inside (Figure 2.5). When the monitor is rolled into place, the mirror is in the beam at an angle of 30° rotated about its long axis with respect to the beam-line. During running, the mirror reflects Cherenkov radiation from pions in the beam toward an array of 20 photo-multiplier tubes (PMTs). The purpose of the detector is to measure the momentum and polar angle of the pions after the horn system. Once these secondary pion production properties are measured, the neutrino energy spectrum can be deduced using simple pion kinematics. Azimuthal symmetry of the pion beam is assumed in this measurement.

Cherenkov radiation is an effect similar to a sonic boom. When a particle's speed is faster than the speed of light in the medium in which it travels, a cone of light is emitted with the following properties:

$$\cos\theta_{Ch} = \frac{1}{n\beta}$$

where $\beta = v/c$, the speed of the particle divided by the speed of light in vacuum, n is the index of refraction of the medium, and $\cos\theta_{Ch}$ is the half-angle of the cone of emitted light.

Light incident on a spherical mirror is reflected onto a point on the focal plane of the mirror based on the angle of incidence on the mirror, independent of the position of incidence on the mirror.

If we make the assumption for the moment the only particles in the beam are charged pions and the magnitude of momentum is the same for all of them, measuring the intensity of light across the focal plane would be a measurement of pion flux as a function of polar angle. If we make a complementary assumption, all pions are collinear, since the Cherenkov angle depends on momentum, measuring the intensity of light across the focal plane would be a measurement of the momentum distribution of pions in the beam. Changing the gas pressure in the vessel changes the index of refraction, which changes the Cherenkov angles for a given pion momentum and the momentum threshold for Cherenkov radiation. By varying the gas pressure, the momenta and polar angles can be de-convolved.

Since protons are more massive than pions, their Cherenkov threshold is higher. The highest gas pressure used is such that the proton Cherenkov threshold is 13 GeV. Since the beam energy is 12 GeV, we are assured protons do not contaminate the measurement of the pions. However, this puts a lower limit on the visible pion momentum and therefore pion monitor studies are only useful to reconstruct the neutrino flux for $E_\nu > 1GeV$.

In order to obtain the information on neutrino energy below 1 GeV, beam Monte Carlo studies and quasi-elastic neutrino interaction studies using near detector data are used. For the purposes of this thesis, precise knowledge of the neutrino spectrum below $E_\nu \approx 1GeV$ is unnecessary since single π^0 events, which are mostly NC induced, are measured in a ratio with single muon events, which are mostly CC induced. Figure 2.7 shows the neutrino spectrum calculated by beam MC with input from pion monitor data at the near detector.

The pion monitor relies on the azimuthal symmetry of the beam. The symmetry is measured by the next detector down the beam-line, the ionocopter.

Two ionization chambers are mounted on a wheel which is rotated over a range of 220° (Figure 2.8). Each chamber has 22, $5cm$ square pads organized in a 2×11 grid. Since the chambers are 180° apart from each other, by rotating through the full range of motion of the wheel, the chambers can be calibrated relative to each other.

Data are not collected during normal running since, like the pion monitor, the ionocopter measurement is destructive. The sample data in Figure 2.9 show good azimuthal symmetry.

Since neither the pion monitor nor the ionocopter can be in the beam during normal running, it is useful to have a way of monitoring neutrino production during normal runs. At the end of the decay-pipe are a collection of detectors which measure the muon flux from pion decay. The measurements provide both flux information and monitoring of the pointing accuracy of the neutrino beam and are used to select good spills - those which will be used for data analysis.

The muons monitors are placed downstream of the $3.5m$ of iron and $2m$ of concrete. All hadronic particles are filtered out by this material and only high energy muons penetrate to the detectors. There is a segmented plate ionization chamber (μ-SPIC) and a solid silicon detector (SSD) array as shown in Figure 2.10. The μ-SPIC covers a $1.75m \times 1.9m$ area and measures the horizontal and vertical projections of the muon profile. The SSD is a silicon pad detector where pads are arrayed in the shape of two concentric crosses covering an area

$2.8m \times 2.8m$. The 17 pads on the horizontal and vertical axes are $1cm \times 2cm$ and spaced $35cm$ apart, while the diagonal axes (u and v) use 9 larger pads $3.4cm \times 3.05cm$ (Figure 2.10). The SSD gives two dimensional beam-profile information.

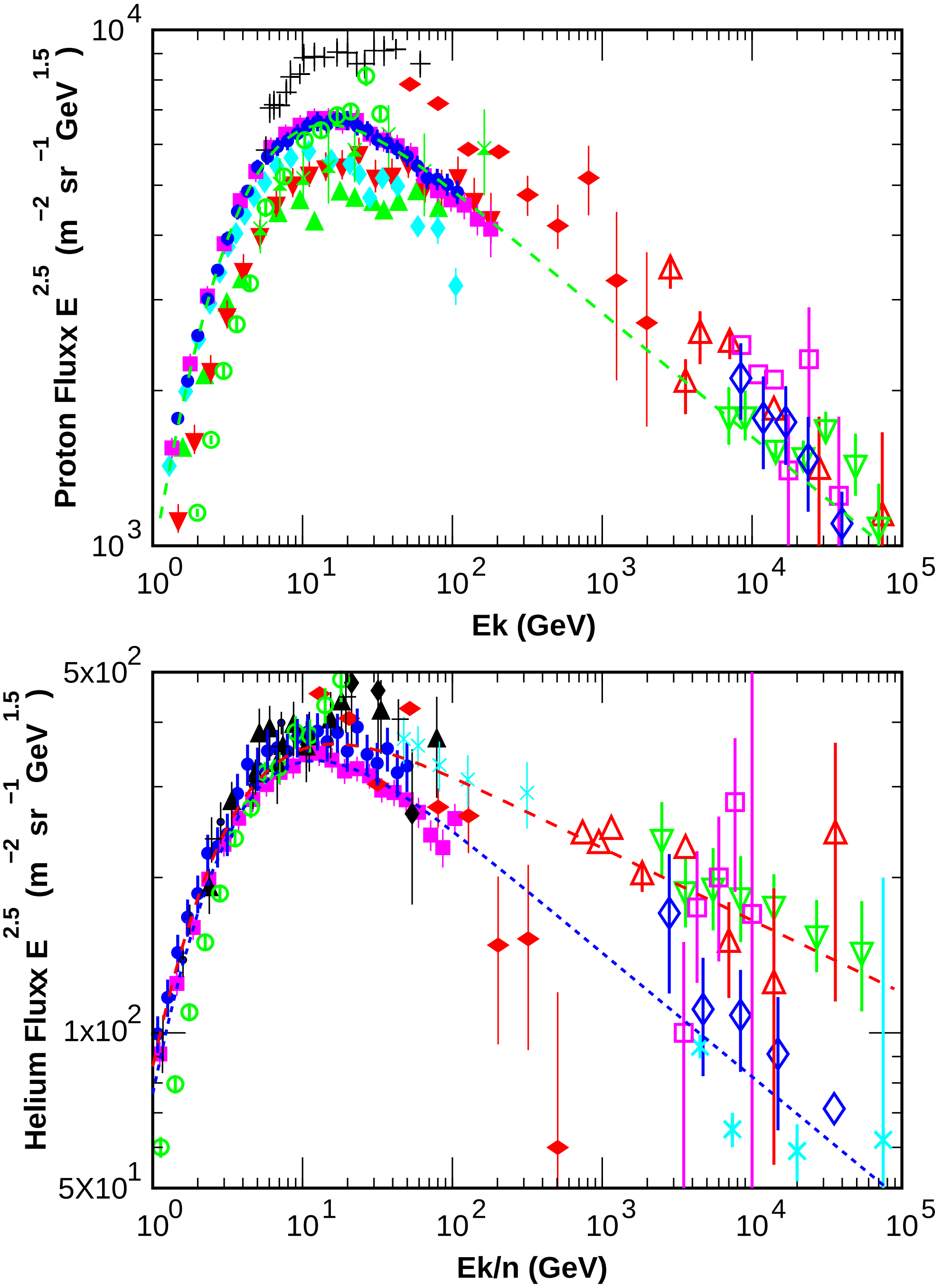

Figure 2.1: A Summary of Cosmic ray data with predictions from [34]. The references for the data are: crosses [35], upward triangles [36], open circles [37], vertical diamonds [39], downward triangles [40], circles [41], squares [42], horizontal diamonds [43], downward open triangles [44], upward open triangles [45], open diamonds [46], and open squares [47].

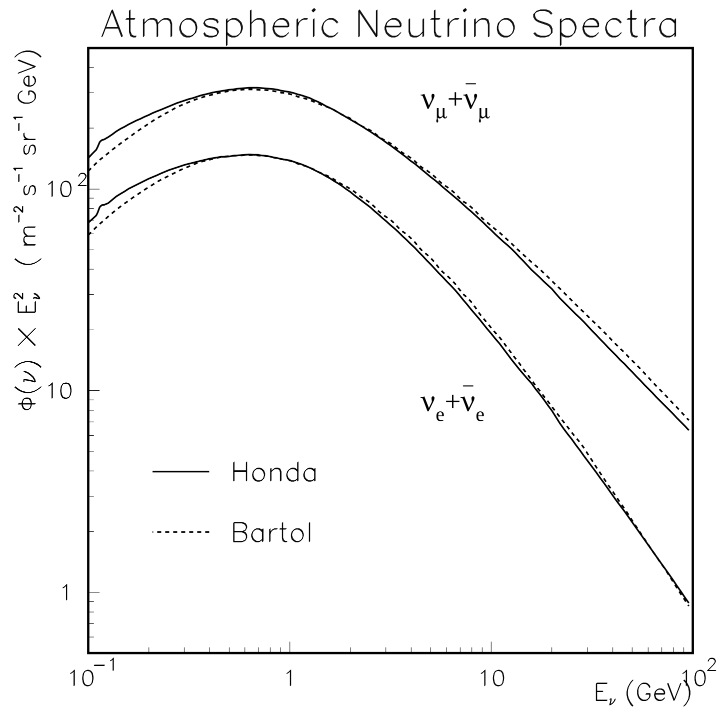

Figure 2.2: The fluxes we use at Super–Kamiokande. Honda is from [50] and Bartol is from [51].

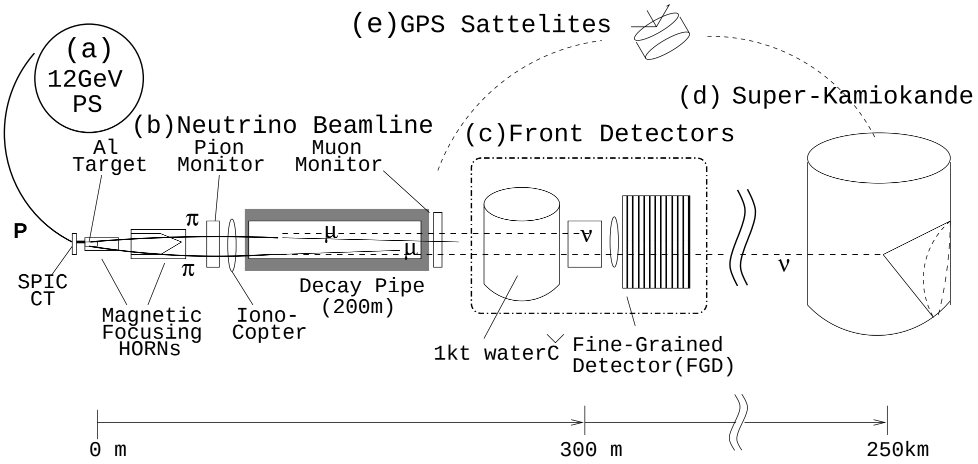

Figure 2.3: Overview of the K2K experiment.

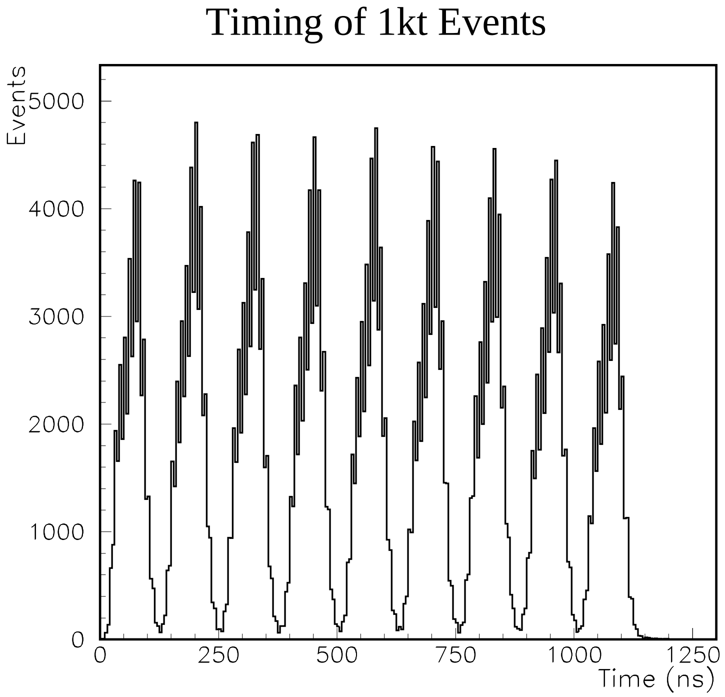

Figure 2.4: The beam structure from events recorded in the 1 kt water Cherenkov detector described in Chapter 3.

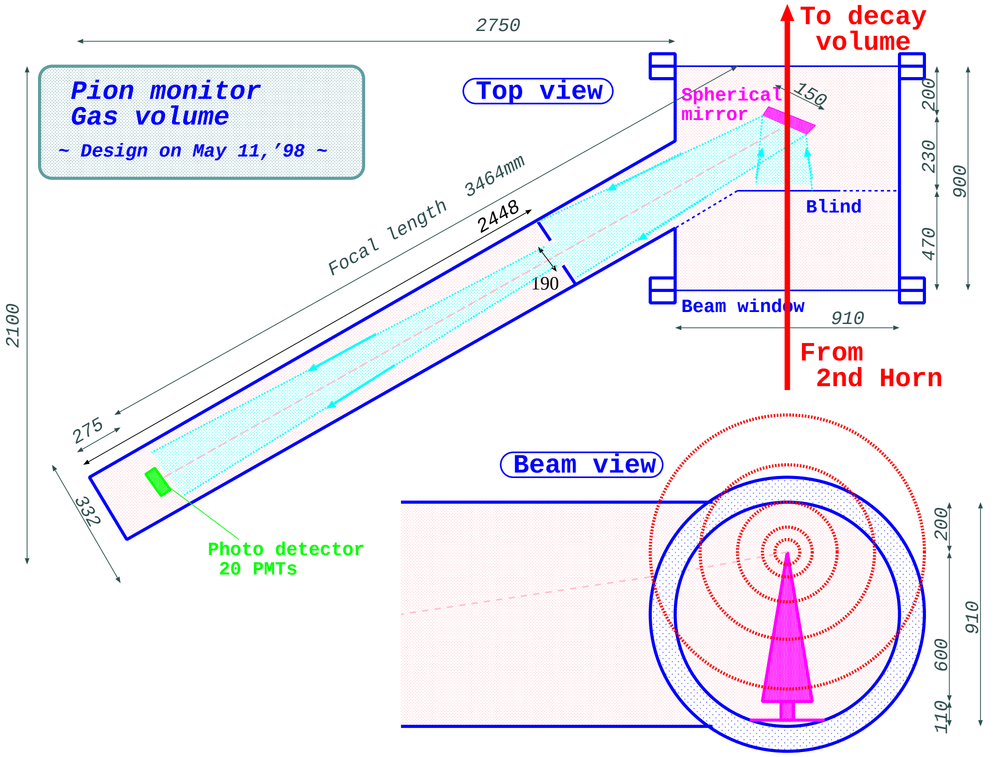

Figure 2.5: The pion monitor.

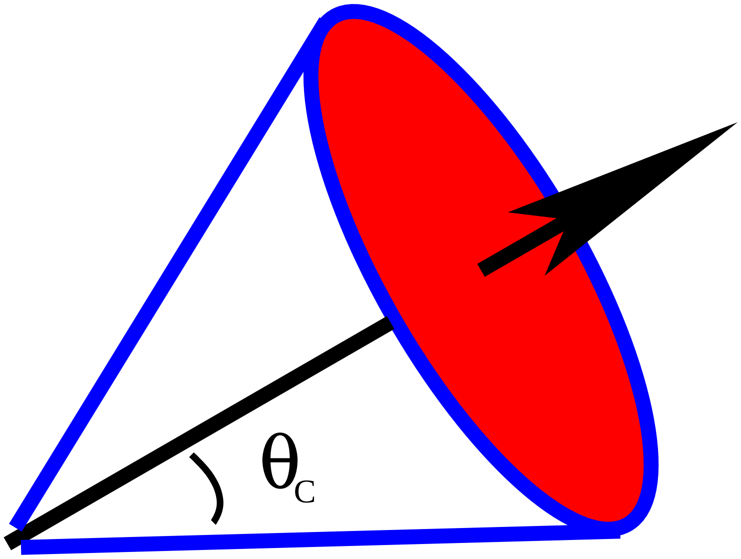

Figure 2.6: Cherenkov radiation.

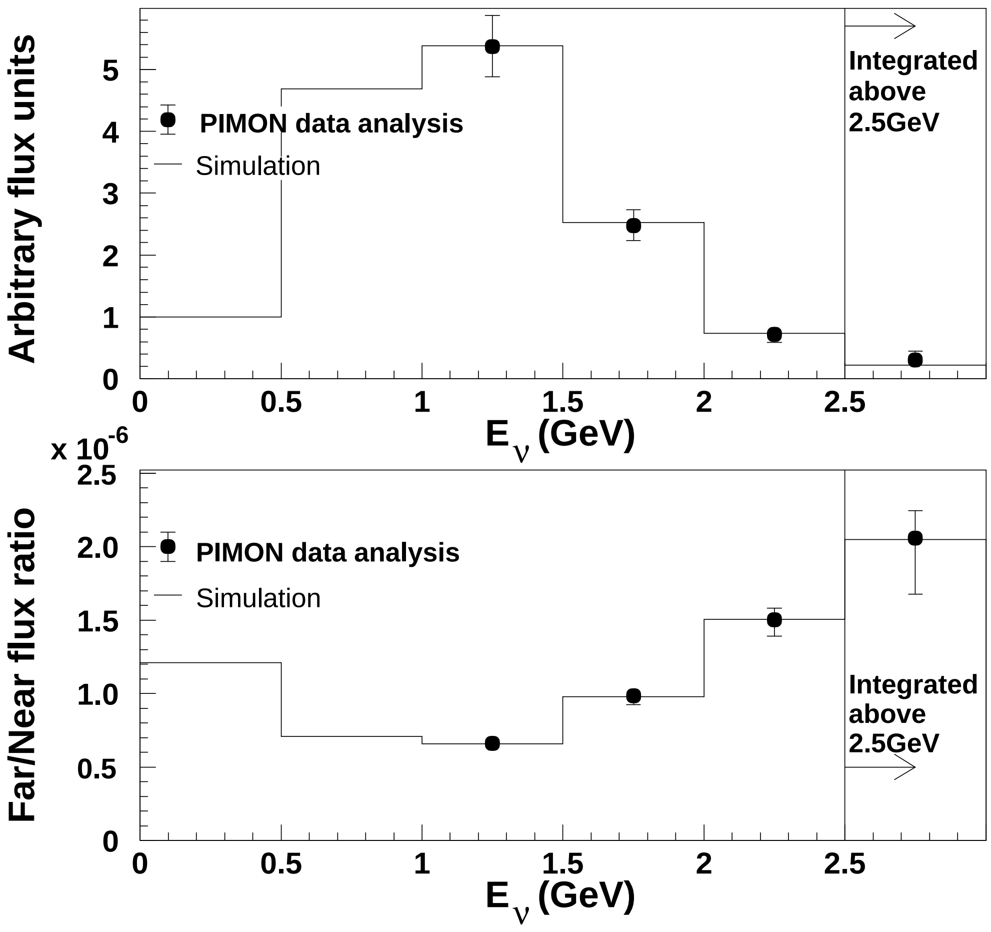

Figure 2.7: The K2K neutrino spectrum from MC studies at low energy and pion monitor data at higher energies. The far/near ratio is a measure of the difference in K2K beam fluxes at Super–Kamiokande (250 km away) and at the near detector array.

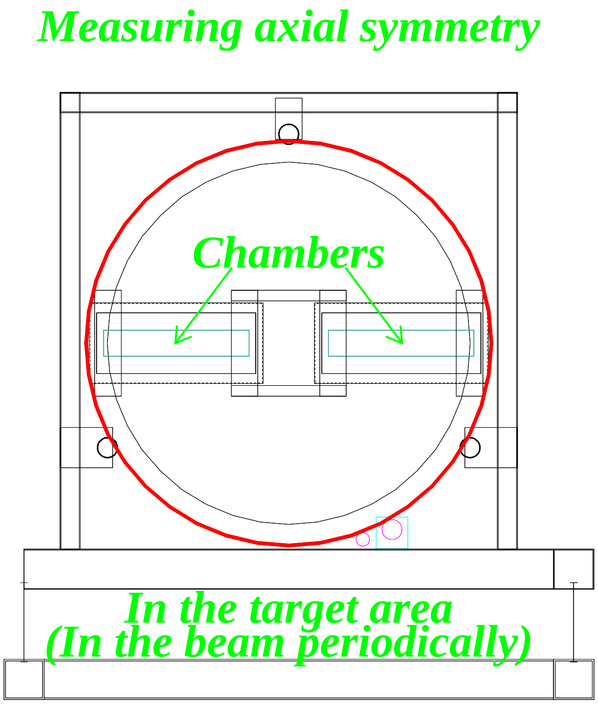

Figure 2.8: The ionocopter.

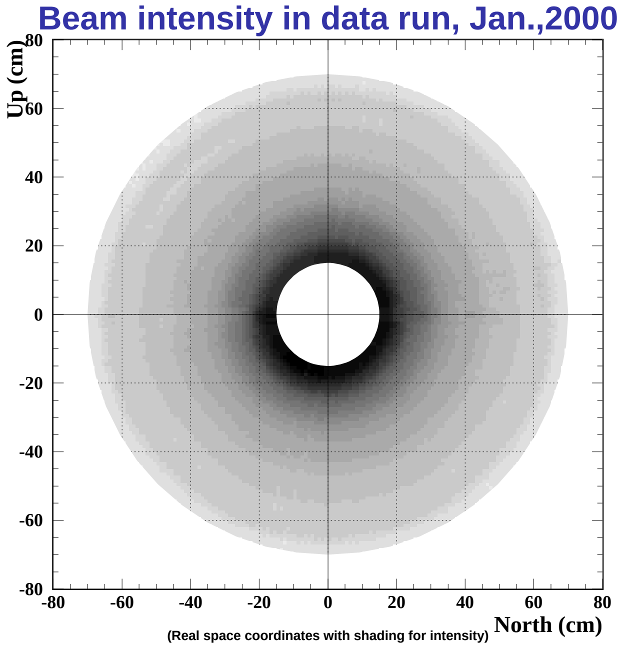

Figure 2.9: The ionocopter data.

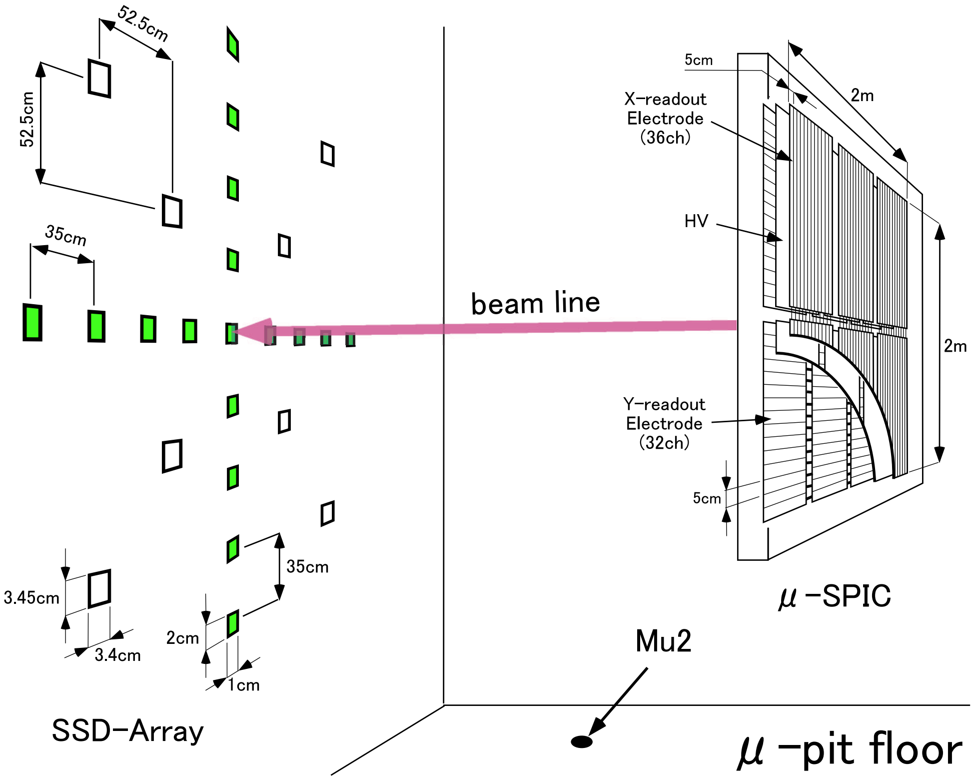

Figure 2.10: The muon monitor.

Chapter 3

Super–Kamiokandeand K2K 1kt Water Cherenkov Detectors

Both detectors used for studying R_{π^0} are large water Cherenkov detectors. Super–Kamiokande (SK) is the largest water Cherenkov detector in the world. It has been used to study a variety of topics from particle physics, cosmic ray physics and astrophysics. The 1 kiloton water Cherenkov detector (1kt) is a smaller version of SK and is part of an array of near detectors for the K2K long baseline neutrino experiment.

3.1 Water Cherenkov Methodology

The primary advantage of water Cherenkov detectors is their size. Water is inexpensive and its transparency makes it an excellent optical medium. Since photo-detectors arranged on the surface can detect light produced in the center, one can increase the mass of a detector while only incurring a $(mass)^{2/3}$ increase in the cost of photo-detectors.

Cherenkov radiation was described in the previous chapter as arising from a charged particle traveling faster than the speed of light in a medium. Since water has an index of refraction of $\sim 4/3$, when particles have a speed $\beta \geq 3/4$, they will produce Cherenkov radiation at a characteristic angle, θ_C, with the following distribution:

$$\frac{d^2N}{dxd\lambda} = \frac{2\pi\alpha}{\lambda}\left(1 - \frac{1}{\beta^2 n^2(\lambda)}\right) = \frac{2\pi\alpha}{\lambda}\sin^2\theta_c,$$

where α is the fine structure constant, λ is the wavelength of the emitted light, and x is the path of the particle. While θ_C depends on the β of a particle, in practice, we observe particles which are very energetic such that β is almost

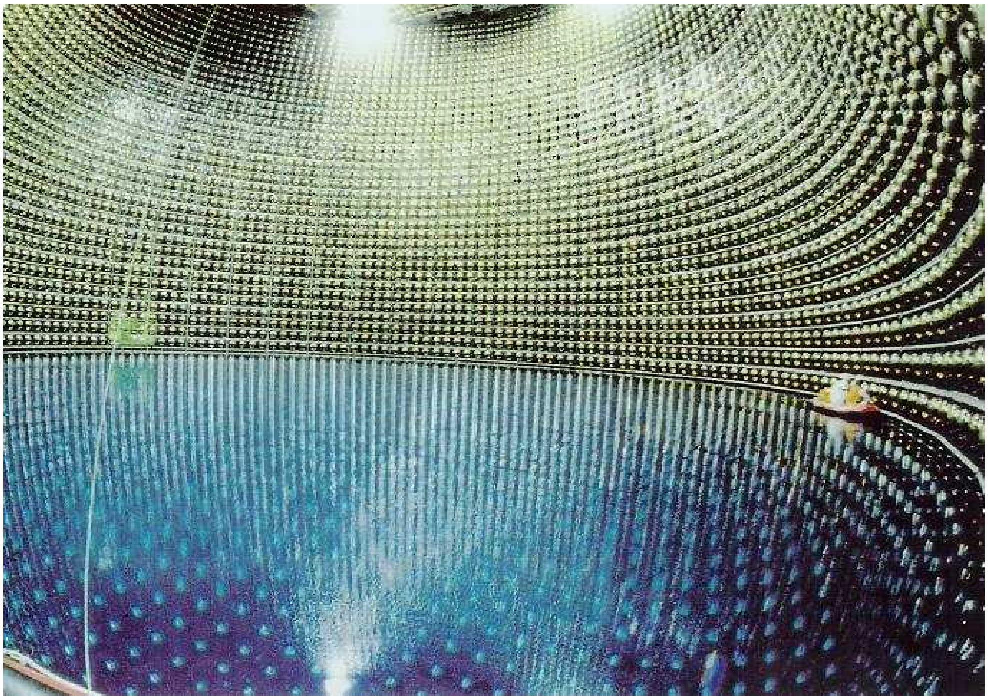

Figure 3.1: Super–Kamiokande while being filled in 1996.

always $\simeq 1$. In water, the maximum Cherenkov angle with $\beta = 1$ is 42°.

3.2 SK Detector

Super–Kamiokande is a 50 kiloton water Cherenkov detector located in the Kamioka Mine in Kamioka Town, Gifu Prefecture, Japan. Kamioka is a small town in the foothills of the Japanese Alps and borders the town of Osawano in Toyama Prefecture. Most people working at the experimental site live in Osawano.

A stainless steel cylindrical tank, $41.4m$ high and $39.3m$ in diameter contains the water. Figure 3.1 shows a photograph of the detector while undergoing water filling.

Inside, the tank is divided into three concentric cylinders by a stainless steel frame about $2m$ from the walls of the tank (Figure 3.2). The inner detector (ID) employs 11,146 inward facing 20 inch PMTs mounted on the inside of the frame to monitor an inner volume and is $36.2m$ in height and $33.8m$

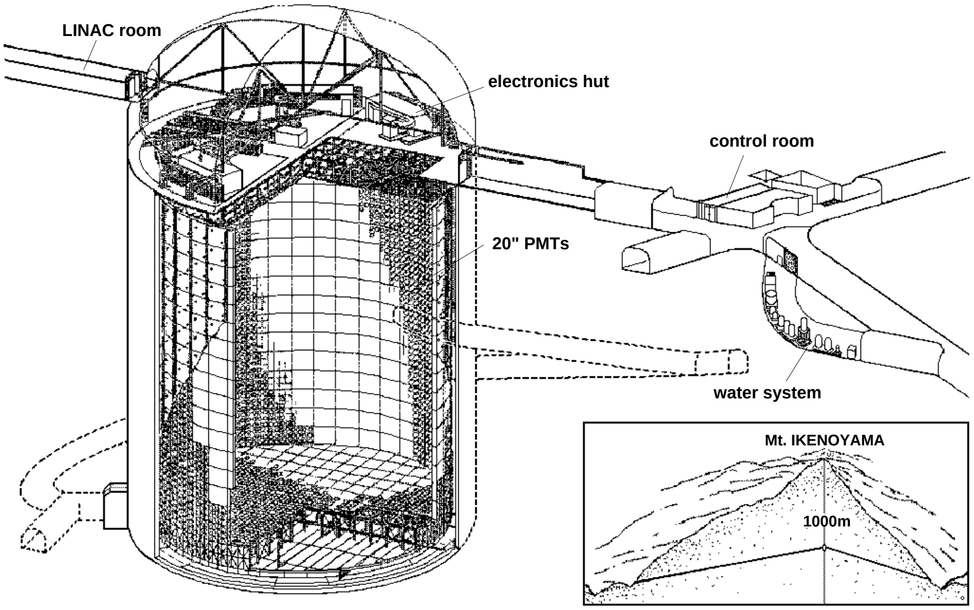

Figure 3.2: Super–Kamiokande.

in diameter. The outer detector (OD) employs 1885 8 inch PMTs mounted on the outside of the frame and facing outwards towards the wall of the tank. The volume of the $55cm$ thick frame is called the dead zone. To optically separate the three volumes, the surface between inner PMTs is covered by black, opaque, plastic sheeting as shown in Figure 3.3. The photocathode coverage in the inner side is 40 %. The OD photocathode coverage is only 1 %, so several methods are employed to increase light collection in the OD. The large spaces between PMTs are covered with tyvec sheeting with polyethylene coated on one side. The coated side is black and is on the side of the sheeting facing the inner volume. The uncoated side is white to reflect light and maximize its collection. The outer walls of the detector are covered with white tyvec. To increase light collection even further, mounted onto each PMT is a $60cm \times 60cm$ wavelength shifter plate. Since the intensity of Cherenkov radiation increases with decreasing wavelength, there are many Cherenkov photons in the UV range. The wavelength shifter plates collect many of these photons and convert them to the visible light. By total internal reflection, many of these photons then strike the photocathode of the PMTs. Figure 3.4 shows the top portion of the outer detector with the OD PMTs, the wavelength

Figure 3.3: The Inner PMTs with black sheeting.

shifter plates and everything else covered in white tyvec. Figure 3.5 shows a portion of the wall of the OD underwater.

The fiducial volume for the atmospheric neutrino analysis is defined by a cylinder concentric with the inner volume such that its boundary is 2m away from the plane of the PMT faces, which comprises the 22.5 *kton* fiducial volume. Most physics measurements are made using this fiducial volume. The OD is used primarily to veto incoming charged particles and tag outgoing charged particles.

3.2.1 The PMTs

A schematic of the custom-built 20 inch ID PMTs is shown in Figure 3.6. The PMTs are coated with a bialkali (Sb-K-Cs) material on the inner surface of the hemispherical face and is kept at ground because of its proximity to the water. Near the neck of the PMT is the 11-stage, Venetian blind dynode

Figure 3.4: The OD PMTs on the top.

structure. The end of this structure is the anode. When photons strike the surface of the PMT, they free an electron about 22 % of the time (the quantum efficiency is 22 % for $\lambda = 390nm$). The electron is then accelerated toward the dynode structure by the applied high voltage. The ratio of applied voltage is $8 : 3 : 1 : \ldots : 1$, where 8 is from the photocathode to the first dynode, 3 is from the first dynode to the second and 1 is for all subsequent stages. The Venetian blind structure allows for high collection efficiency ($\sim 70\%$) while maintaining good timing resolution. At the operating voltage of $\sim 2000V$, the gain is 10^7 and the transit time from cathode to anode is $90ns$ with a spread of $\sigma \sim 2.8ns$. The PMT was custom designed for SK. More details of the design of this PMT can be found in Ref. [54].

The quantum efficiency as a function of wavelength is shown in Figure 3.7. While the intensity of Cherenkov radiation is higher for lower wavelengths, the quantum efficiency of the PMTs drops to zero for UV wavelengths.

The OD PMTs and the wavelength shifter plates were recycled from the IMB experiment. The OD PMTs were also made by Hamamatsu and are similar to the ID PMTs, but the transit time spread is about $11ns$. This is

Figure 3.5: The OD PMTs on the side while under water.

further smeared because of the wavelength shifter plates. The plates increase the collection efficiency by about 60 %.

3.2.2 The Water System

A defining feature of Super–Kamiokande is the ultra-pure water which is the active target. Beginning as spring water inside Mt. Ikenoyama, it is filtered of particles large and small and cleansed of radioactive elements. Water is mostly recirculated with a small amount of new water added each cycle to replace losses. Water is taken from the top of the detector and fed to the bottom. Figure 3.8 shows a schematic of the water system which circulates about 50 tons per hour. The key elements are:

- $1\mu m$ Filter: Removes small particles.
- Heat Exchanger: Maintains water at $14°C$.
- Ion Exchanger: Removes ions.

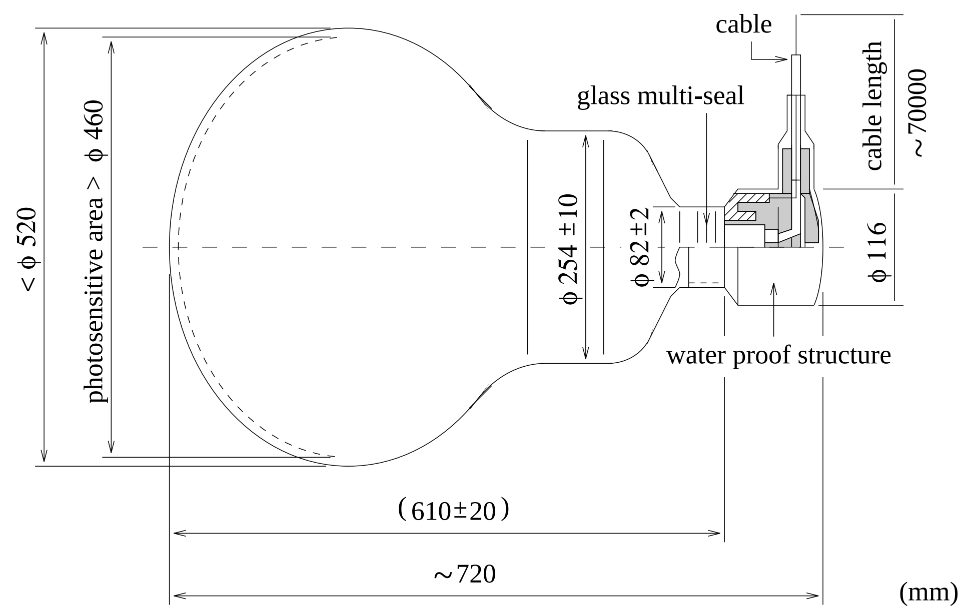

Figure 3.6: The ID PMTs.

- Ultra-Violet Sterilizer: Kills any bacteria.
- Vacuum De-gasifier: Removes dissolved gases, primarily oxygen and radon.
- Cartridge Polisher: Second stage of ion reduction.
- Ultra-Filter: Very fine filter removes particles to $\sim 10nm$.
- Reverse Osmosis: Water which doesn't make it through the Ultra-Filter is put through reverse osmosis before being returned to the system.

3.2.3 Electronics

The quantities important from each PMT are the time the light arrived and amount of light which struck the surface. This is recorded as time in nanosec-

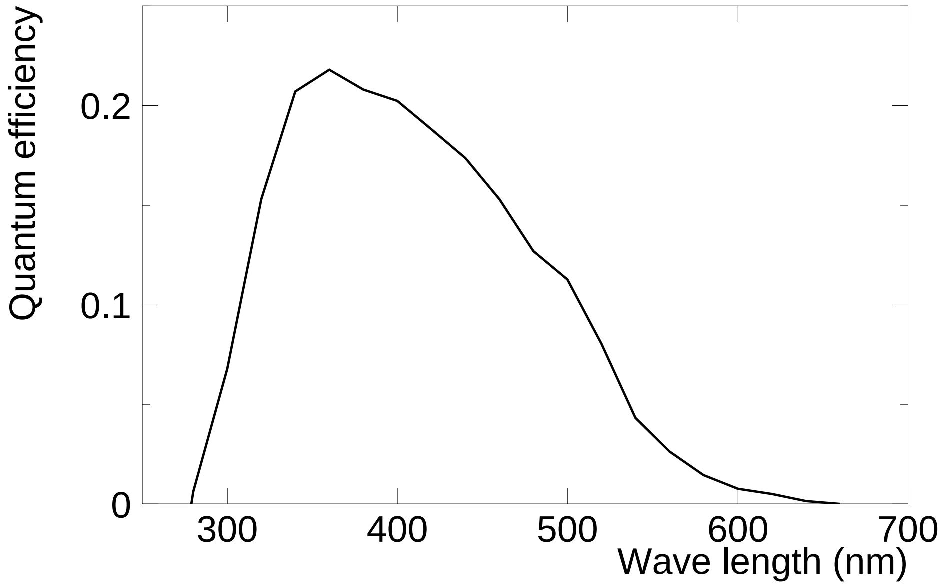

Figure 3.7: The ID PMT Quantum Efficiency.

onds and charge in units of photo-electrons (p.e.) - the number of electrons ejected by photons at the photo-cathode. The ID electronics are designed to record and process this information. A schematic of the ID electronics is shown in Figure 3.9. Signals from the PMTs are processed by a custom electronics module called an ATM (Analog Timing Module). The PMT signal is fed into the ATM and split. One branch is fed into a discriminator with the level set at 1/4 (p.e.). If the discriminator threshold is exceeded, a HITSUM signal is produced and sent to the global trigger module. In the meantime, the other branches of the split PMT signal lead to a charge to analog converter and a timing to analog converter. If a global trigger is issued, these signals will be digitized and sent to a VME memory module called Super-Memory-Partner (SMP). From there, they are collected by workstations and finally collected by the online host computer which creates an event.

The HITSUM signals are 200 ns in length and 15 mV high. When the sum of HITSUM signals exceeds 320 mV, a global trigger is issued. This corresponds to 29 PMT hits which is equivalent to a $5.7 MeV$ electron event. While trigger efficiency is an important issue for solar neutrino analyses, at-

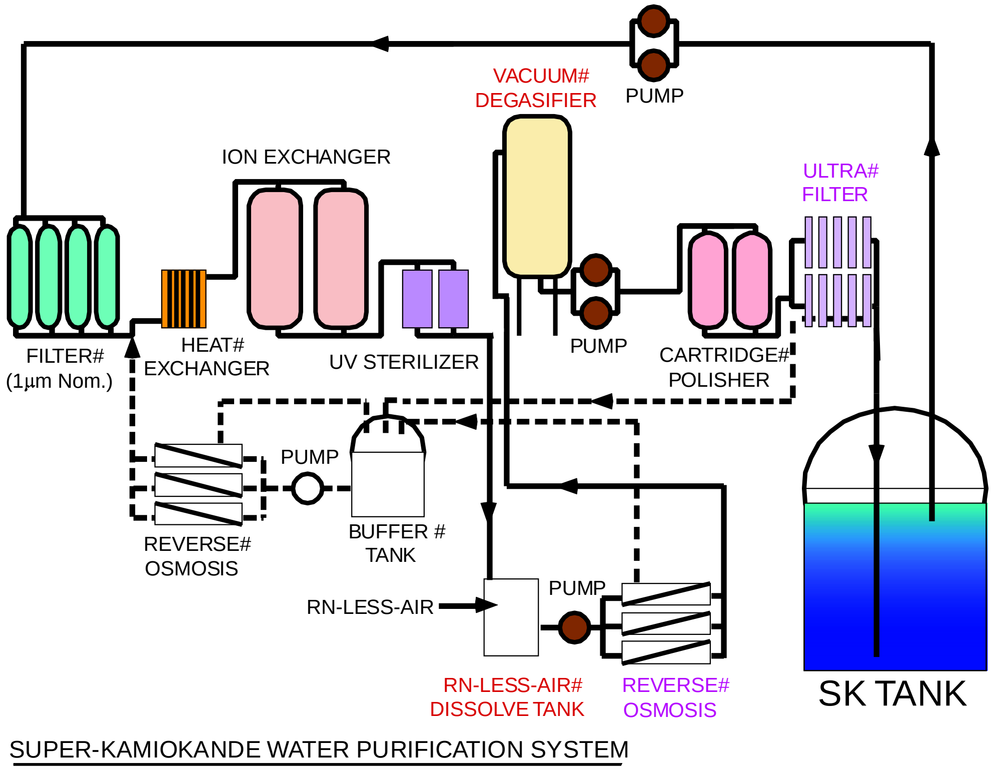

Figure 3.8: The water purification system.

mospheric neutrino events used for analysis have minimum visible energies of $\sim 100 MeV$, so the trigger efficiency is 100 %.

It is important to note, for each PMT, there are two channels on the ATMs labelled A and B. Signals from two successive events, for example, a muon and decay electron, can be digitized simultaneously to minimize dead-time.

The OD PMTs are processed by different electronics. The signals are collected by QTC(charge to timing converter) modules. The QTCs emit pulses whose lengths are proportional to the amount of charge. The timing information is determined by the leading edge of the pulse. These signals are fed into TDC(time to digital converter) modules which convert the leading edges and lengths into time and charge information. This is then sent to a VME memory module and collected by a workstation. Finally, the information is sent to the online host computer which includes the OD information in the events it builds.

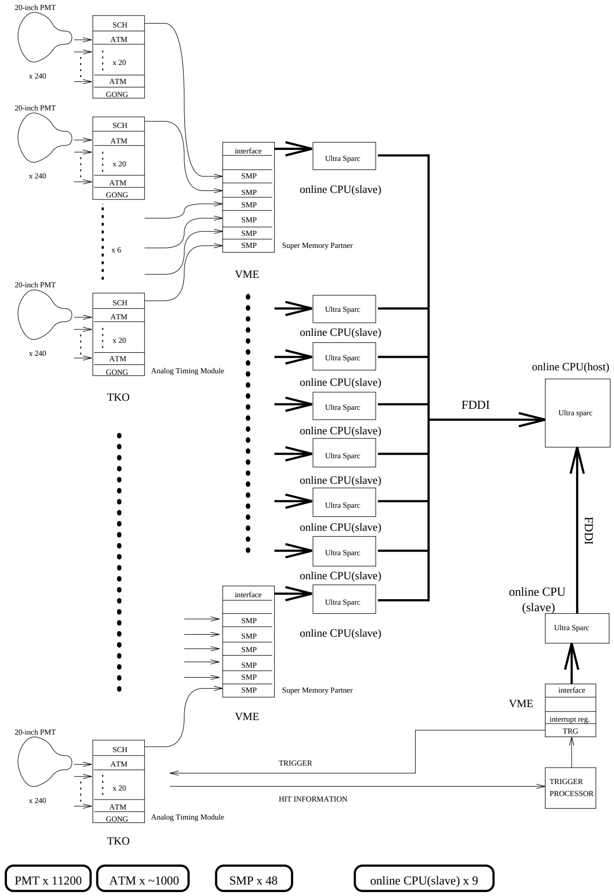

Figure 3.9: Super–Kamiokande DAQ with arrows showing the flow of data.

3.3 1kt Detector

Located about 300m downstream of the pion production target is the 1 kton imaging water Cherenkov detector (1kt). As one of the near detectors, its primary purpose is to measure the ν_μ interaction rate and energy spectrum. It can also be used to study neutrino interactions in an energy range important for atmospheric neutrino analyses. The K2K near detector array at KEK is shown in Figure 3.10.

The 1kt detector is quite similar to Super–Kamiokande (Figure 3.11). The PMTs, electronics, tyvec and black sheeting are the same. The differences are as follows. First of all, the tank is smaller. It is a cylindrical tank 10.8m high and 10.8m in diameter. The inner volume is 8.6m high and 8.6m in diameter

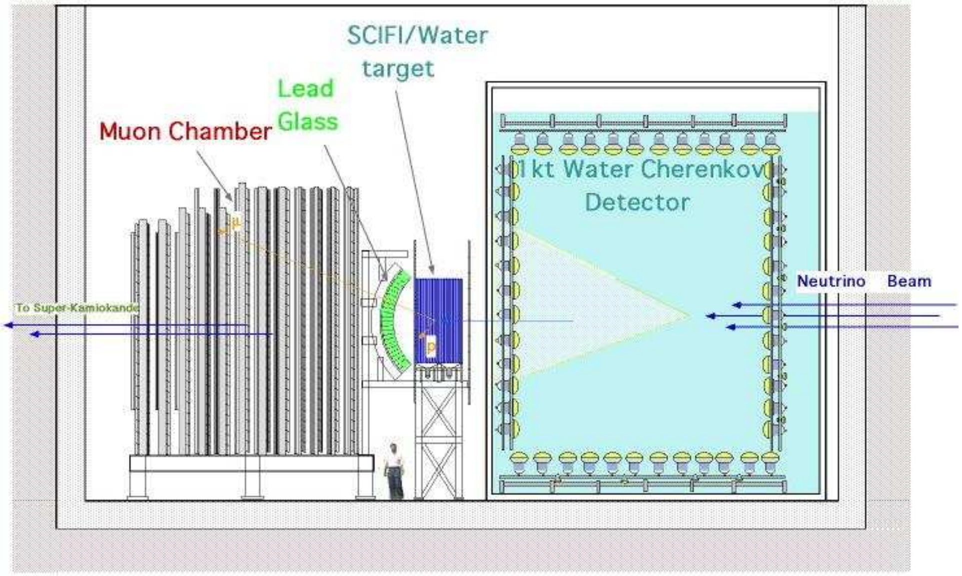

Figure 3.10: The K2K Near Detector Array.

and is viewed by 680 PMTs. Next, the outer detector is only instrumented on the bottom and on the side in the upstream direction. The side has 42 PMTs while the bottom has 26 PMTs. As such, the whole inner volume is offset by about 0.5m in the downstream direction, allowing more space between the upstream wall and the surface of the OD PMTs as can be seen in Figure 3.10. Also, the OD PMTs are connected to ATMs just like the ID PMTs. The electronics for the OD and ID are totally integrated.

The last major difference between SK and the 1kt is the PMTSUM, which is the analog sum of all ID PMTs is put into a flash ADC. With a sampling speed of 500 MHz and 8-bit dynamic range, the flash ADC is used to record what is happening globally in the detector before and during the beam spill. It allows us to veto spills where more than one event occurs in the detector. The average number of events per spill - including those due to cosmic rays and beam-induced muons - is 0.2, so about 10 % of events with at least one event have two or more events.

Figure 3.11: 1kt Detector.

3.4 Calibrations

While the devices and electronics of water Cherenkov detectors are fairly simple, calibration of the detectors is crucial. There are three types of calibrations carried out:

- The PMTs themselves.
- The properties of the water.
- The energy response of the detector.

Using very low light level sources, the 1 p.e. distribution is checked to find the relationship between measured charge and p.e. Then, the timing and charge response of each PMT is measured. Calibration of the water means measuring the water transparency. Events which occur such that the Cherenkov light does not go very far before being detected by the PMTs will be measured to have more light than those where the Cherenkov light has traveled all the way across the detector and had more chance to be absorbed or scattered. While this is a small effect in the 1kt detector, in SK it is a serious issue. Finally, the energy response of the detector is measured using various sources. The question we answer with these measurements is how do the number of photoelectrons correlate with the visible energy of an event? The descriptions and figures which follow are from Super–Kamiokande; however, the same methods were used in the 1kt.

3.4.1 PMTs

To measure the 1 p.e. distribution, we employ a nickel-californium source. The ^{252}Cf source provides neutrons which thermalize in the water and are captured on the nickel which then emits a gamma ray. The spectrum of gamma rays is $6 \sim 9MeV$, so only 1 p.e. is expected for each hit tube. From this measurement, we determined 2.055 pC from a PMT corresponds to 1 p.e.

Using a Nitrogen-Dye laser with a $3ns$ long pulse, a TQ(time-charge) map is made for each channel. The laser light is injected into a diffuser ball which is placed inside the detector. The intensity of the light is controlled by attenuation filters. A sample TQ map is shown in Figure 3.12.

Each PMT came with its own specified operating voltage from the manufacturer, Hamamatsu. However, we adjust this voltage according to in situ measurements of the relative gain. As shown in Figure 3.13, we employ a Xenon lamp with filters to change the intensity of the light supplied to a scintillator ball. The ball is placed in many locations in the tank and the charge for each PMT is corrected based on its distance from the source, the PMT acceptance, and the light intensity measured by a monitoring PMT located near the Xenon source. The result from measurements at the beginning of running in 1996 are shown in Figure 3.14. Since 1996, many subsequent measurements have been made to monitor the relative gain stability. The spread in Figure 3.14 has increased over the years by 10% to 7.7%.

3.4.2 Water transparency: direct, muons

Water transparency has been measured and monitored in a variety of ways. The two most important are the direct measurement and the cosmic-ray muon method. Direct measurement requires stopping data taking, while the cosmic ray muon measurement uses events already in the data stream. Consequently, cosmic ray muons are used to monitor the attenuation length change over time. It is important to note, the meaning of attenuation length is slightly different for each method, so a direct comparison of these results is not meaningful. The

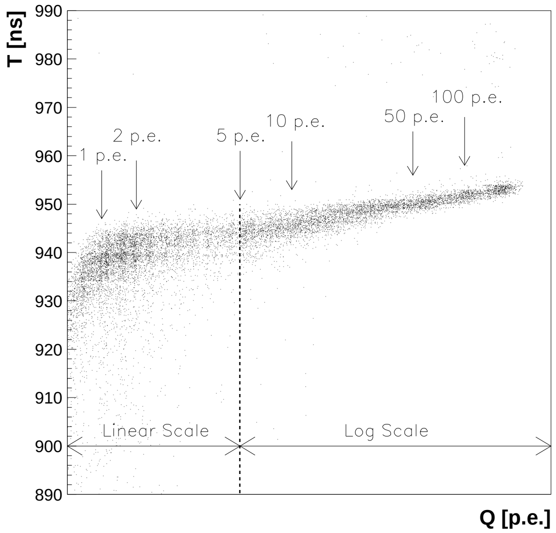

Figure 3.12: A sample TQ map. Higher T means earlier time. As light levels increase, hits are earlier and the timing resolution is better.

cosmic ray muon method employs Cherenkov light which has a broad spectrum of wavelengths, whereas the direct method uses monochromatic light. In addition, the fraction of scattered light measured by each method is different.

Among water Cherenkov experiments, the direct method of measuring water transparency is unique to Super–Kamiokande. The water attenuation length is the combined effect of scattering and absorption on the intensity of light some distance away from a source. It can be parameterized as follows:

$$I = I_0 exp(-(\alpha_{abs} + \alpha_{scat})x).$$

$$\lambda_{atten} = \frac{1}{\alpha_{abs} + \alpha_{scat}}$$

Figure 3.15 shows the apparatus used for the direct measurement. We use a laser, a diffuser ball, and a CCD camera to measure λ_{atten}. The diffuser ball is lowered into the the water and illuminated with the laser via a fiber optic cable (See Figure 3.15). The ball is then imaged with the CCD camera.

While early measurements were made using a Nitrogen-Dye laser, subse-

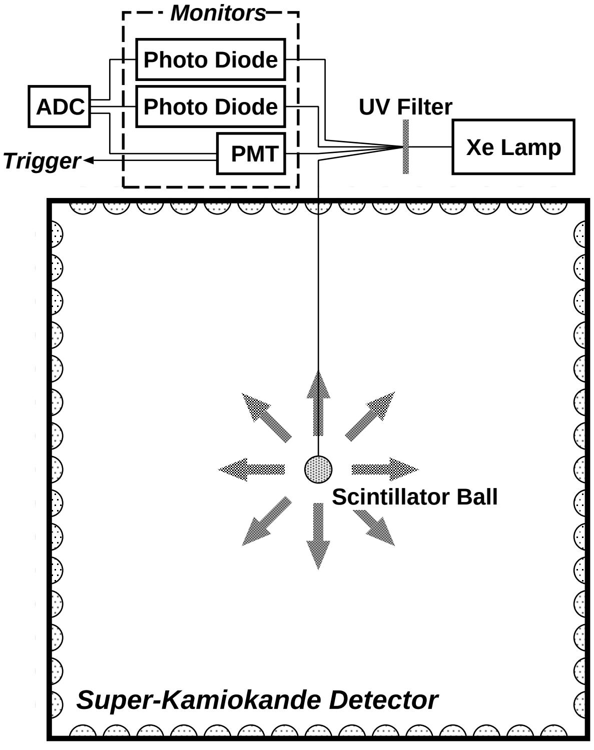

Figure 3.13: The relative gain measurement setup.

quent measurements were made using a Titanium-Sapphire laser and second harmonic generator. The tunable Titanium-Sapphire laser is pumped with an Nd:YAG laser. We obtained output energies of 2 to 3 mJ per pulse at a wavelength of 420 nm. These energies are considerably higher than those we reached with the Nitrogen-Dye laser. By using the second harmonic generator, we probed the attenuation length with wavelengths between 350 and 500 nm. The laser stability is monitored with a PMT. Measurements are made at various depths. For each diffuser ball position, the intensity measured by the CCD camera is divided by the total number of ADC counts from the PMT monitor system to account for any shifts in laser intensity.

Results from one set of measurements are shown in Figure 3.16. While results over time are shown with values used in the detector simulation in Figure 3.17.

Despite having a protective shell of $1000m$ of rock overhead, there are still $2.7Hz$ of cosmic ray muons entering the detector. They provide a useful cali-

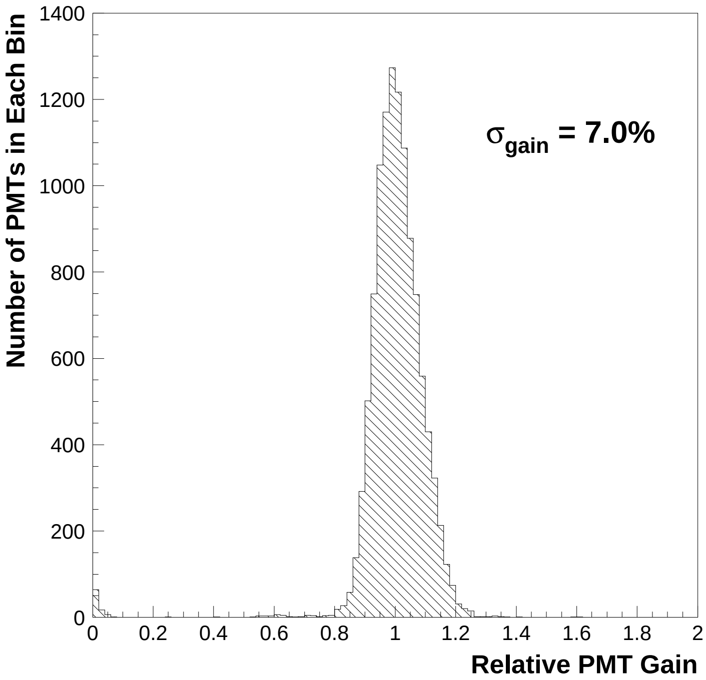

Figure 3.14: The relative gain measurement in 1996. The corrected charge, normalized by the mean is plotted for all PMTs.

bration source, not only to monitor water transparency, but also to determine the absolute energy scale.

Through-going muons, those which have an entry and an exit point in the detector, deposit almost constant energy along their path. We use them as a constant light source. We select muons which enter through a circular region of the top of the inner detector which is concentric with the detector with a radius of $15.9m$. We also require them to exit through the bottom of the inner detector through another concentric circle of the same radius. We further require the entry and exit point to be at roughly the same position in each concentric circle ($< 5m$). If we assume the light is not scattered before arriving at the PMTs, the charge Q observed at any PMT is:

$$Q = Q_0 \frac{f(\theta)}{l} \exp \frac{-l}{L}$$

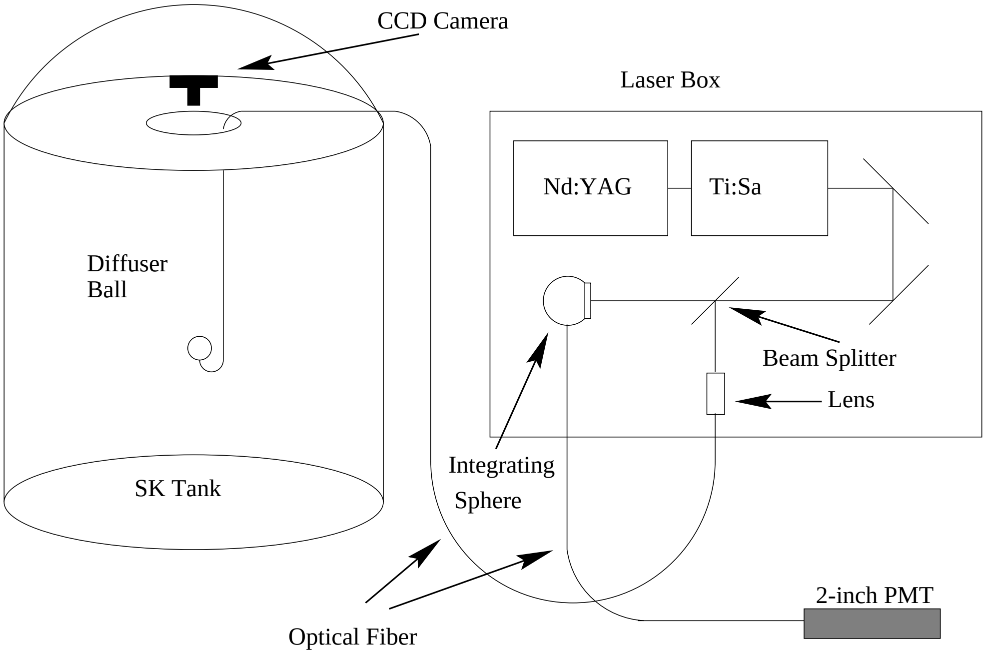

Figure 3.15: Direct water attenuation length measurement apparatus

where l is the path-length, L is the attenuation length, Q_0 is a constant, and $f(\theta)$ is the PMT acceptance function. This function is fit to data to obtain and estimate of L. An example is shown in Figure 3.18.

3.4.3 Energy Calibration

While Super–Kamiokande has several methods at its disposal to measure the absolute energy scale, four are important for atmospheric neutrinos. First, the Michel spectrum of muon decay electrons can be compared between data and MC and is useful for visible energies up to $60 MeV$. Next, since the single-π^0 signal is so clean, the invariant mass peak can be used as a calibration source. Because there are many energies of π^0's, this method tests the reliability of our energy scale over several hundred MeV. Next, because the Cherenkov angle of a particle depends on its momentum, the momentum of low energy stopping muons can be estimated independent of the total charge of an event. Finally, the momentum of high energy stopping muons can be calculated by their range in the detector. The entry point can be fit and the stopping point can be found by fitting the position of the subsequent de-

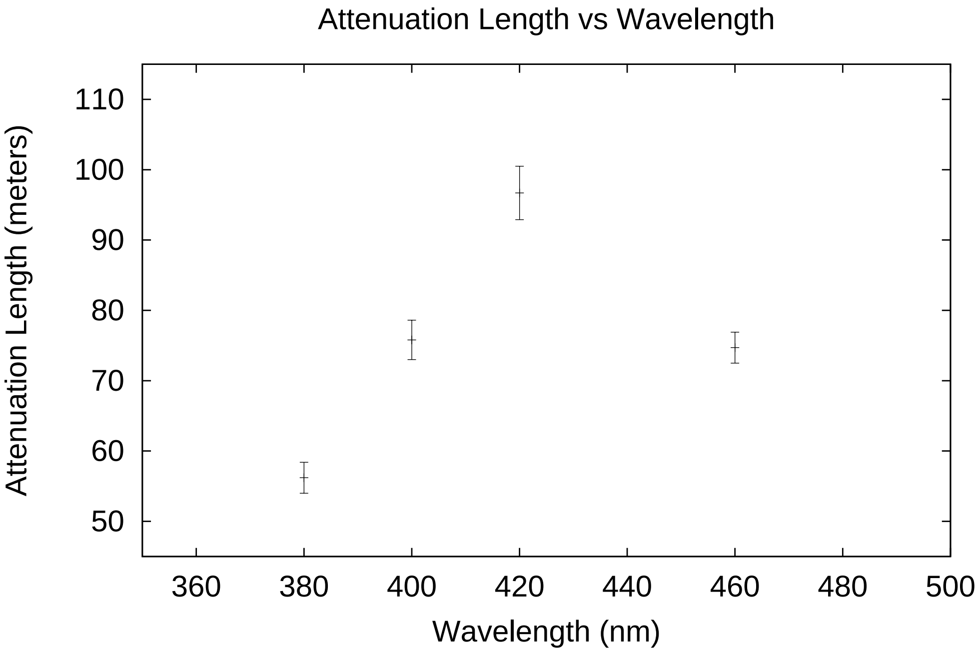

Figure 3.16: Water attenuation length results from one set of measurements.

cay electron. We compare the momentum calculated by their range with the charge they deposit in the detector.

Figure 3.19 shows the decay electron spectrum. While the distributions are similar for data and MC, their mean values differ by about 2 %.

While π^0's are discussed in much greater detail later in this thesis, it is worth mentioning here the difference of the peak positions of data and MC of the π^0peak is within 2 %.

Stopping muons with momenta below $400 MeV/c$ have Cherenkov angles which depend on their momenta. We make a ratio R of measured momentum by charge to calculated momentum by Cherenkov angle. We then compare the R values of data and MC as shown in Figure 3.20 shows a result. The deviation is less than 1 % and the difference between data and MC is less than 1.5 %.

We estimate the momenta of high energy stopping muons by measuring their range. For stopping muons with a path-length of greater than $7m$ in Super–Kamiokande, the measured momentum by charge per unit path-length is shown in Figure 3.21. Though the data is systematically lower than the MC

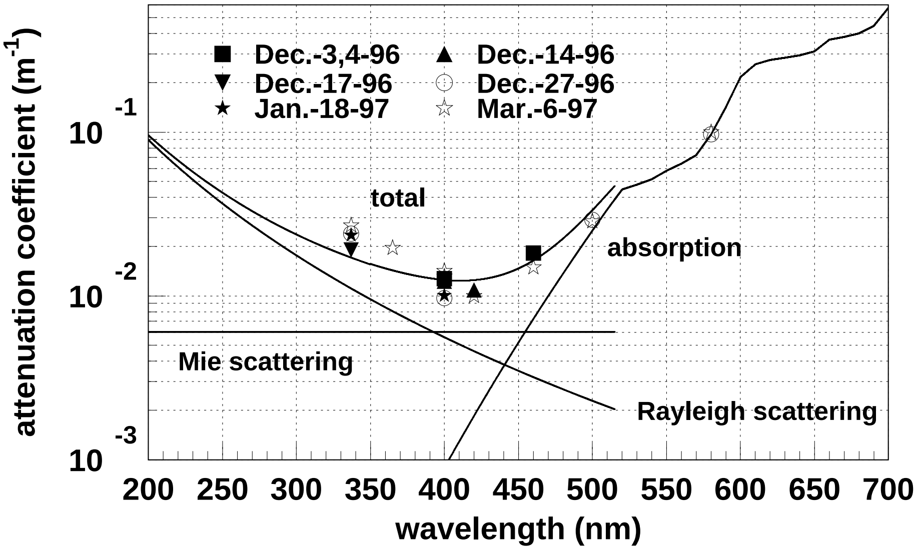

Figure 3.17: Water attenuation length measurements (points) with the model used in the detector simulation (lines).

by 2.5 %, the deviation over the range for each is less than 1 %.

By the above measurements including the π^0 mass peak described later. We are confident we understand our absolute energy scale to within ±5%.

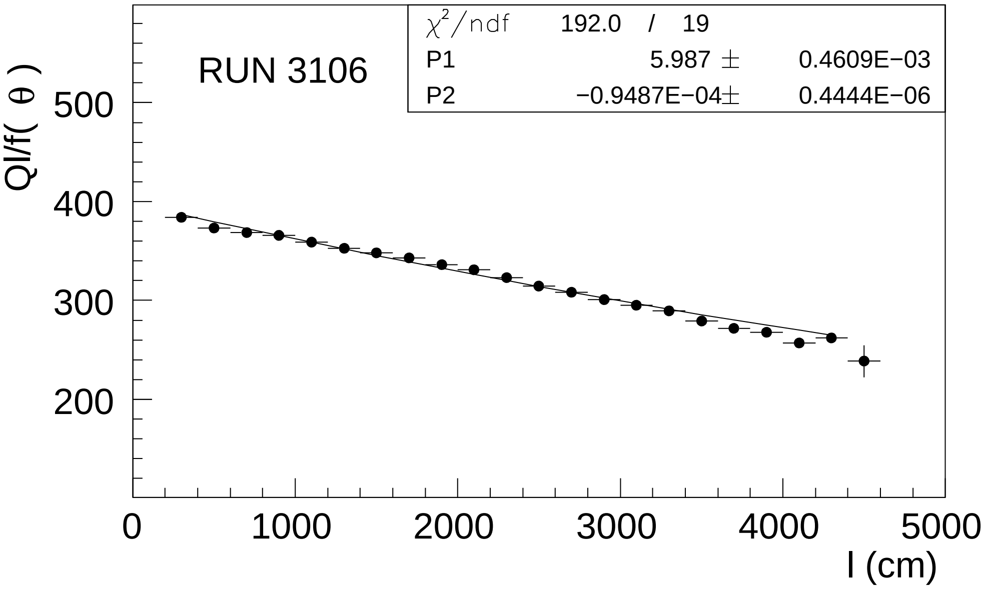

Figure 3.18: Effective observed charge as a function of the path-length.

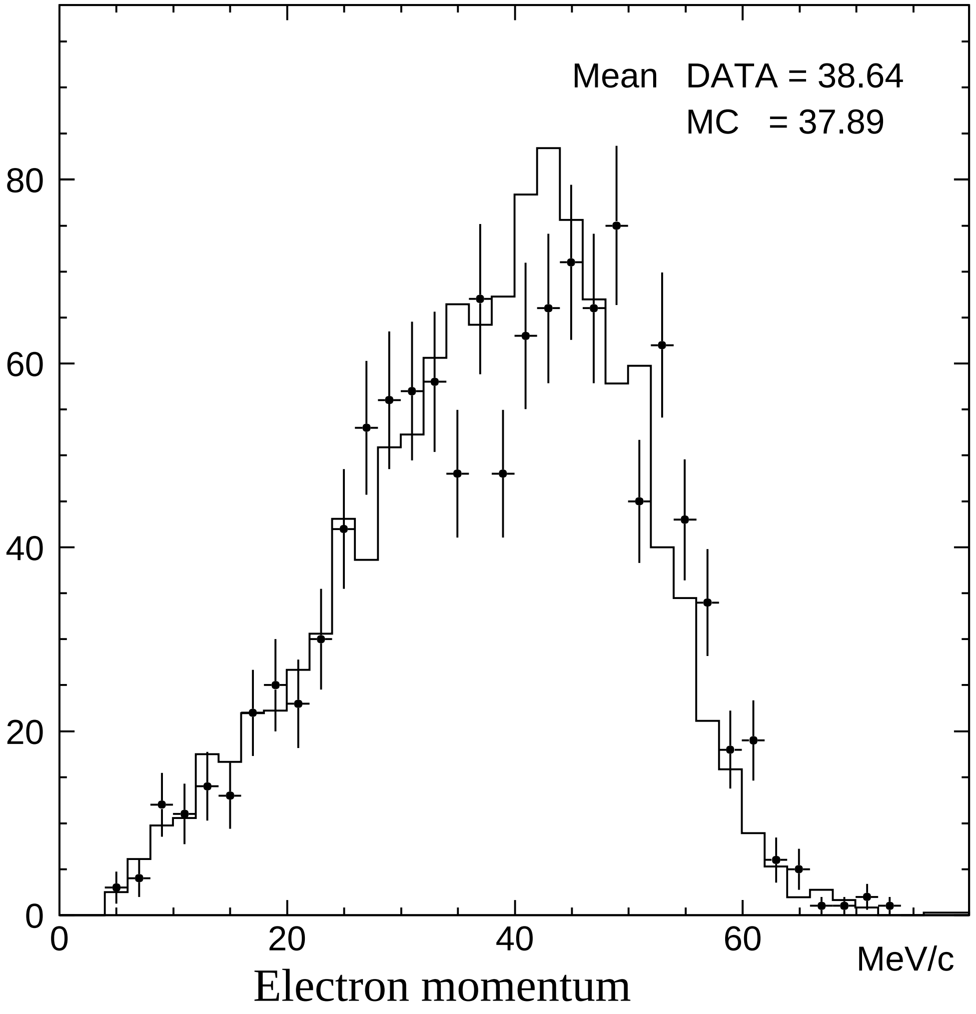

Figure 3.19: Michel electrons from muon decay.

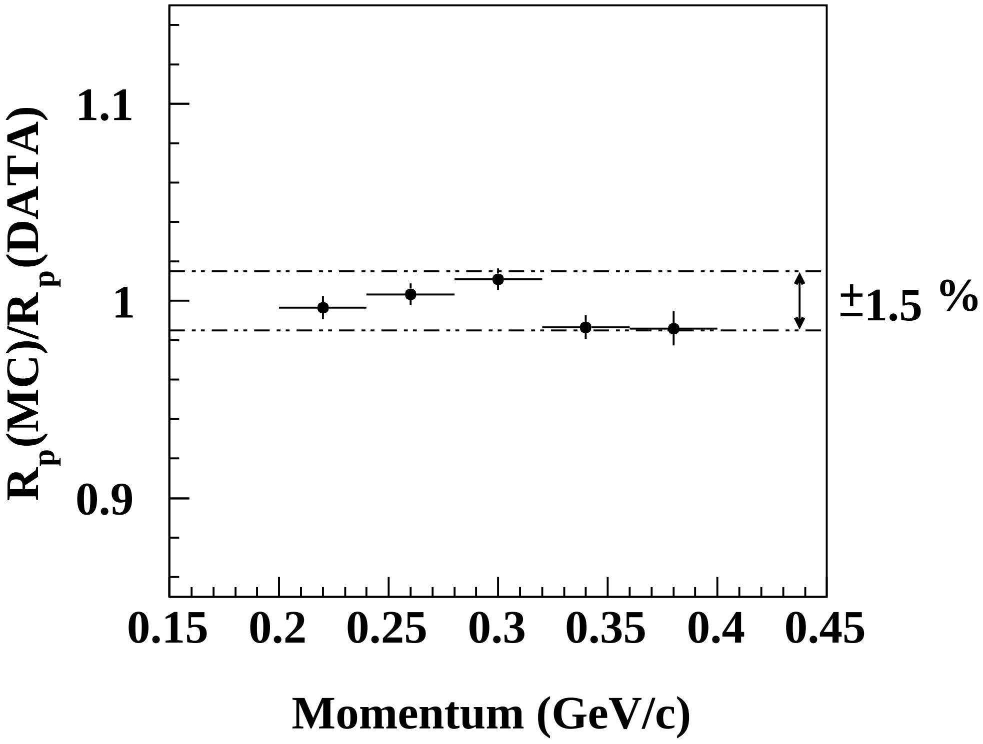

Figure 3.20: Low Energy Stopping muons.

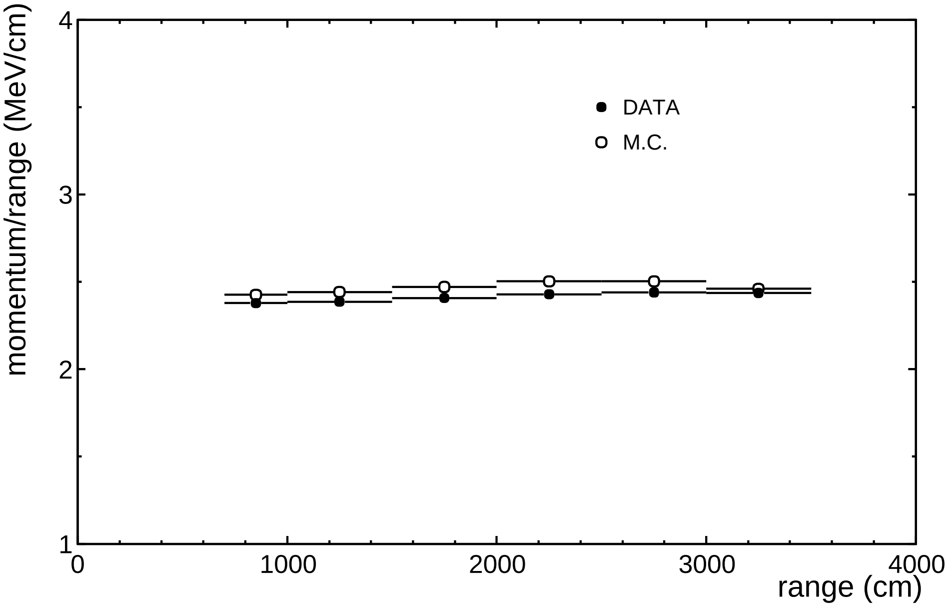

Figure 3.21: High Energy Stopping muons.

Chapter 4

Simulation

Both Super–Kamiokande and K2K use a staged set of programs to simulate real data. As discussed in Chapter 2, SK uses atmospheric neutrino flux predictions from a few theoretical groups [55], while K2K calculates its fluxes based on measurements and beam Monte Carlo simulations. The fluxes are fed into the first stage of the simulation, the interaction MC. Both Super–Kamiokande and K2K use the same interaction MC, called NEUT, which simulates elastic and quasi-elastic scattering [56] (QE), single resonant meson production [57], coherent pion production [58] and multi-pion production [59] in water. The dominant components of the event samples in this analysis are QE interactions and resonant pion production. These "production modes" are used to generate a primary interaction. Since the interaction can take place inside the oxygen nucleus, effects such as binding energy, Pauli blocking and Fermi motion must be taken into account. In addition, nuclear de-excitation, and meson re-scattering and absorption are simulated.

As will be shown, the cross-sections used for many production modes are not well known. Where data are available, the errors are frequently large. Sometimes our model does not agree well with the data. Sometimes the data do not agree well with each other. This accounts for the large systematic uncertainties which we discuss in Chapter 7.

Once particles are out of the nucleus, the detector simulators track them using GEANT [60] and GCALOR [61]. The 1kt detector simulation uses essentially the same SK detector simulation code with a few exceptions. The global geometry had to be modified and the data format had to be changed. We developed a custom electronics simulation to study multi-interaction events. However, since we found their effect to be negligible for most analyses, we use the less CPU-intensive SK electronics simulation for most cases.

4.1 Coherent Pion Production

The interaction considered in NEUT which is least destructive from the standpoint of the oxygen nucleus is coherent pion production.

$$\nu_\mu +^{16} O \rightarrow \nu_\mu(\mu^-) + \pi^0(\pi^+) +^{16} O$$

By definition, the oxygen nucleus remains intact. Since very little momentum is transferred to the nucleus, the outgoing lepton and pion angular distributions are forward peaked.

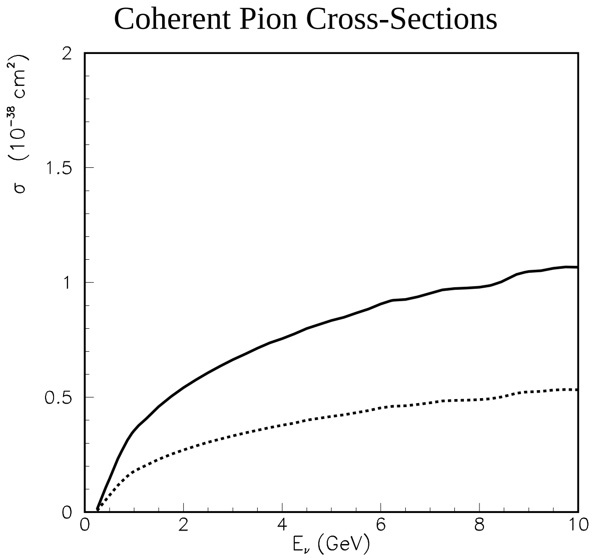

Figure 4.1: The coherent π^0 production cross-sections used in NEUT. The solid line is for CC while the dashed line is for NC.

The differential cross-section is:

$$\begin{aligned}\frac{d^3\sigma}{dQ^2dydt} &= \beta \times \frac{G^2M}{2\pi^2} f_\pi^2 A^2 E_\nu (1-y) \frac{1}{16\pi}[\sigma_{tot}^{\pi N}]^2 \\ & (1+r^2)(\frac{M_A^2}{M_A^2+Q^2})^2 e^{-b|t|} F_{abs}\end{aligned}$$

where β is the axial vector coupling constant and is 1 for NC and 2 for CC interactions. G is the weak coupling constant, M is the nucleon mass, $f_\pi =$

$0.93m_\pi$, A is the number of nucleons (16), E_ν is the neutrino energy, y is the lepton fractional energy loss, $\sigma_{tot}^{\pi N}$ is the averaged pion-nucleon cross-section, $r = \frac{Ref_{\pi N}(0)}{Imf_{\pi N}(0)}$, where $f_{\pi N}(0)$ is the πN scattering amplitude, M_A is the axial mass, Q^2 is the four-momentum transfer of the lepton, $b = 80GeV^{-2}$, t is the four-momentum transfer to the nucleus, and F_{abs} is a factor to account for the absorption of pions in the nucleus. Figure 4.1 shows the cross sections for CC and NC interactions used in NEUT.

4.2 Elastic and Quasi-Elastic Scattering

For both the atmospheric neutrino sample and the K2K beam neutrino sample, QE scattering is the dominant contribution from neutrinos with energies below $1GeV$ and is of the form:

$$\nu\ (\bar{\nu})\ +\ n\ (p)\ \rightarrow\ l^-\ (l^+)\ +\ p\ (n)$$

The differential cross-section is:

$$\frac{d\sigma}{dq^2} = \frac{M^2 G^2 \cos{\theta_c}^2}{8\pi E_\nu^2}[A(q^2) \mp B(q^2)\frac{s-u}{M^2} + C(q^2)\frac{(s-u)^2}{M^4}]$$

where M is the mass of the target nucleon, G is the Fermi coupling constant, θ_c is the Cabbibo angle, E_ν is the neutrino energy, q is the four-momentum transferred of the lepton, and s and u are Mandelstam variables [56]. The factors A, B, and C are:

$$\begin{aligned}
A(q^2) &= \frac{m^2 - q^2}{4M^2}[(4 - \frac{q^2}{M^2})|F_A|^2 \ - \ (4 + \frac{q^2}{M^2})|F_V^1|^2 \\
&\quad - \frac{q^2}{M^2}|\xi F_V^2|^2(1 + \frac{q^2}{4M^2}) \ - \ \frac{4q^2 F_V^1 \xi F_V^2}{M^2} \\
&\quad - \frac{m^2}{M^2}((F_V^1 + \xi F_V^2)^2 + |F_A|^2)] \\
B(q^2) &= \frac{q^2}{M^2}(F_A(F_V^1 \ + \ \xi F_V^2)) \\
C(q^2) &= \frac{1}{4}(|F_A|^2 \ + \ |F_V^1|^2 \ - \frac{q^2}{4M^2}|\xi F_V^2|^2)
\end{aligned}$$

where m is the lepton mass, $\xi \equiv \mu_p - \mu_n = 3.71$. The parameterization of the form factors, F_V^1, F_V^2, F_A, is determined from experiments [62, 63]. The vector form factors are given by:

$$
\begin{aligned}
F_V^1 &= (1-\frac{q^2}{4M^2})^{-1}(1-\frac{(1+\xi)q^2}{4M^2})(1-\frac{q^2}{M_V^2})^{-2} \\
F_V^2 &= (1-\frac{q^2}{4M^2})^{-1}(1-\frac{q^2}{M_V^2})^{-2}.
\end{aligned}
$$

The axial form factor, F_A, is approximated as a dipole:

$$F_A(q^2) = -1.23(1-\frac{q^2}{M_A^2})^{-2}.$$

In the version of NEUT used for this thesis work, M_A is set to 1.01.

Figure 4.2 shows the NEUT cross-section for QE scattering together with data from various experiments. Figure 4.3 shows the same for anti-neutrinos.

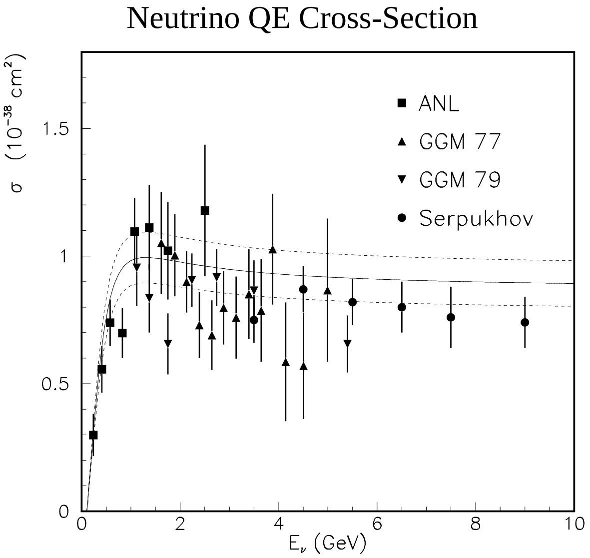

Figure 4.2: The quasi-elastic cross-section used in NEUT for neutrinos shown with data from several experiments [64, 65, 66, 67].

When the target nucleus is hydrogen, the above can be used directly. For the case of oxygen, however, effects such as Fermi motion and Pauli blocking must be considered. Since Fermi motion contributes positively or negatively

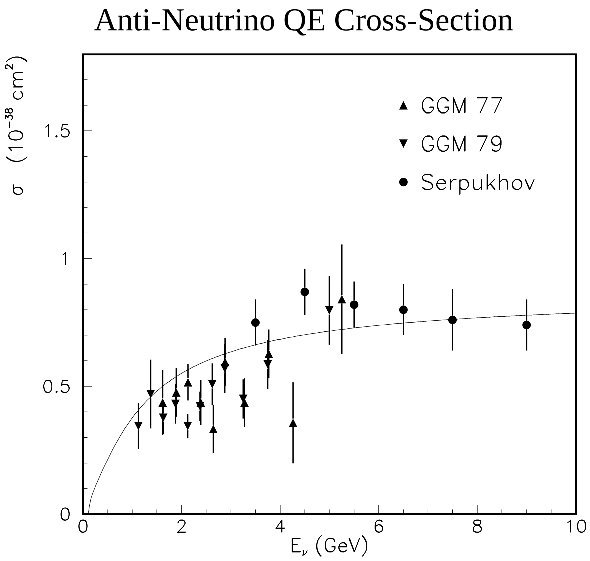

Figure 4.3: The quasi-elastic cross-section used in NEUT for anti-neutrinos shown with data from several experiments (See Figure 4.2 for data references).

to the total energy available for the interaction, the outgoing kinematics are altered. Also, since neutrons and protons are fermions, NEUT requires the outgoing momentum of the nucleon in the interaction to be above the Fermi surface.

NC elastic scattering cross-sections were estimated according to the relations from [68, 69]:

$$\begin{aligned}\sigma(\nu p \to \nu p) &= 0.153 \times \sigma(\nu n \to e^- p)\\ \sigma(\bar{\nu} p \to \bar{\nu} p) &= 0.218 \times \sigma(\bar{\nu} p \to e^+ n)\\ \sigma(\nu n \to \nu n) &= 1.5 \times \sigma(\nu p \to \nu p)\\ \sigma(\bar{\nu} n \to \bar{\nu} n) &= \sigma(\bar{\nu} p \to \bar{\nu} p).\end{aligned}$$

4.3 Resonant Single-Meson Production

As neutrino energy increases, so does the probability to create a meson. Most single-meson production is single-pion production due to the excitation of a $\Delta(1232)$ resonance, for example:

$$\nu + p \;\rightarrow\; \mu^- + \Delta^{++}$$

followed by the decay:

$$\Delta^{++} \;\rightarrow\; p + \pi^+$$

In general, a Δ or N^* resonance is created and subsequently decays into a single meson and a nucleon. In NEUT, this process is "factorized". Using the Rein-Seghal model [57], we calculate the amplitude of producing each resonance. Subsequently, we multiply each amplitude by the probability the corresponding resonance decays into one pion while considering interference effects between the resonances. We restrict our attention to 18 resonances such that the hadronic invariant mass $W < 2.0 GeV$ since above this energy we use a deep inelastic scattering model. The same procedure is also done for kaons and η's.

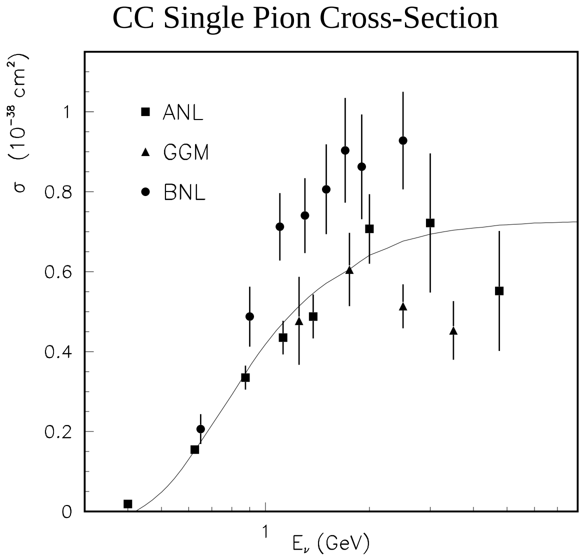

Figure 4.4: The cross-section for $\nu_\mu + p \rightarrow \mu^- + p + \pi^+$. Data are from [70, 71, 72].

NEUT cross-sections with data from several experiments are plotted in Figures 4.4 to 4.6 for CC interactions and Figures 4.7 to 4.10 for NC interactions.

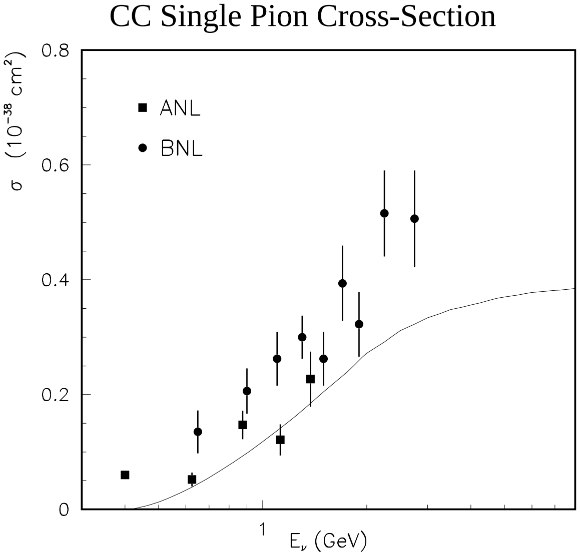

Figure 4.5: The cross-section for $\nu_\mu + n \rightarrow \mu^- + p + \pi^0$. (See Figure 4.4 for data references).

The angular distribution of pions from decay of the $\Delta(1232)$ is taken from Ref. [73], while for isospin 1/2 resonances it is set to be isotropic in the Adler frame, the resonance rest frame.

If the interaction takes place in the oxygen nucleus, pions and other mesons are stepped through the nucleus to account for elastic scattering, charge exchange and absorption. This nuclear effect is described later in the chapter.

In addition, in accordance with Ref. [74], we allow 20 % of Δ's produced in oxygen to decay without producing a pion.

4.4 Multi-π Production and Deep Inelastic Scattering

Deep Inelastic Scattering is simulated using one of two processes. For events with $W > 2.0GeV$, we employ JETSET [75], a common event generator in high energy physics. For $1.3GeV < W < 2.0GeV$, for CC interactions we

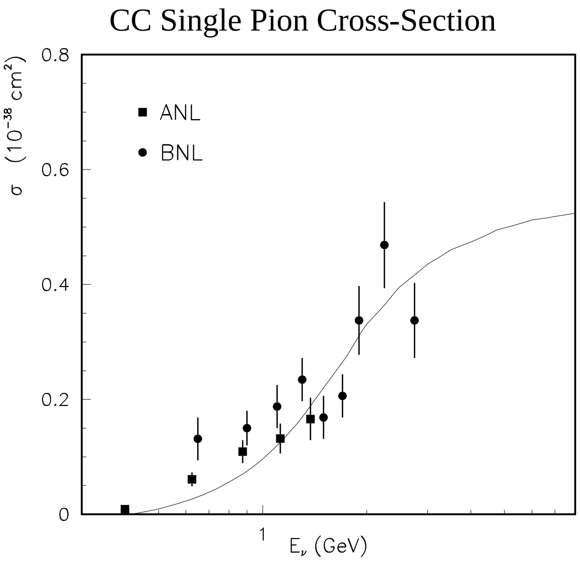

Figure 4.6: The cross-section for $\nu_\mu + n \rightarrow \mu^- + n + \pi^+$. (See Figure 4.4 for data references).

integrate the following equation:

$$\begin{aligned}
\frac{d^2\sigma}{dxdy} &= \frac{G_F^2 M_N E\nu}{\pi}((1-y+\frac{y^2}{2}+C_1)F_2(x,q^2) \pm y(1-\frac{y}{2}+C_2)(xF_3(x,q^2))) \\
C_1 &= \frac{yM_l^2}{4M_N E_\nu x} - \frac{xyM_N}{2E_\nu} - \frac{M_l^2}{E_\nu^2} - \frac{M_l^2}{2M_N E_\nu x} \\
C_2 &= -\frac{M_l^2}{4M_N E_\nu x}.
\end{aligned}$$

In the above, M_l is the outgoing lepton mass, M_N is the nucleon mass, and E_ν is the neutrino energy. For the nucleon structure functions F_2 and xF_3, we use GRV94 [76]. The variables $x = -q^2/(2M_N(E_\nu - E_l))$ and $y = (E_\nu - E_l)/E_\nu$ are the Bjorken scaling variable and the fractional energy transferred to the hadronic system respectively.

The mean multiplicity of pions is estimated using the result of the Fermilab 15-foot bubble chamber experiment [77]:

$$\langle n_\pi \rangle = 0.09 + 1.83 \log W^2.$$

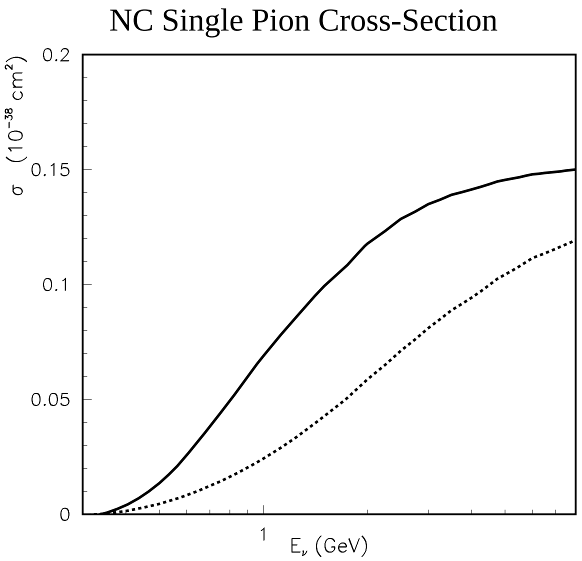

Figure 4.7: The cross-section for $\nu_\mu + p \to \nu_\mu + p + \pi^0$.

For an individual event, the pion multiplicity is determined by KNO (Koba-Nielsen-Olesen) scaling [78]. Figure 4.11 shows our simulation compared with BEBC data. Also, to prevent double counting with the single-pion code, pion multiplicities are restricted to $n_\pi \geq 2$. No such restriction is in place for the JETSET generated DIS events since $W \geq 2.0$. The forward backward asymmetry of the pions in the hadronic center of mass system was including using results from the BEBC experiment [79]:

$$\frac{n_\pi^F}{n_\pi^B} = \frac{0.35 + 0.41 \log W^2}{0.5 + 0.09 \log W^2}.$$

NC multi-pion cross-sections in the $1.3GeV < W < 2.0GeV$ range are determined using the following relations estimated from experimental results [80, 81]. For neutrinos:

$$\begin{aligned} \frac{\sigma(\nu N \to \nu X)}{\sigma(\nu N \to \mu^- X)} &= 0.26 \ (for\ E_\nu \leq 3\ GeV), \\ &= 0.26 + 0.04 \times \frac{E_\nu - 3}{3} \ (for\ 3\ GeV < E_\nu < 6\ GeV), \end{aligned}$$

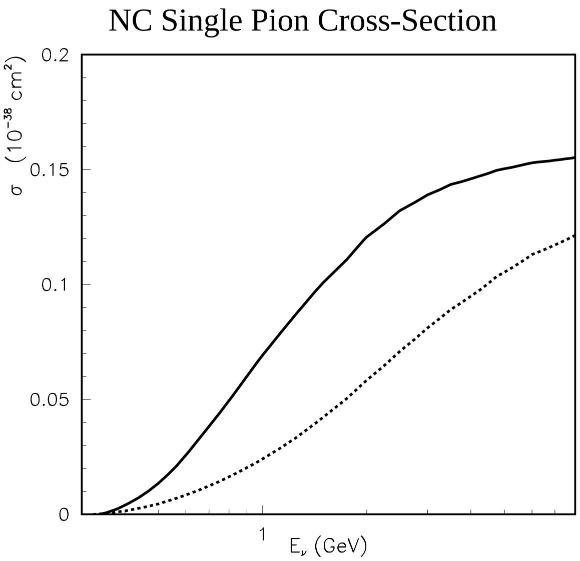

Figure 4.8: The cross-section for $\nu_\mu + n \rightarrow \nu_\mu + n + \pi^0$.

$$= \; 0.30 \; (for \; E_\nu \geq 6 \; GeV).$$

For anti-neutrinos

$$\begin{aligned} \frac{\sigma(\bar{\nu}N \rightarrow \bar{\nu}X)}{\sigma(\bar{\nu}N \rightarrow \mu^+X)} &= 0.39 \; (for \; E_\nu \leq 3 \; GeV), \\ &= 0.39 - 0.02 \times \frac{E_\nu - 3}{3} \; (for \; 3 \; GeV < E_\nu < 6 \; GeV), \\ &= 0.37 \; (for \; E_\nu \geq 6GeV). \end{aligned}$$

4.5 Nuclear Effect

If a neutrino interaction takes place in the oxygen nucleus, NEUT tracks all hadrons until they exit or are absorbed in the nucleus. This is critical for pions because they have very large interaction probabilities. All interactions are tracked using a cascade model.

First, the location of the interaction in the nucleus is chosen using the

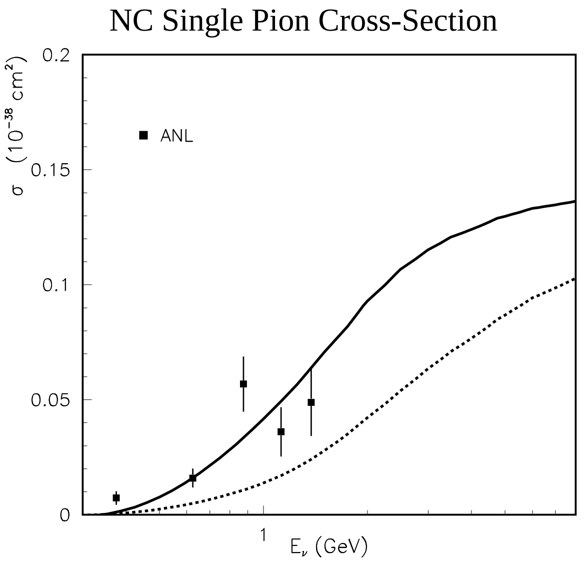

Figure 4.9: The cross-section for $\nu_\mu + n \to \nu_\mu + p + \pi^-$. (See Figure 4.4 for data references).

Woods-Saxon density distribution:

$$\rho(\mathbf{r}) = \frac{1}{2}\bar{\rho}[1 + \exp\left(\frac{|\mathbf{r}| - c}{a}\right)]^{-1}$$

where $\bar{\rho}$ is the average density of the nucleus (set to $0.48m_\pi^3$ for oxygen), and a and c are density parameters of the oxygen nucleus (set to $0.41fm$ and $2.69fm$ respectively). The 1/2 is actually from a Z/A factor in the Woods-Saxon density distribution.

In the case of pions, mean-free-paths are calculated using the model of Oset et al. [82]. They depend not only on the pion momentum, but the position of the pion in the nucleus. Should an interaction occur, Fermi motion is considered and Pauli blocking is enforced. For all interactions, the outgoing nucleon must be above the Fermi surface:

$$p_F = [\frac{3}{2}\pi^2\rho(\mathbf{r})]^{-1/3}.$$

To determine the angular and momentum distribution of outgoing pions from

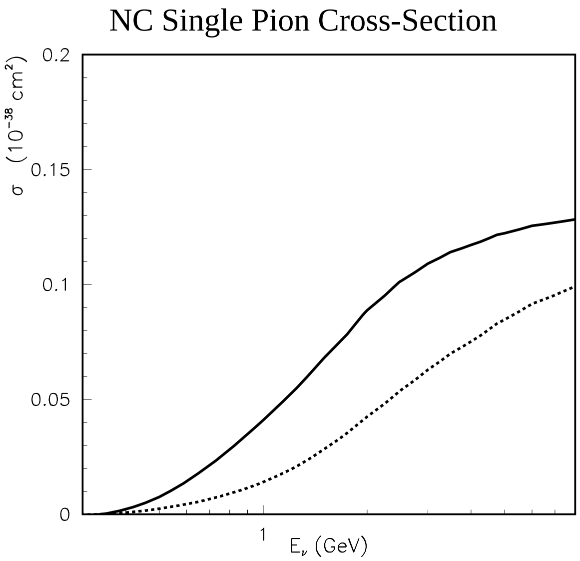

Figure 4.10: The cross-section for $\nu_\mu + p \to \nu_\mu + n + \pi^+$.

reactions inside the nucleus, we use the πN phase shift analysis results from experiment [83].

NEUT uses the results of two experiments to simulate charge exchange and elastic scattering interactions for kaons [84, 85, 86].

η's can be absorbed by nucleons leading to the N^* resonances 1540 and 1650 which can decay into a nucleon and one or two pions [87]. Pions are then tracked as described above.

Finally, using the results of nucleon scattering experiments [88], NEUT considers elastic scattering and one and two delta production processes for nucleons traveling through the oxygen nucleus [89]. Again, pions resulting from delta decays are tracked as above.

4.6 Detector Simulation

The SK and 1kt detectors are simulated using almost identical GEANT based code [60]. Particles are tracked through the detector using GEANT. Hadronic interactions are simulated using CALOR [61] except for pions of $p \leq 500 MeV/c$ where we have developed a custom program based on the

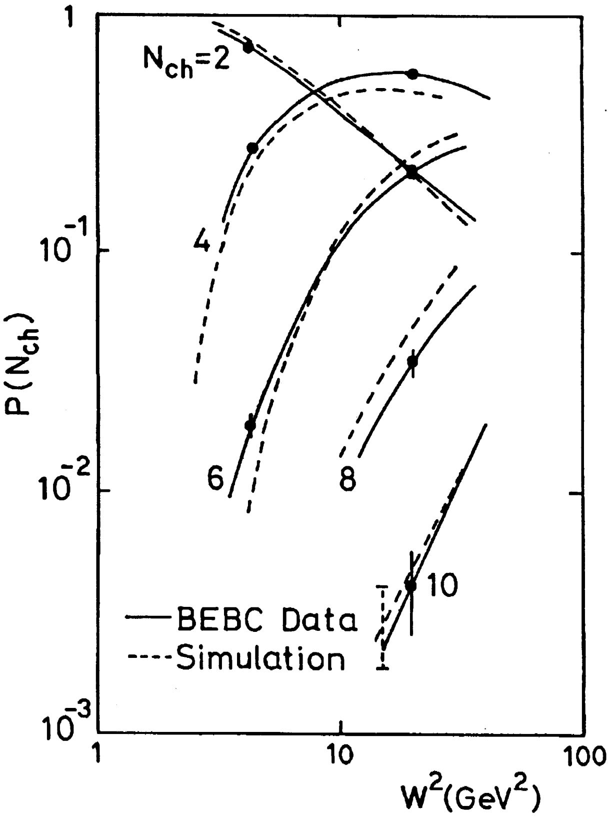

Figure 4.11: KNO scaling.

results of πH_2O scattering experiments [90]. In the custom simulation, we treat elastic and inelastic scattering, charge exchange and absorption processes.

While Cherenkov photons are produced by GEANT, we use a custom program to track them through the detector. The program includes Rayleigh and Mie scattering and absorption as were shown in Figure 3.17. The attenuation lengths used in the program are from the direct measurements described in section 3.4.2. The relative proportion of Rayleigh and Mie scattering is determined by comparing MC with various calibration sources, especially cosmic ray muons.

Simulated data are written out in ZBS format, a ZEBRA based format [91]. Real data are written in the same format so all reduction and reconstruction programs can be run on both.

Chapter 5

Data Reduction and Reconstruction

Super–Kamiokande developed a reduction and reconstruction to identify several different classes of events shown in Figure 5.1. The four types of events are fully contained (FC), partially contained (PC), entering events and penetrating events. To be fully contained, an event must have its vertex inside the defined fiducial volume and all charged particles must remain inside the inner volume. PC events also have their vertices inside the fiducial volume, but at least one charged particle exits the inner detector. Entering events are ones where a charged track enters the inner volume from outside the detector and stops inside the inner volume. Most of these are stopping cosmic ray muons though if the track enters from below the horizon it is probably a muon created by an atmospheric neutrino interacting in the rock below the detector. Finally, through-going events are muons which enter and exit the inner volume. Most through-going muons are cosmic ray muons, but again, if they are upward-going, they were created in the rock below the detector by an atmospheric neutrino interaction. Since atmospheric neutrinos detected at SK are energetic, radioactive backgrounds cause almost no problem. The two large sources of background which must be removed by the reduction are cosmic ray muons and "flashers". Flashers are PMTs which spark due to an instrumentation problem inside of the PMT. The photons from the spark can be detected by the surrounding PMTs and trigger the detector. If this takes place in the ID, there may be no hits in the OD and the event might be classified at FC.

Though the 1kt detector is not protected by a $1000m$ rock overburden, cosmic rays are a manageable problem because the $1.2\mu s$ beam spill comes only once every 2.2 seconds. Flashers pose no problem. There are additional sources of background which SK does not have. Neutrinos can interact in the soil upstream from the 1kt detector creating beam-induced muons which enter the detector during the beam spill. Also, the neutrino beam intensity is quite

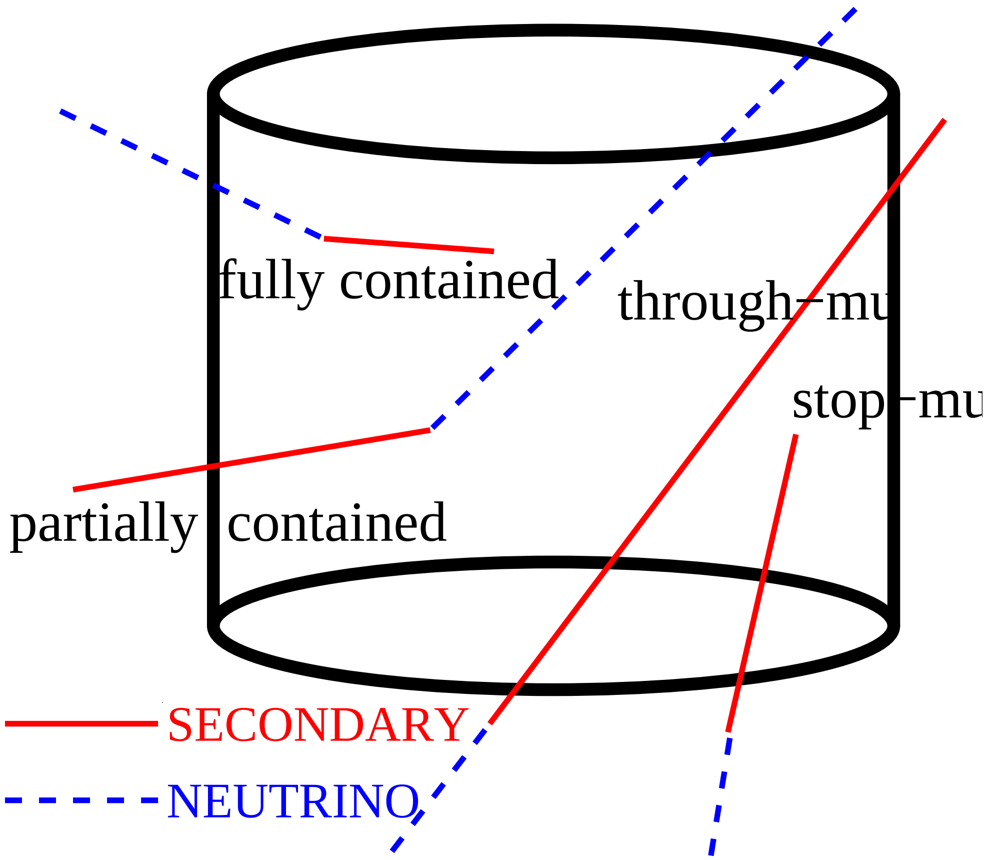

Figure 5.1: Super–Kamiokande event types.

large, so more than one interaction can occur in the detector during one spill.

For the analysis in this thesis, only FC events are used. The following describes how FC events are selected in SK and in the 1kt detector, and how they are reconstructed. Since the sources of background differ, the reductions are not the same; however, once a final sample of FC neutrino candidates is obtained, the same reconstruction algorithms are run on each [92].

5.1 SK Reduction

There are about 800,000 triggers per day in Super–Kamiokande which must be reduced by the atmospheric neutrino group down to the ten events per day due to atmospheric neutrinos. The data reduction process is done in five stages.

5.1.1 First Reduction

This is a collection of very simple cuts to quickly reduce the data to a manageable size. First, the maximum charge in a sliding time window 300 ns wide (PE_{300}) is measured. All events with $PE_{300} < 200$ *p.e.* are cut. The cut corresponds to a visible energy of $23 MeV$. Since the minimum analysis threshold is a visible energy of $100 MeV$, this cut is very safe. Next, events where the number of hits in the OD was greater than 50 in an 800 ns sliding time window are cut. This removes some cosmic ray muons without endangering FC events.

These two cuts reduced the event rate to 4,000 per day.

5.1.2 Second Reduction

Here, the OD cut is tightened to just 25 hits in the 800 ns window. In addition, a simple cut is introduced to get rid of some flashers. Sometimes a PMT flashes because of a problem with the dynode structure such that there is a spark. The PMT which sparks records a very large charge. PE_{300} is used again. If for any PMT the following is true:

$$\frac{PE_{single\ PMT}}{PE_{300}} \geq 0.5$$

the event is discarded.

After these cuts, there were about 500 events per day.

5.1.3 Third Reduction

With 500 events per day, the reduction algorithms become more sophisticated. The six cuts in this reduction level deal with the following background. There are still stopping and through-going cosmic ray muons as well as flashers and low energy events. Some of the cosmic ray muons enter through a dead area of the OD. The cables from the detector are collected in bundles and brought to the top of the detector through twelve cable holes. Four of these are in a position to block a portion of the OD. To compensate for this dead area, four $2 \times 2.5m$ plastic scintillation counters were placed over the bundles in April of 1997 and are used to veto some cosmic rays which pass through the OD undetected. In addition, there are accidental events where two or more unconnected interactions take place in a single event.

Since through-going muons are very energetic, they deposit a lot of charge in the ID. When they exit the ID, the area around the exit point is lit up like a Christmas tree. The ADC channels connected to these PMTs tend to saturate. Events where the charge on any single PMT in the event is larger than 230 p.e. and where the number of hit PMTs is greater than 1000 are passed to a special through-going muon fitter. The fitter selects an entrance and an exit point for the event. The entrance point is at the position of the earliest hit PMT with two more neighboring hit PMTs. The exit point was determined to be the center of the area of saturated PMTs. If more than 9 OD PMTs within $8m$ of the defined entrance or exit point were hit in a 800 ns window, the event was labeled a cosmic ray muon and cut.

A stopping muon fitter is applied to remaining events. It defines an entrance point in the same manner as above. If more than 9 OD PMTs satisfy the conditions described for the through-going muon fitter or if more than 4 OD PMTs satisfy those conditions and the goodness of fit is larger than 0.5, the event is classified as a stopping muon.

Events still surviving are passed to a low energy fitter which defines a sliding time window of 50 ns. If the maximum number of hit PMTs in the window is less than 50, the event is tossed.

Next, more complicated algorithms are applied to cut flashers. Events due to cosmic ray muons or neutrinos have a relatively sharp timing profile while many flashers have a profile which is very broad. By looking at an from the event trigger, take place for longer than a typical event. The number of hits in a 100 ns window which runs in an off-timing region from 300 to 900 ns away from the event trigger is recorded. If it is at least 15 hits for events with > 800 ID hits or at least 10 hits for events with ≤ 800 ID hits, the event is cut.

Remaining events are checked for accidental coincidence. If an event satisfies both of the following criteria, it is removed:

- at least 20 OD hits in the 500 ns time window from 400 to 900 ns after an event trigger.

- ID has more than 5000 p.e. in the same time window

Finally, events are checked to remove cosmic ray muons which passed through the cable bundles. If a cable hole veto counter fires and the track reconstructed by the through-going or stopping muon fitter passes within four meters of the hit veto counter, the event is discarded.

After the third reduction, only 30 events per day remain.

5.1.4 Fourth Reduction

When flashers are found, the high voltage on the PMT is turned off to prevent further contamination of the data. However, some flashers mimic the timing signature of neutrino events. While these can be removed by eye, there is one final algorithm applied to remove these events. Since flashing is an instrumental problem with a PMT, it is likely to repeat. PMTs in the same region of the detector will be hit with the same charge several times over the course of hours or days. Neutrino events, of course, are extremely unlikely to repeat in such a way. This algorithm searches for events with a similar pattern of charge distribution and marks them for disposal.

After this stage, we are left with about 20 events per day.

5.1.5 Scanning

The remaining events must be scanned by physicists to remove any remaining flashers or cosmic ray events. After minimum visible energy cut of $30MeV$ and a vertex cut requiring all vertices to be at least $2m$ from the wall, the background level in the FC sample is negligible.

5.2 1kt Reduction

Unlike SK, which has a separate reduction for FC and PC events, the 1kt makes the FC/PC separation after the reconstruction. The primary reason for this is there are no OD tubes on the downstream side of the detector. The 1kt reduction is much simpler than the SK reduction since we can look for events during the $1.2\mu s$ long beam spills. In the first stages of reduction, some very basic cuts are in place. First, only events which take place during the beam spill are selected. Next, only spills where there is no detector activity for at least $1.2\mu s$ before the spill are kept to prevent cosmic rays from occupying the electronics. Finally, events must have a minimum charge of 200 p.e.

5.2.1 Good Spills

As it is important to have a good understanding of the neutrino beam, spills are rejected if the quality of the beam is in doubt. Specifically, all of the the following criteria must be met for a spill to be called “good”:

- All beam-line components must be working properly
- The beam-line DAQ must be functioning

- The proton intensity must be greater than 1×10^{12} protons per pulse
- The current in both horns must be greater than 240 kA
- The 1kt must be alive
- SK must be alive

The final item is not important for this analysis, but is necessary for all long baseline neutrino studies. Since it results in very little loss of live-time, it is required for live-time consistency with the other analyses.

5.2.2 FADC

The analog sum of the PMTs is input into a flash ADC as described in Section 3.3. Each interaction makes a peak in the FADC data. If the peak contains more than 1000 p.e., it is considered a valid peak. This corresponds to about $100 MeV$ of visible energy. Events used for analysis must be from spills which have exactly one valid peak.

If a low energy event triggers the detector but subsequently there is a higher energy interaction, an event can be tagged as a one-peak event but actually contains two interactions. The TWIN cut requires the peak to coincide with the trigger time.

5.3 Reconstruction

The same reconstruction algorithms run on SK data are also run on 1kt data. Not only are both water Cherenkov detectors with the same instrumentation, but for studying long baseline neutrinos, having a near and far detector with similar detector and reconstruction systematic uncertainties is an advantage. Here is a description of each. A detailed description can be found in Ref. [94].

5.3.1 Vertex Fitting

The first stage of reconstruction is finding the event vertex. It is a three stage process. During all three stages, the assumption is all events are single-ring events. For multi-ring events, the practical outcome is the most energetic ring is usually fit. First, a rough vertex is found by minimizing the timing residuals of the PMTs assuming a point-like light emitter. The goodness, G_p, is maximized:

$$G_p = \frac{1}{N}\sum_i \exp(-\frac{t_i^2}{2\sigma^2})$$

where N is the number of hit PMTs, t_i is the time residual, and σ is the timing resolution. After finding a rough vertex, the direction is estimated by vector summing the charge-weighted directions from the vertex to each hit PMT.

Second, using the vertex and initial direction found above, a smoothed charge map is made as a function of the polar angle from the initial direction and the Cherenkov ring edge is found. By changing the direction slightly, this process is repeated to find the sharpest Cherenkov ring.

Finally, finite track lengths and scattered light are considered by redefining the goodness with portions corresponding to light inside and outside of the Cherenkov cone. Figure 5.2 shows the difference between the real and fitted vertices for single-ring and multi-ring events in SK. This is the final vertex for multi-ring events. Single-rings undergo one more fitting algorithm described in Section 5.3.4 which improves their vertex resolution.

Figures 5.3and 5.4 show vertex and directional resolutions for π^0 events in the 1kt detector.

5.3.2 Ring Finding

After the event vertex and first ring are established, the next task is to find any other Cherenkov rings in the event. In order to accomplish this task, we apply an algorithm which uses a Hough transformation [93]. The Hough transformation takes a ring finding problem and turns into a peak search. The basic idea is shown in Figure 5.5. In practice, we map the charge on all the PMTs onto a sphere with the vertex position at the center. Next, we remove from the map charge expected from the ring already found. We then search for peaks in this two dimensional space of polar and azimuthal coordinates $(\theta - \phi)$.

Once Cherenkov ring seeds are found, they are tested using a likelihood method. If a seed is found to be a valid ring, a new charge map is made and the process is repeated. This procedure is iterated until no seeds produce a valid ring.

5.3.3 Particle Identification

All particles are classified as showering, e-like, or non-showering, μ-like. Compared with showering events, non-showering events produce Cherenkov

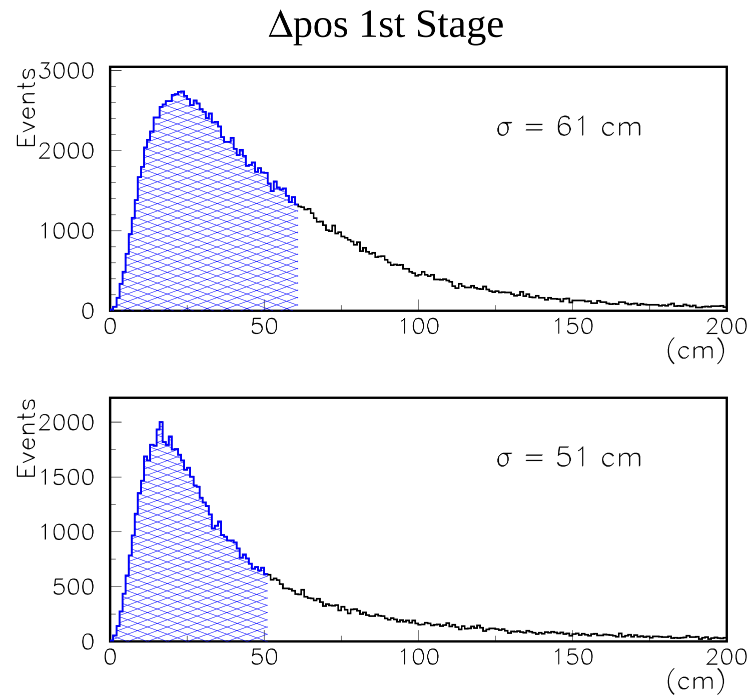

Figure 5.2: Super–Kamiokande Δ position distribution for the first stage fitter. The upper figure shows FC one-ring events. The lower figure shows FC multi-ring events.

rings with sharp edges as shown in Figure 5.6. In addition, when a muon loses energy, its β becomes less than 1 and the Cherenkov angle gets smaller. For electrons, this does not happen until they have very low energies. Our PID algorithms exploit these differences to categorize rings as e-like or μ-like.

Using a MC simulation of electrons and muons with perfect water transparency, a standard direct photon distribution is defined on an imaginary sphere for each particle type at several different energies. Next, using realistic water transparency, the amount of scattered light is estimated. Using the above, for any given vertex, direction and visible energy of a ring in the detector, an expected number of p.e.'s can be determined for each PMT for each particle type. An event is then compared with the standard distribution for e-like and μ-like events and a probability for each case defined.

Next, a probability using the opening angle is defined for each case. The

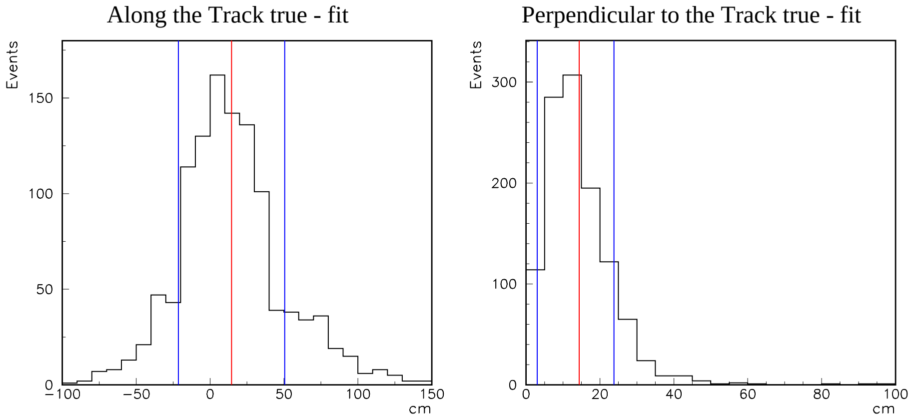

Figure 5.3: The fit - true vertex distribution for π^0 events in the 1kt. The left figure shows the distribution along the track while the right figure shows the distribution perpendicular to the track. The red line on each shows the mean deviation from the true vertex position, while the blue lines show the resolution around deviation.

pattern and opening angle probabilities are multiplied and an event is classified as e-like if $P_e > P_\mu$ and μ-like if $P_e < P_\mu$. Figure 6.11 shows the PID likelihood distributions for 1kt data.

5.3.4 MS Vertex Fitter

Since the first stage fitter uses only timing information, the resolution for single-ring events is not optimal. By using the expected light distribution for an event from the PID algorithm, the MS Vertex Fitter modifies the position of the vertex in the longitudinal direction. It then uses the same distribution to modify the direction of the event. After a new vertex and direction are found, the vertex is then moved perpendicularly to the particle direction using the first stage (timing based) fitter.

This process is iterated until the change in the vertex position is less than $5cm$, and the change in angle is less than 0.5 degrees. The vertex resolution becomes $34cm$ for e-like events and $25cm$ for μ-like events.

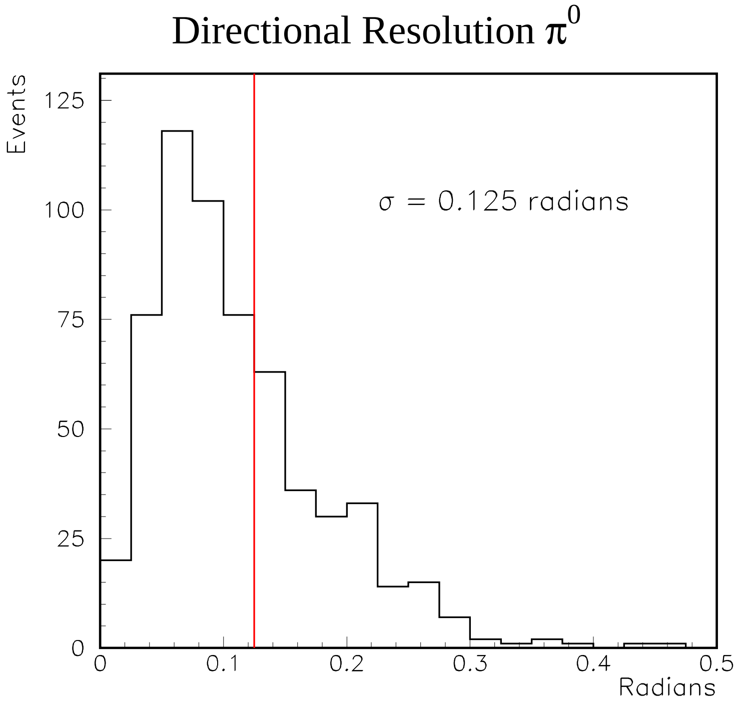

Figure 5.4: The angular deviation from the true direction in radians for π^0 events. The red line shows 1 σ deviation.

5.3.5 Momentum Reconstruction

The momentum of each ring is based on the total corrected charge associated with that ring in a cone defined by the ring direction with a half-angle of less than 70 degrees. The raw charge is selected in a 300 ns timing window and converted to corrected charge by taking into account the water transparency and the PMT acceptance.

5.3.6 FC Selection

The fiducial volume in SK is defined as the concentric cylinder $2m$ from the surface of the ID PMTs. FC events are selected during the reduction process.

In the 1kt, the fiducial volume for π^0 events is defined by a 4m diameter, 4m long cylinder ($\sim$ 50t) along the beam axis, while the fiducial volume for single-ring μ-like events is the upstream half of the 50t volume as shown in Figure 5.7.

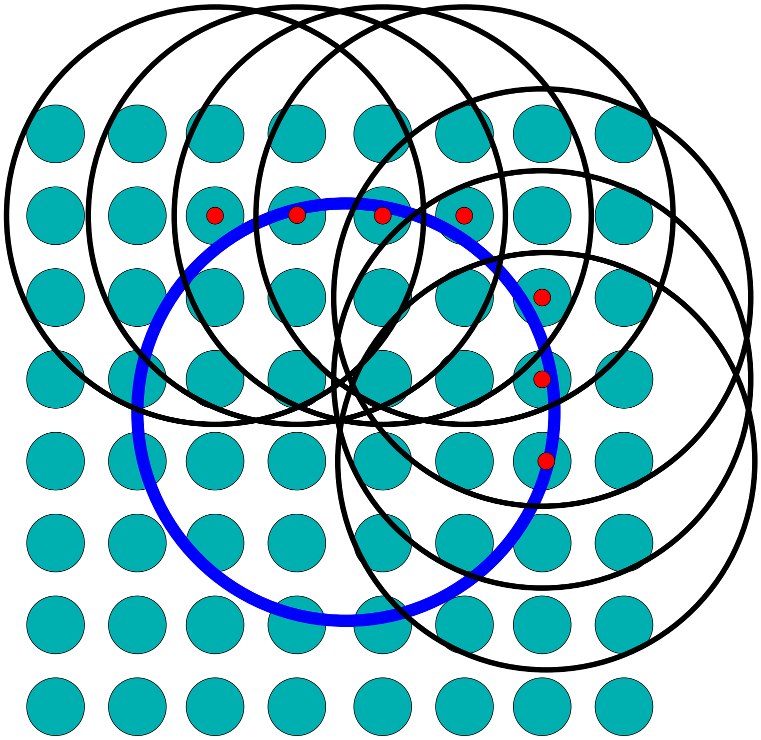

Figure 5.5: The cyan circles represent PMTs. The blue ring is a Cherenkov ring. Red circles denote some of the hit PMTs. By putting circles of a radius characteristic of the pattern expected from a Cherenkov ring emanating from the vertex centered on each hit PMT, we create a constructive interference at the center of the actual Cherenkov ring.

FC events are selected after the reconstruction is applied because the OD is not instrumented all the way around. To select FC events, we use a technique similar to the one used to identify the exit point of a through-going muon as described in Section 5.1.3. We look in a cone around the direction of each ring with a 20 degree opening angle to find the PMT with the most charge. The charge on that PMT is labeled $pomax20deg$. If $pomax20deg < 200 p.e.$, the event is classified as FC. The $pomax20deg$ distribution is shown in Figure 5.8.

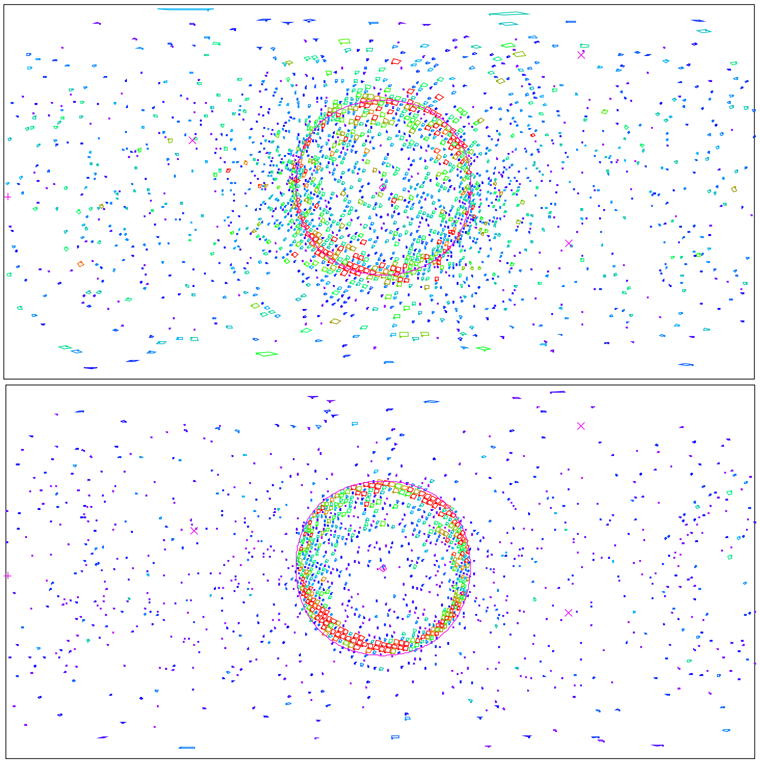

Figure 5.6: The figure on top shows a single electron, while the one on the bottom shows a single muon.

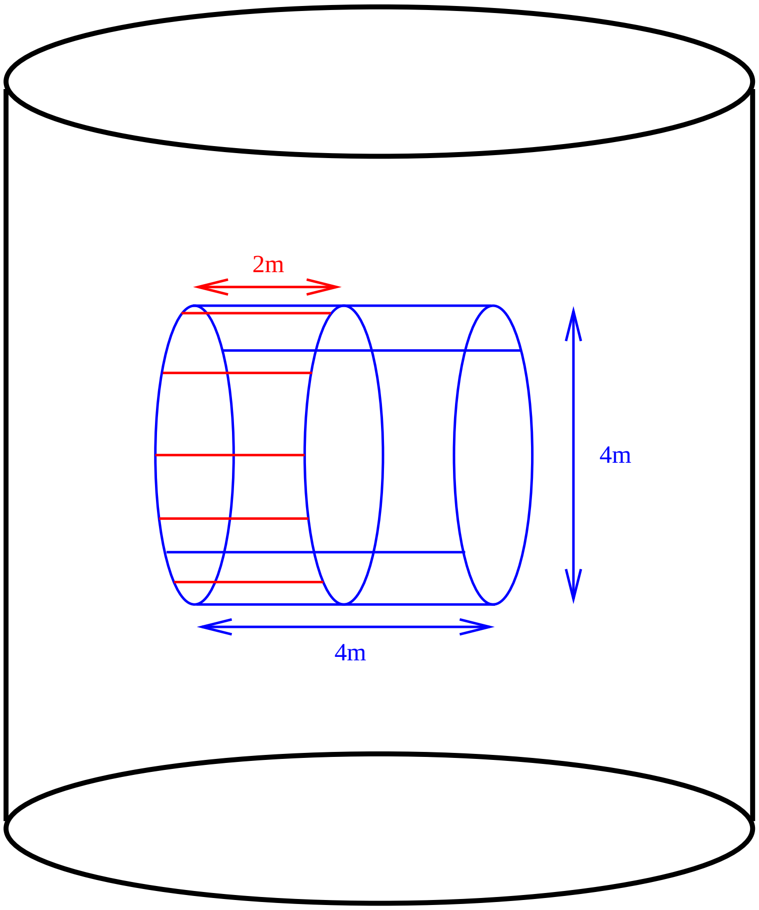

Figure 5.7: The 50 ton fiducial volume used for π^0 events is the $4m \times 4m$ cylinder shown in blue. The red lines denote the 25 ton fiducial volume used for FC muons.

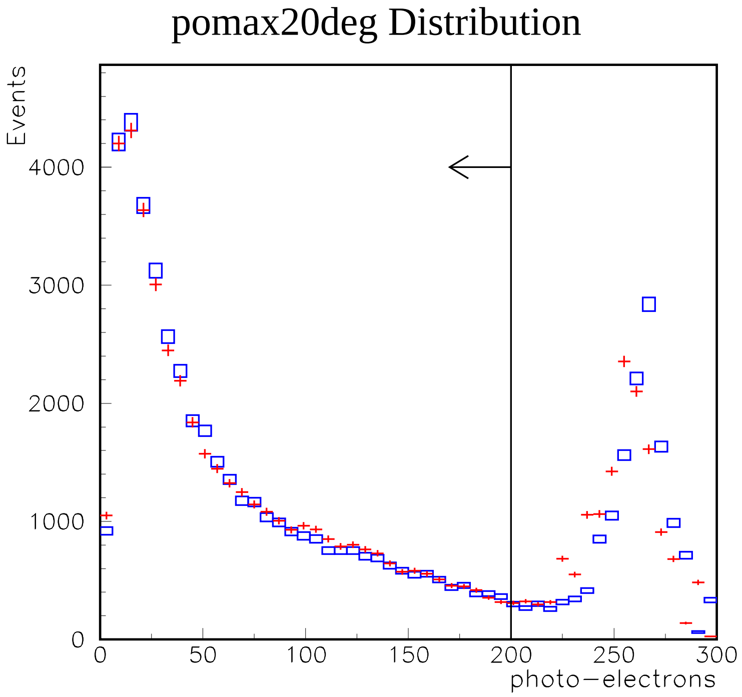

Figure 5.8: The *pomax20deg* distribution for all events passing the reduction in which the reconstruction successfully found a vertex.

Chapter 6

1kt π^0

The K2K beam gives us an unprecedented opportunity to make relative cross-section measurements in the $E_\nu \sim 1GeV$ regime. Back in Chapter 1, the quantity R_{π^0} was defined as follows:

$$R_{\pi^0} \equiv \frac{(\pi^0/\mu)_{data}}{(\pi^0/\mu)_{MC}}.$$

In Super–Kamiokande, R_{π^0} is useful to study $\nu_\mu \leftrightarrow \nu_\tau$ vs. $\nu_\mu \leftrightarrow \nu_s$ neutrino oscillation. In the context of Super–Kamiokande, it would be more natural to use electron-like events rather than muon-like events as the denominator because the ν_{e}'s are not participating in the oscillation. We use muon-like events because the K2K beam is almost pure ν_μ. This chapter explains the event selection, describes the systematic error analysis, and finally states the results of the measurement of R_{π^0} at the 1kt. Its use in the Super–Kamiokande analysis is described in Chapter 7.

6.1 π^0 Events

In large water Cherenkov detectors, π^0's are easy to find. With a lifetime of $8.4 \times 10^{-17}s$, they decay "instantaneously" as far as we are concerned. With a mass of 134.98 MeV/c^2, they are the lightest mesons and they decay electromagnetically to a pair of gamma rays 98.8 % of the time. Each gamma ray creates electromagnetic shower which makes a fuzzy ring. Our PID algorithms identify the rings as e-like. As such, our selection criteria are as follow:

- fully-contained
- event vertex is in the 50t fiducial volume

- two reconstructed rings
- both rings identified as showering (e-like)
- invariant mass is in the range 85 - 215 MeV/c^2

The result of the first four cuts is shown in Figure 6.1. A π^0 peak is clearly visible.

The data peak position (148.6 ± 0.3 MeV/c^2) is shifted relative to the MC peak (146.0 ± 0.4 MeV/c^2) position and both are shifted relative to the nominal π^0 mass. The data and MC relative shift is only two percent, well within our quoted systematic uncertainty in the energy scale of five percent. The shift from the nominal value is due to two reasons. First, when a π^0 is produced in oxygen in resonant production, a nucleon is usually ejected from the nucleus. The remaining nucleus is often left in an excited state and will then emit de-excitation gamma rays which add light (ie. energy) to an event. Second, there is a known reconstruction bias which causes higher momentum π^0's to be reconstructed with a systematically higher invariant mass. This happens as follows. During the reconstruction, once the first ring is found, the vertex remains fixed during the search for subsequent rings. Since the gamma rays do not convert in the water right after the decay, the vertex tends to be pulled into the event. This causes the reconstructed opening angle to be slightly larger than the true opening angle. While this is a very small effect, as the momentum of the π^0 increases, the opening angle becomes smaller because of the Lorentz boost. The relation for the π^0 invariant mass in a two-body decay to massless particles (gamma rays) is:

$$M_{inv} = \sqrt{2E_1E_2}\sqrt{1-\cos(\theta)}$$

where E_1 and E_2 are the energies of each gamma ray and $\cos(\theta)$ is the cosine of the opening angle. The important part is the $\sqrt{1-\cos(\theta)}$. For a given difference between the fitted and true $\cos(\theta)$, its relative importance increases as $\cos(\theta)$ approaches 1 because as $\sqrt{1-\cos(\theta)}$ approaches 0, its derivative becomes larger. Figure 6.2 shows there is no discernible change in the bias of

$$\cos(\theta_{reconstructed}) - \cos(\theta_{true})$$

as a function of momentum, but shows a large change in

$$\frac{\sqrt{1-\cos(\theta_{reconstructed})}}{\sqrt{1-\cos(\theta_{true})}}$$

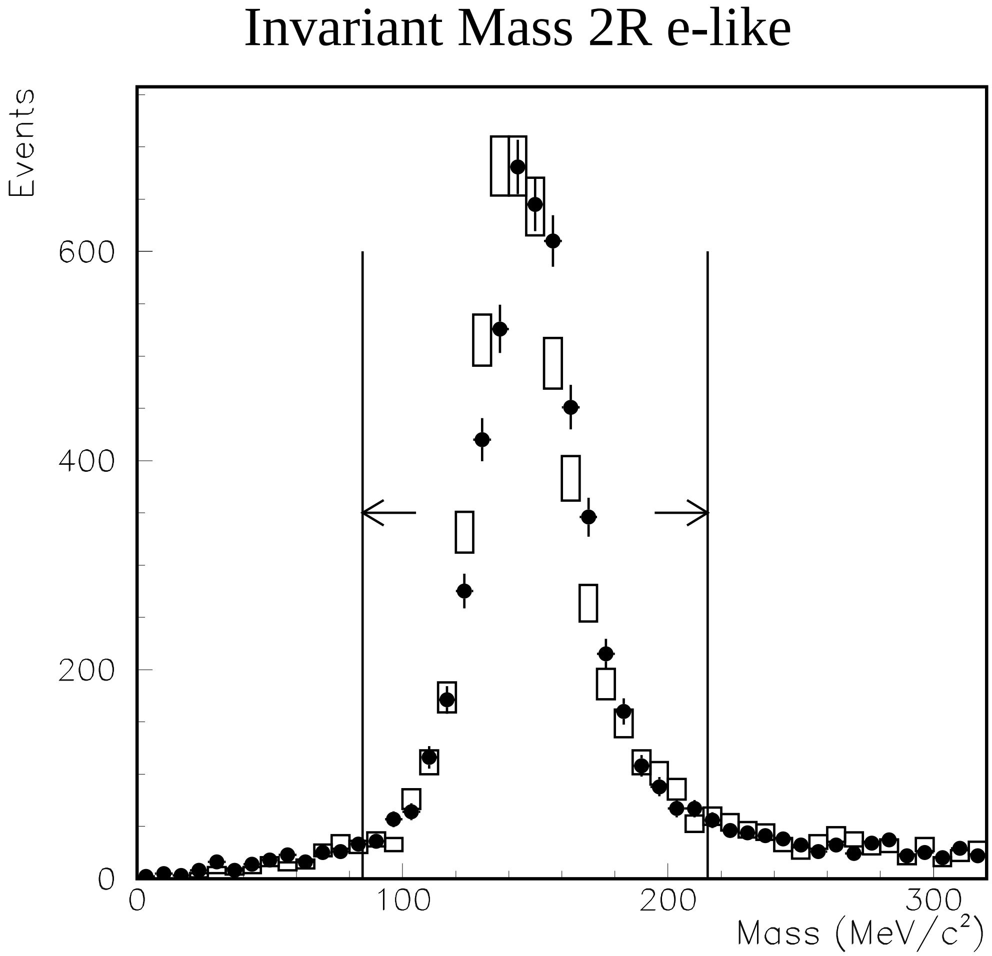

Figure 6.1: The invariant mass distributions of events with two e-like FC rings for data (black dots) and MC (boxes) in the 1kt detector. The arrows show the invariant mass cut. The MC is normalized to the data by entry.

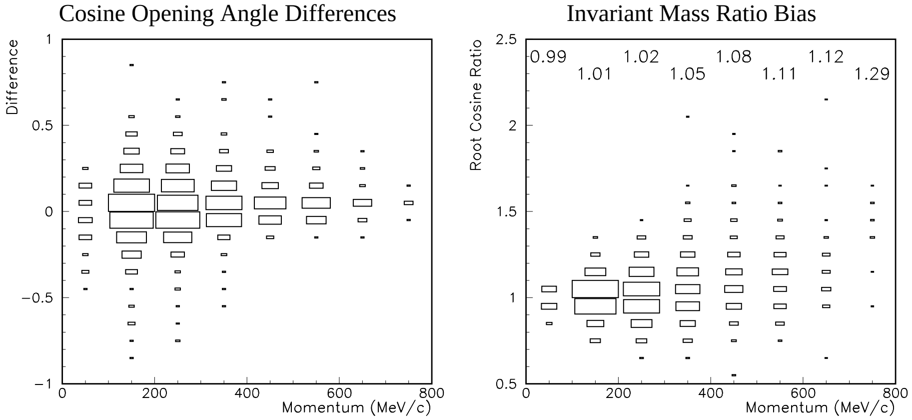

Figure 6.2: The figure on the left is the difference of the reconstructed and true opening angle of the gamma rays as a function of momentum. It shows no momentum dependence. The figure on the right is $\frac{\sqrt{1-\cos\left(\theta_{reconstructed}\right)}}{\sqrt{1-\cos\left(\theta_{true}\right)}}$ as a function of momentum. The mean values are also plotted and exhibit a momentum dependence.

as momentum increases. Accordingly, the reconstructed invariant mass increases as the π^0 momentum increases.

Figure 6.3 shows the efficiency to reconstruct a single π^0 in the fiducial volume as a function of momentum. The total efficiency is estimated to be about 47 %. The efficiency drops off as a function of momentum for two reasons. First, the asymmetry of the decays in the lab frame increases. Second, the opening angle between the two gamma rays decreases. Figure 6.4 shows the true opening angle of the gamma rays as a function of true π^0 momentum for events reconstructed and not reconstructed as π^0's. From Figure 6.4, we see smaller opening angle events are being preferentially reconstructed in the middle range of momenta. The smaller the opening angle, the more symmetric the decay. As the momentum increases, large opening angle decays have asymmetric momentum ratios and the reconstruction might miss the low energy second ring. For the highest momenta, however, the opening angle is so small the rings overlap and are mis-reconstructed as one ring.

Figure 6.5 shows the reconstructed momentum ratio and opening angle of π^0 candidates, and Figure 6.6 shows the reconstructed vertex distribution along the beam axis and perpendicular to the beam axis. Both figures demonstrate

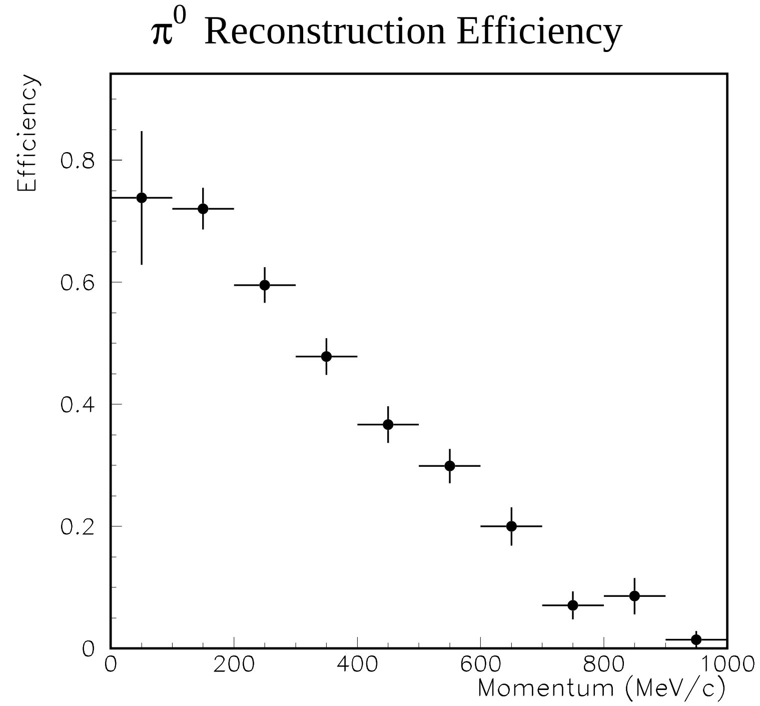

Figure 6.3: The efficiency to reconstruct a single π^0 in the fiducial volume as a function of momentum.

good agreement between data and MC.

Table 6.1 shows the fraction of the single π^0 sample due to each production mode. The π^0 sample has an NC fraction of 83%. The dominant contribution to the sample is from NC resonant single-pion production. In these interactions, either a π^0 is produced and escapes the nucleus, or a charged pion is produced and charge exchanges before leaving the nucleus. In NC coherent pion production, by definition the π^0 is produced as a free particle. In NC multi-pion reactions which contribute to the sample, an accompanying charged pion(s) is(are) either below Cherenkov threshold or absorbed in the nucleus. A small fraction of the sample comes from NC elastic interactions where the recoiling nucleon creates a π^0 in the water. The CC induced events are mostly resonant single-pion production with a muon below Cherenkov threshold or multi-pion production where the muon is below Cherenkov threshold and, as in the NC case, accompanying charged pions are absorbed in the nucleus or

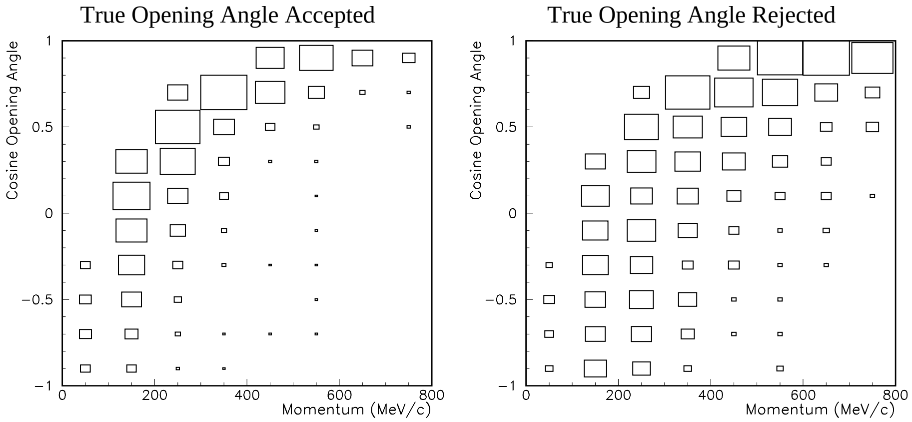

Figure 6.4: The figure on the left is the true opening angle of the gamma rays vs. the true momentum of the π^0 for events reconstructed as a π^0. The figure on the right is the same for events which were not reconstructed as a π^0.

below Cherenkov threshold. The left side of Figure 6.7 shows the invariant mass plot with production mode information. As the invariant mass increases, the contribution of "Others" - mostly CC events - becomes larger. The right side of the figure shows the invariant mass distribution with events with a π^0 in the final state shown in blue, and those without shown in green. Events accepted by the invariant mass cuts which do not have a π^0 in the final state are less than 0.5 % of the sample.

Figures 6.8 and 6.9 show that the MC reproduces the overall shape of the data angular and momentum distributions reasonably well. However, there are some differences and a close examination of the primary production modes

NC Coherent	14 %
NC Resonant	46 %
NC Multi-pion	19 %
NC Elastic	4 %
CC Resonant	8 %
CC Multi-pion	7 %

Table 6.1: The underlying interactions producing the π^0 sample.

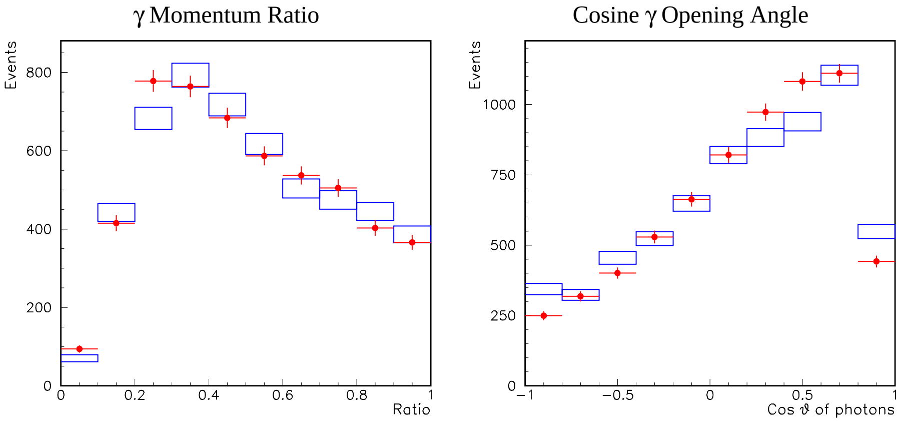

Figure 6.5: Momentum ratio and opening angle distribution of the gamma rays. The data are shown as red dots and the MC blue squares.

reveals simply changing the admixture of each mode (ie. changing the relative cross-sections) cannot account for the discrepancy between data and MC. The more likely cause is the uncertainty in the width of the Δ in oxygen. A different event generator, called NUANCE [95], with a different treatment of the Δ width and decay and final state interactions has been shown in earlier stages of this analysis to better reproduce the shapes of the momentum and angular distributions. However, the R_{π^0} measured with NUANCE is far from unity indicating a problem with the single pion to QE cross-section ratio. In addition, NUANCE has not been used to make a simulated FC atmospheric neutrino event sample at Super–Kamiokande and so a comparison of R_{π^0} between the 1kt and SK is not yet possible. Much discussion of the issues concerning neutrino event generators in the $E_\nu \sim 1GeV$ energy regime has taken place around the NuInt '01 Conference at KEK in Tsukuba, Japan [96]. The authors of both NEUT and NUANCE participated in the organization of the meeting and further conferences are planned. We look forward with great anticipation to this series of conferences and surrounding discussions to nail down the solution to this and other issues.

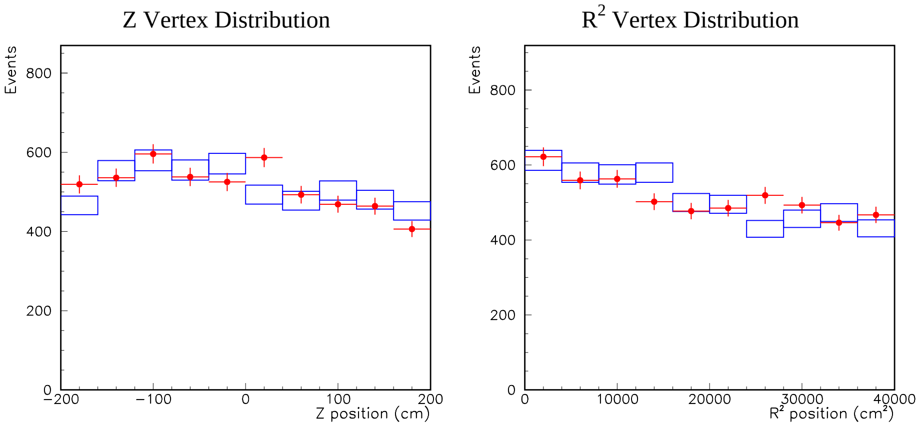

Figure 6.6: Distribution of π^0's in the fiducial volume. Data are red dots, MC is shown with blue squares.

6.2 FC Single Muons

As mentioned in Chapter 1, the first studies of atmospheric neutrinos focused on determining the ν_μ/ν_e flavor ratio. As such, the original Super–Kamiokande atmospheric neutrino reconstruction was designed specifically to find single ring events and classify them as e-like or μ-like.

The fiducial volume for the K2K 1kt FC muon sample is the upstream half (25t) of the fiducial volume used in the π^0 analysis [52]. The selection criteria for FC muons are:

- fully-contained
- single reconstructed ring
- ring is identified as non-showering (μ-like)

Figure 6.10 shows the FC muon momentum distribution. The data and MC agree well.

The FC muon sample has a charged current (CC) fraction of 97% , where 53% of the sample is due to QE scattering and 44% of the sample is due to CC pion production with the pions absorbed in the nucleus or below Cherenkov threshold. Three percent of the sample is due to NC interactions where a charged pion in the final state is above Cherenkov threshold. Energetic charged pions mimic muons with regard to PID.

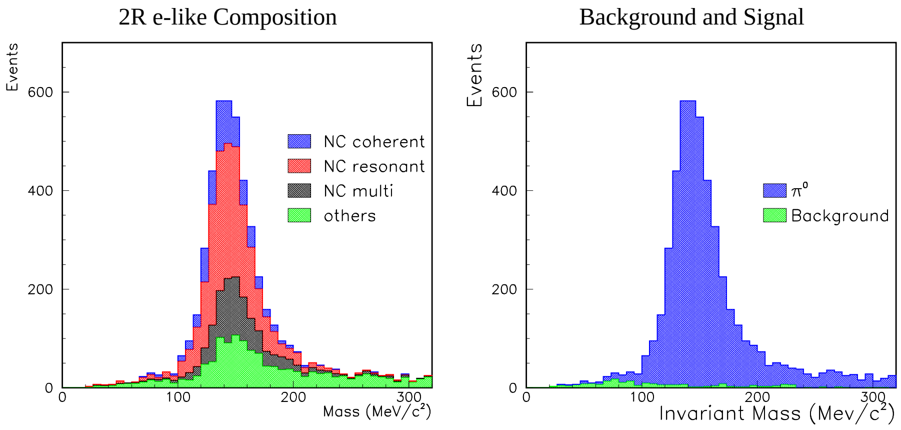

Figure 6.7: The figure on the left is the composition of the π^0 sample by production mode. “Others” is predominantly from CC-induced events. The figure on the right shows events with a π^0 in the final state in blue, and those without in green.

6.3 Systematic Uncertainties

We list the sources of systematic uncertainty we have identified on our measurement of R_{π^0} in Table 6.2.

Ring Counting	6 %
Particle ID	5 %
Fiducial Volume Cut	3 %
Flux	2 %
Energy Scale	1.5 %
FC Selection	1.5 %
MC Statistics	1 %

Table 6.2: The systematic uncertainty on R_{π^0} .

The systematic uncertainties on R_{π^0} due to the fiducial volume cut, the FC selection and the flux uncertainty were evaluated directly on the double ratio.

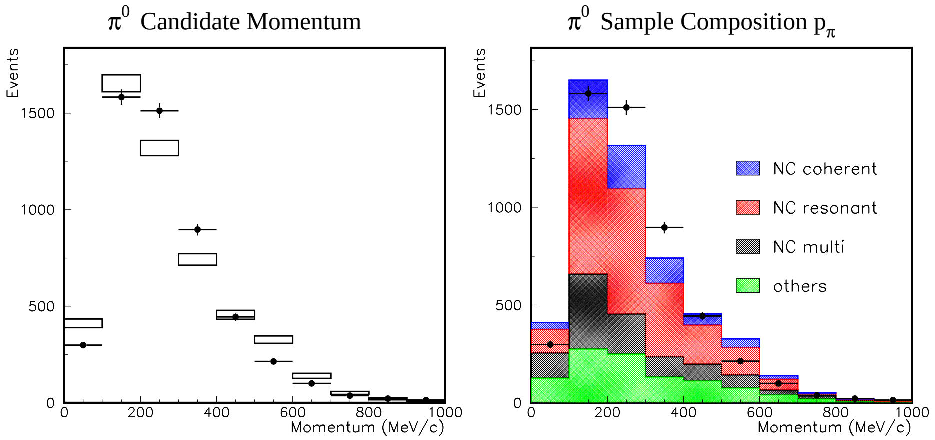

Figure 6.8: The momentum distribution of the π^0 data and MC samples where the MC is normalized by the data. On the left, the data are shown with the MC with statistical errors for both. On the right, the simulated data are shown by production mode. “Others” is predominantly CC single-pion production.

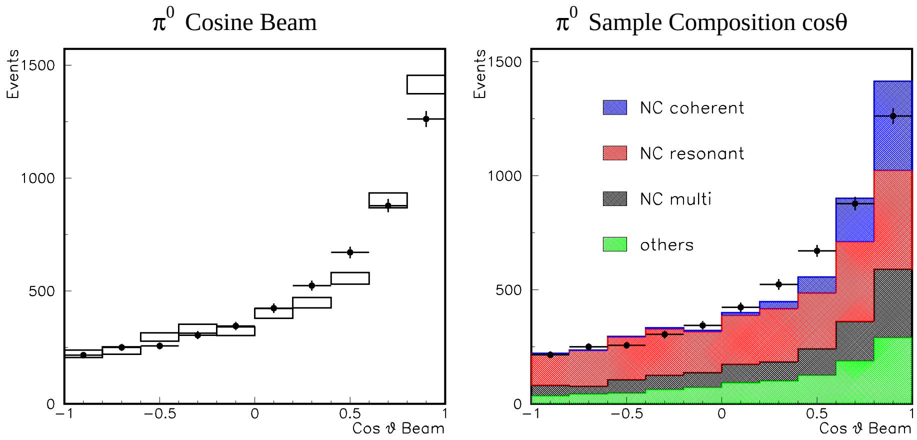

Figure 6.9: The angular ($cos\theta$) distribution with respect to the neutrino beam of the π^0 data and MC samples where the MC is normalized by the data. On the left, the data are shown with the MC with statistical errors for both. On the right, the MC is shown by production mode. “Others” is predominantly CC single-pion production.

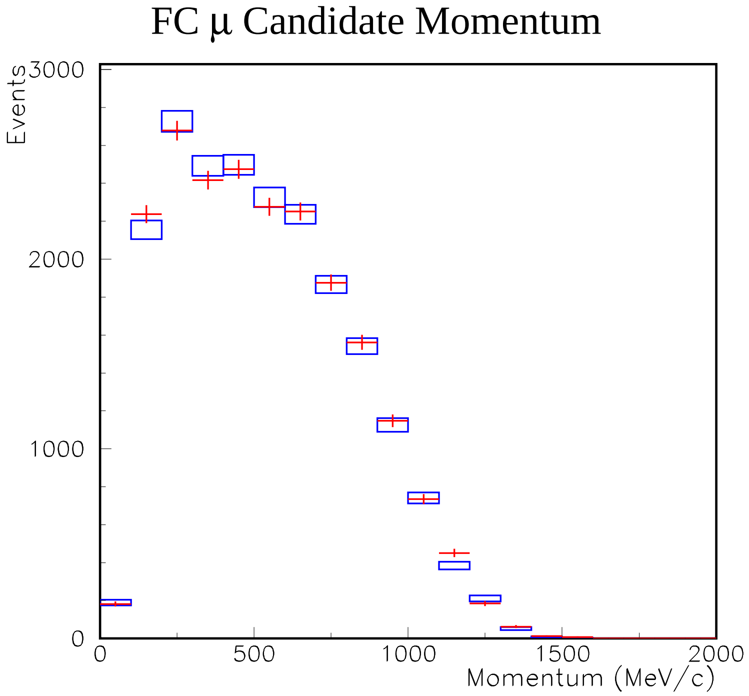

Figure 6.10: The FC muon momentum distribution. Red dots are data, blue squares are MC. The data and MC agree well.

- **Flux** The uncertainty was evaluated by independently varying the flux values in each neutrino energy bin of Figure 2.7 and determining the change in $(\pi^0/\mu)_{MC}$.
- **FC Selection** As described in Section 5.3.6, FC events are selected by cutting events where the PMT with the most charge has a charge above 200 p.e. Since the energy scale is uncertain to ±5%, the cut value was varied by ±5% and the change in R_{π^0} evaluated.
- **Fiducial Volume Cut** The fiducial volume was shifted by $\pm 37cm$, the fitting resolution for π^0's, perpendicular to the beam axis (vertically) and along the beam axis and the maximum change in R_{π^0} was defined as the systematic uncertainty.

The uncertainty on R_{π^0} due to the energy scale uncertainty was evaluated on each sample separately. After scaling the energy by ±5%, the number of events in each class was calculated and the effect on R_{π^0} determined. The effect on FC muons was negligible; however, because of the invariant mass cut, the number of π^0's changed by 1.5%.

The dominant sources of systematic uncertainty on R_{π^0} are ring counting and particle identification (PID). Both were evaluated for the π^0 and FC muon samples separately and then combined on the double ratio assuming no correlations. The ring counting and PID uncertainties on R_{π^0} are almost entirely due to the systematic uncertainties from the π^0 reconstruction. For the π^0 sample, the PID and ring counting systematic errors are both 5 %, while for the FC muon sample, they are 1 % and 4 % respectively. All four are described in more detail below.

6.3.1 Particle ID FC μ

The PID likelihood distribution is shown in Figure 6.11 for FC single-ring events. Events on the positive side of the PID parameter scale are classified as μ-like, while those with a negative PID parameter are classified as e-like. The peak positions on the PID parameter scale differ by about 0.25 between data and MC. To define a systematic error, we change the cut by 0.50 in each direction and measure the change in the total number of μ-like events. For both data and MC, in either direction, all changes are below one percent. We then define the systematic error on the number of FC muons due to PID to be 1 %.

6.3.2 Particle ID π^0

Particle ID for multi-ring events is more difficult because with more rings, there are more opportunities for failure and also because assigning charge to a particular ring for overlapped rings is a difficult business. Initially the systematic uncertainty was evaluated in a similar fashion to FC muons (instead of a cut line, there was a two-dimensional cut region). Subsequently a different method was found which has allowed us to reduce the systematic error for the π^0 sample due to PID from six percent to five percent.

If all rings are assumed to be e-like for purposes of momentum reconstruction and no PID cut is made on the data, from all two ring events in the 1kt event sample, a plot of invariant mass still reveals a large π^0 peak. The right side of Figure 6.12 shows this distribution. The left side of the figure shows the distribution with PID cuts in place. We compare the ratio of the number of π^0 events with PID cuts to the number of π^0 without PID cuts for data and MC and define this as the systematic uncertainty due to the PID cuts on the

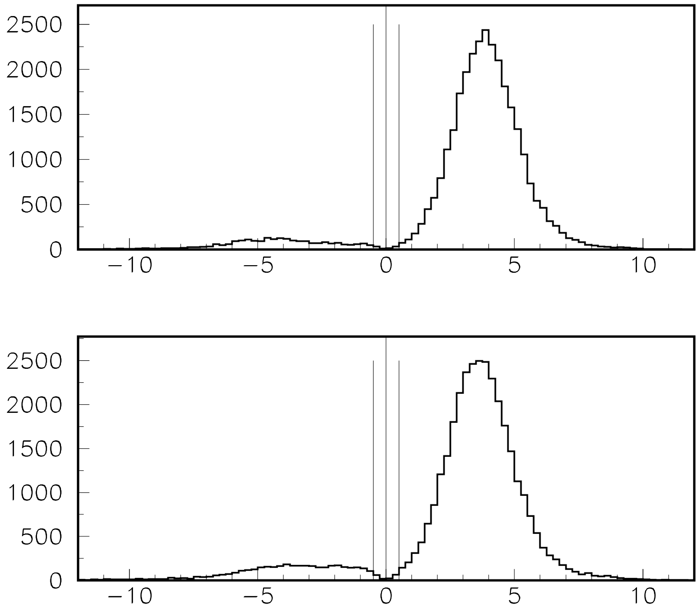

Figure 6.11: The PID likelihood distributions for MC (above) and data (below). Muon-like events are positive, electron-like events are negative. The middle line on each plot shows the nominal cut value. The lines to either side show alternative cuts used to define a systematic error. The total number of FC single-ring muons changes by less than one percent for each case.

π^0 sample. We define the efficiency:

$$\epsilon = \frac{N^{\pi^0}_{PID}}{N^{\pi^0}_{No\ PID}}$$

and the systematic error on the efficiency:

$$\delta_\epsilon = \frac{|\epsilon_{data} - \epsilon_{MC}|}{\epsilon_{MC}}$$

Instead of counting events within invariant mass cut values, we fit the peak and the background and integrate the fit function for the peak. To account

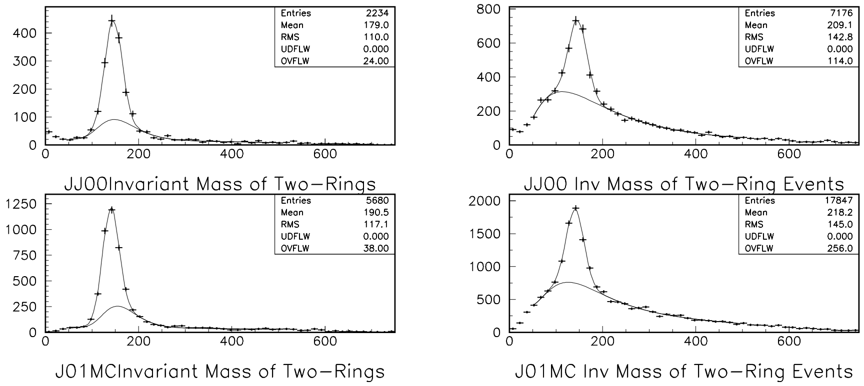

Figure 6.12: The invariant mass distributions for standard cuts on the left, and no-PID cut on the right. The upper figures are for data, while the lower figures are for MC. The continuous lines show the fits for the background and background plus signal.

for possible differences in the MC cross-sections with reality, we create several MC distributions with cross-sections re-weighted according to their systematic uncertainties. We define the PID systematic uncertainty using the largest difference of δ, which was 5 %.

6.3.3 Ring Counting FC μ

To simulate a systematic difference between data and MC which would confuse the ring counting algorithm, we chose to add more light scattering to events. Muons were generated at $100MeV$ intervals from $100MeV$ to $1.2GeV$. Since Cherenkov radiation and photon propagation have large variations event to event, generating a statistically relevant sample of events at each energy is very difficult. Instead, with an existing set of events for a given energy, we developed software to operate on the existing distribution of tube hits with a scattering model and rewrite the event. Each set of data was then run through the reconstruction algorithms and the efficiencies compared. We define our systematic uncertainty on the efficiency due to ring counting for muons to be largest measured change in efficiency for the above event samples. This was for $E_\mu = 600MeV$ and the efficiency change was 4 %.

6.3.4 Ring Counting π^0

At first, the method described for FC muons was used for π^0's as well and yielded an estimate of 6 %. However, this has since been partially replaced by a new method inspired by the example of PID for π^0's. During ring counting, sometimes, a ring will be split into two, such that an event with a single π^0 which decays to two gamma rays will be classified as a three-ring event. Usually the energy is shared among the rings in such a way that if one reconstructs the invariant mass of the event, it is near the π^0 mass. The right side of Figure 6.13 shows the invariant mass distribution of three-ring e-like events and a π^0 mass peak is clearly visible. By carrying out a similar procedure described for the PID systematic uncertainty estimate, we define a δ_ϵ for ring counting. In the case of the PID systematic uncertainty estimate, the no-PID sample contained the PID sample. In this case, however, the samples are exclusive, so the definition is:

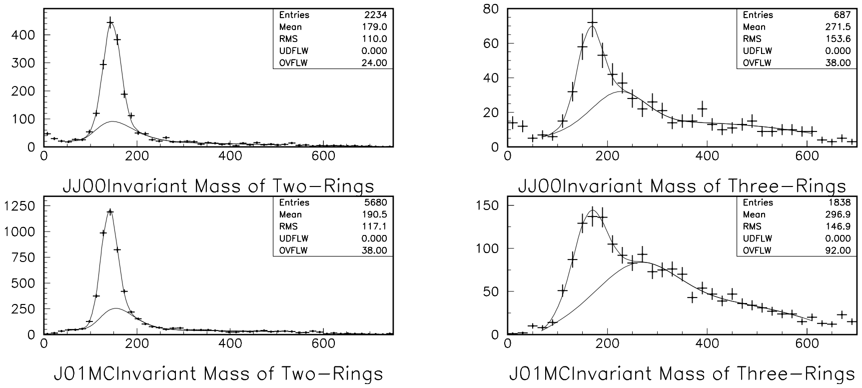

Figure 6.13: The invariant mass distributions for standard cuts on the left, and three-ring e-like events on the right. The upper figures are for data, while the lower figures are for MC. The continuous lines show the fits for the background and background plus signal.

$$\epsilon = \frac{N_{2R}^{\pi^0}}{N_{2R}^{\pi^0} + N_{3R}^{\pi^0}}.$$

After accounting for cross-section uncertainties, the largest difference is 1 %. While this is exciting news, uncertainty is only good for the 2 ↔ 3 case. The 1 ↔ 2 case is not covered by this estimate. Since we cannot reconstruct an invariant mass for one-ring events, we define the 1 ↔ 2 systematic uncertainty as the old value of 6 %. We then define the systematic uncertainty on the efficiency for the π^0 sample due to ring counting as the average of the two weighted by the number of events. Since the number of one-ring e-like events is much larger than the number of three-ring π^0-like events, the result is 5 %.

6.4 Results

The data described in this chapter were taken from January to March, 2000, and from January to July 2001 and correspond to 3.21×10^{19} protons on target, yielding 5,133 π^0 events and 20,555 FC single-ring muons.

From the real and simulated data, we obtain:

$$R_{\pi^0} = 1.00 \pm 0.02(stat.) \pm 0.09(sys.).$$

Chapter 7

Super–Kamiokande π^0 Analysis

Single-π^0 production from atmospheric neutrinos is a clean NC signal in Super–Kamiokande. As mentioned in Chapter 1, if the solution to the atmospheric neutrino oscillation problem is $\nu_\mu \leftrightarrow \nu_s$ oscillation, we expect measurements to be lower than the expectation for the no-oscillation case. If the solution is $\nu_\mu \leftrightarrow \nu_\tau$ oscillation, the expected NC rate would be roughly the same as the no-oscillation case. This chapter describes the atmospheric neutrino R_{π^0} oscillation analysis and the use of the 1kt R_{π^0} measurement in this analysis. The data analyzed for this analysis correspond to 1289 live-days.

7.1 π^0 Events

The selection criteria for π^0 events at SK are almost the same as the criteria used in the 1kt and are as follows:

- fully-contained in the 22.5 kton fiducial volume
- two reconstructed rings
- both rings identified as showering (e-like)
- no observed decay electron
- invariant mass is in the range 85 - 185 MeV/c^2

Super–Kamiokande has the capability to observe decay electrons. The fourth criterion allows us to reject many events where there is a muon or charged pion present in the final state, but below Cherenkov threshold. The invariant mass distribution of events passing the first four criteria for π^0's is shown in Fig. 7.1. Between the invariant mass cut values are 414 events.

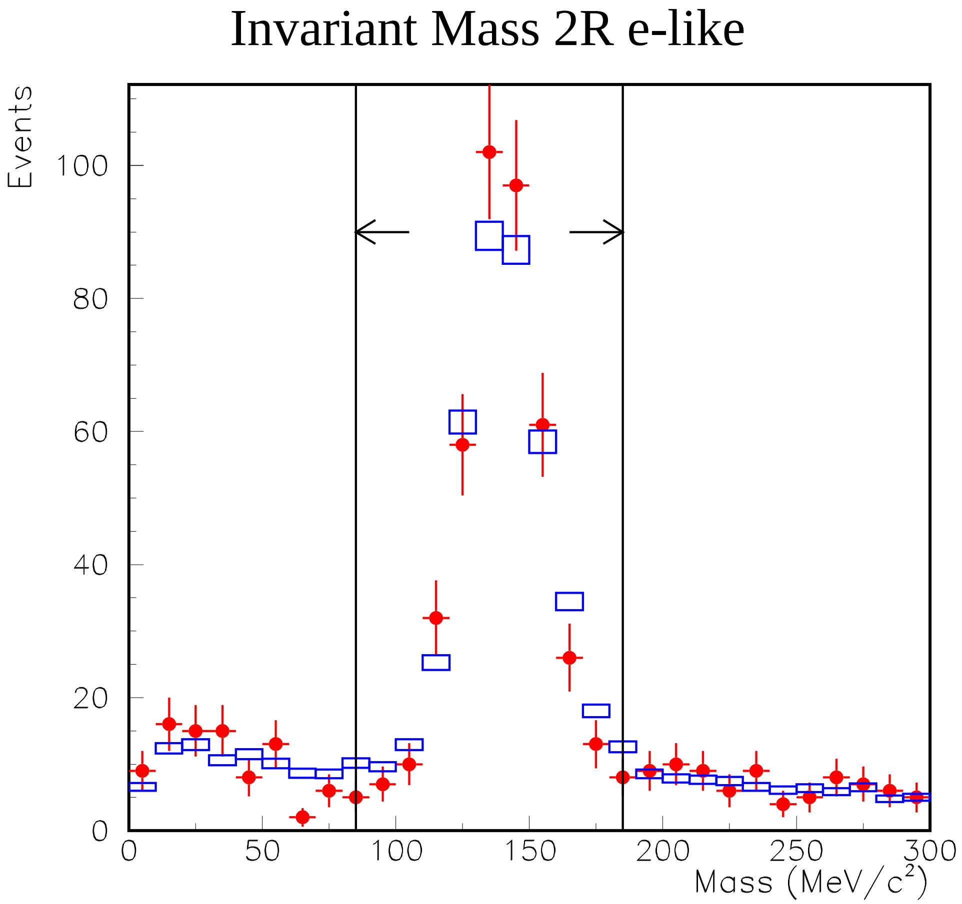

Figure 7.1: The invariant mass distributions of events with two e-like FC rings for data (red dots) and MC (boxes) in Super–Kamiokande. The arrows show the invariant mass cut. The MC is normalized to the live-time of the data.

NC Coherent	21 %
NC Resonant	48 %
NC Multi-pion	14 %
NC Elastic	2 %
NC other	1 %
CC Resonant	8 %
CC QE ν_e	4 %
CC Multi-pion	2 %

Table 7.1: The underlying interactions producing the π^0 sample.

For no oscillations, we estimate 86% of the π^0 sample is from NC interactions. The breakdown of interaction modes is shown in Table 7.1. As in the 1kt, the multi-pion channels contribute because charged pions are either below Cherenkov threshold or are absorbed in the nucleus. The CC pion productions modes also contribute when the charged particles are below Cherenkov threshold. In addition, when more than one ring is identified, either due to misreconstruction or a hard scatter, QE ν_e events contribute to the sample.

Figure 7.2 shows the π^0 momentum distribution. While there is very good agreement between data and MC, with only 414 π^0 events, the SK sample is significantly smaller than the 1kt sample.

7.2 FC Single Muons

The selection criteria for FC muons in Super–Kamiokande are quite similar to those used in the 1kt analysis:

- fully-contained in the 22.5 kt fiducial volume
- single reconstructed ring
- ring is identified as non-showering (μ-like)
- muon momentum $> 200\ MeV$.

We recorded 3346 single-ring muon events. According to the simulation, 96 % of the muon sample is from CC ν_μ interactions. The production modes are listed on Table 7.2

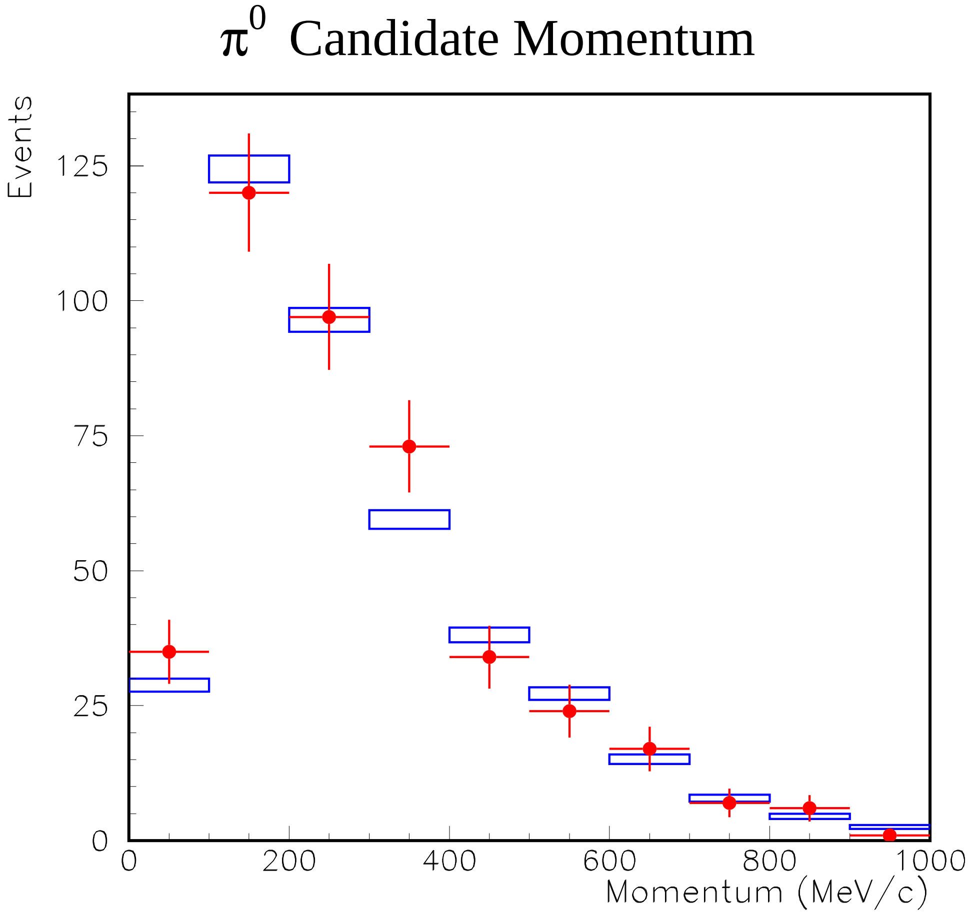

Figure 7.2: The π^0 momentum distribution in Super–Kamiokande. The data are shown in red dots and the MC in blue boxes. The MC is normalized to the live-time of the data.

CC QE	68 %
CC Resonant	20 %
CC Multi-pion	6 %
CC Coherent	2 %
NC Resonant	3 %
NC Multi-pion	1 %

Table 7.2: The underlying interactions producing the FC muon sample.

7.3 Systematic Uncertainty on R_{π^0}

Before attempting to use the 1kt measurement to reduce the systematic error on $R_{\pi^0}^{SK}$, let us discuss the systematic error without the 1kt. The values are shown in Table 7.3.

Reconstruction	7 %
Atmospheric Neutrino Flux	2 %
MC Statistics	1 %
Cross Section	22 %
Nuclear Reinteractions	7 %
Total	24 %

Table 7.3: The systematic error on $R_{\pi^0}^{SK}$ before using the 1kt measurement.

The reconstruction systematic uncertainty was derived differently in SK than it was in the 1kt. With the benefit of a lot of manpower, events could be hand-fit and compared with the vertices, rings, and PID assignments by computer. As discussed in Chapter 2, the ratios:

$$\frac{\nu_\mu + \bar{\nu_\mu}}{\nu_e + \bar{\nu_e}} \;,\; \frac{\nu}{\bar{\nu}}$$

are only known to 5 % and 10 % respectively. The former has little effect on the π^0 sample, but a larger effect on the number of FC muons. The effect on R_{π^0} is $\sim 2\%$. The latter affects both samples and results in a $\sim 0.5\%$ on R_{π^0} . The two combined are about 2 %. The largest systematic uncertainty on R_{π^0} is due to π^0 cross sections and nuclear re-interaction uncertainties in the MC. Before the 1kt measurement, this combined error was 23% making an assessment of the $\nu_\mu \leftrightarrow \nu_\tau$ vs. $\nu_\mu \leftrightarrow \nu_s$ issue with π^0's impossible. The cross-section uncertainties are due to uncertainties on the cross-section of each production mode and due to a 20 % uncertainty on the NC/CC ratio. The second column

Production Mode	Uncertainty	Error on R_{π^0}
Quasi-elastic	10 %	6.0 %
Resonant 1π	40 %	15.6 %
Coherent π	50 %	13.0 %
Multi-pion	40 %	5.5 %

Table 7.4: The cross-section uncertainties and their effect on $R_{\pi^0}^{SK}$.

of Table 7.4 shows the nominal uncertainties for each production mode. The error on R_{π^0} was calculated for each production mode by varying the cross-section by the nominal uncertainty and simultaneously varying the NC/CC ratio by 20 %. The resultant effect on R_{π^0} is shown in the third column of Table 7.4. The uncertainty on re-interactions was estimated by changing the π^0 mean path length in oxygen by 50 %, resulting in a change of R_{π^0} of 7 % [33].

7.4 Using the 1kt Measurement in SK

The first step to use the 1kt measurement is to figure out what exactly we are measuring. In SK, the uncertainties listed on Table 7.3 from the cross-section and from nuclear re-interactions were evaluated on the double ratio R_{π^0} . The cross-section uncertainties for single-pion production are large, so the error on the ratio is mostly from the π^0 sample. However, it is important to note about a third of the selected FC single-ring muons are from interactions where a pion was produced in the nucleus (or a Δ which was allowed to undergo pionless decay). These pions are either absorbed, or they are charged pions which go undetected in the water. The R_{π^0} measurement at the 1kt tests the combined effect of of the cross-section and nuclear re-interaction uncertainties. These uncertainties together total 23 % on $R_{\pi^0}^{SK}$.

The two major differences which prevent our complete replacement of 23 % with the 9 % 1kt measurement uncertainty are differences in neutrino energy spectra, and different neutrino compositions of each beam. The K2K beam is almost pure ν_μ, while the atmospheric neutrino beam contains ν_e's and muon

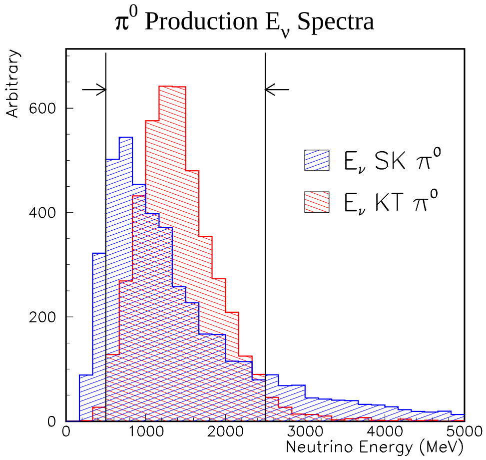

Figure 7.3: Energy spectrum of neutrinos producing the π^0 samples at SK and K2K. Most of the π^0 sample at K2K comes from neutrinos between 500 and 2500 MeV. The π^0 sample at Super–Kamiokande has a low energy shoulder and a high energy tail from which 20% of the sample originates. The arrows show the region of neutrino energies where the 1kt result is applied. Details are in the text.

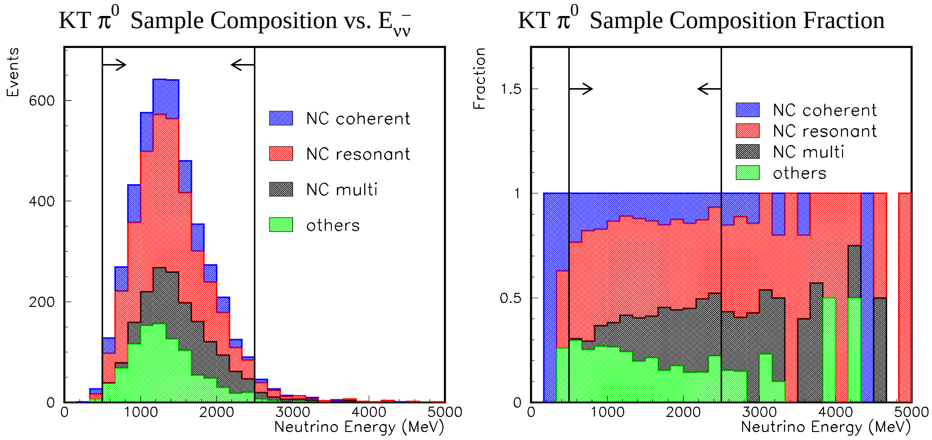

Figure 7.4: The KT composition as a function of neutrino energy. The left figure shows the energy spectrum while the right figure shows the fraction. “Others” is predominantly CC single-pion production. The arrows show the region of neutrino energies where the 1kt result is applied. Details are in the text.

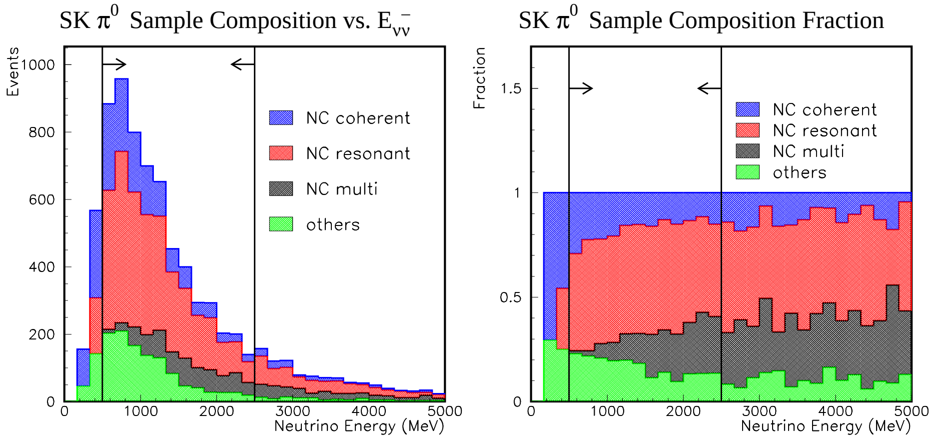

Figure 7.5: The SK composition as a function of neutrino energy. The left figure shows the energy spectrum while the right figure shows the fraction. “Others” is predominantly CC single-pion production. The arrows show the region of neutrino energies where the 1kt result is applied. Details are in the text.

and electron anti-neutrinos. Figures 2.2 and 2.7 show the atmospheric and K2K beam fluxes respectively. While there is similarity in the $1 \sim 2GeV$ energy region, there is a higher relative low-energy neutrino flux for atmospheric neutrinos than for K2K beam neutrinos. Even more pronounced is the high-energy tail in the atmospheric neutrino energy spectrum, while the K2K beam cuts off above a few GeV.

Fig. 7.3 shows the parent neutrino energy distributions for the π^0 samples selected from K2K beam interactions in the 1kt and from atmospheric neutrino interactions in Super–Kamiokande. While the spectrum of atmospheric neutrinos which produce π^0's is very wide, as expected, the spectrum of beam neutrinos which produce π^0's is mostly constrained within $500\ MeV \leq E_\nu \leq 2500\ MeV$. Therefore, the measurement of the 1kt only tests the accuracy of the MC prediction of $R^{SK}_{\pi^0}$ between these energies.

We estimate the uncertainty on the MC prediction by using the value calculated in Section 7.3, 23 %, for neutrinos of energies outside the above range and using the uncertainty on the 1kt measurement for neutrinos between 500 and 2500 MeV. The 1kt measurement uncertainty on $R^{K2K}_{\pi^0}$ is 9%, but as is clear from Fig. 7.3, even for energies between 500 and 2500 MeV, the spectra have slightly different shapes.

Figures 7.4 and 7.5 show the composition of the π^0 samples for the 1kt and SK as a function of neutrino energy. The SK distributions show the results for neutrinos + anti-neutrinos. We estimate the systematic uncertainty of using the 1kt measurement uncertainty in this energy range by allowing the cross-sections to float within the uncertainties stated in Table 7.3 and such that $R^{1kt}_{\pi^0}$ must remain equal to the measured value. With the different allowed admixtures, the effect on $R^{SK}_{\pi^0}$ is calculated. The maximum difference was 3.5%. Added in quadrature with the 1kt reconstruction systematic uncertainty, the total uncertainty on the MC prediction of $R^{SK}_{\pi^0}$ from neutrinos between 500 and 2500 MeV is 10%. The flux weighted uncertainty is 13%. The revised systematic uncertainty on $R^{SK}_{\pi^0}$ is shown in Table 7.5.

7.5 Analysis: $\nu_\mu \leftrightarrow \nu_\tau$ vs. $\nu_\mu \leftrightarrow \nu_s$ Discrimination

From the real and simulated data for no oscillations, we obtain:

$$R_{\pi^0} = 1.49 \pm 0.08(stat.) \pm 0.21(sys.)$$

To test $\nu_\mu \leftrightarrow \nu_\tau$ and $\nu_\mu \leftrightarrow \nu_s$, we calculate $(\pi^0/\mu)_{MC}$ for both oscillation

Reconstruction	7 %
Atmospheric ν flux	2 %
MC Statistics	1 %
K2K $\leftrightarrow$ SK flux difference	3.5 %
$500 < E_\nu$(MeV) < 2500	9 %
$E_\nu < 500$ MeV $E_\nu > 2500$ MeV	23 %
Flux averaged	13 %
Total	15 %

Table 7.5: The systematic error on $R^{SK}_{\pi^0}$ after using the 1kt measurement.

hypotheses as a function of Δm^2 (assuming $\sin^2 2\theta = 1.0$) and compare these predictions with $(\pi^0/\mu)_{data}$, as shown in Fig. 7.6. At Super–Kamiokande 's best fit point, of $\sin^2 2\theta = 1.0$ and $\Delta m^2 = 2.5 \times 10^{-3}$, $\nu_\mu \leftrightarrow \nu_\tau$ oscillation implies $R_{\pi^0} = 1.41$, in agreement with the measured value of 1.49 ± 0.22, while the $\nu_\mu \leftrightarrow \nu_s$ oscillation hypothesis predicts $R_{\pi^0} = 1.17$. The result using the systematic uncertainties from Table 7.3, that is, without using the 1kt measurement is shown in Figure 7.7.

While we cannot say definitively by this study the $\nu_\mu \leftrightarrow \nu_\tau$ hypothesis is correct, by using the 1kt measurement, we can say our result is more consistent with the $\nu_\mu \leftrightarrow \nu_\tau$ hypothesis. Furthermore, since this result does not depend on matter effects, it is an important check of the SK analysis using predominantly high-energy muons [32].

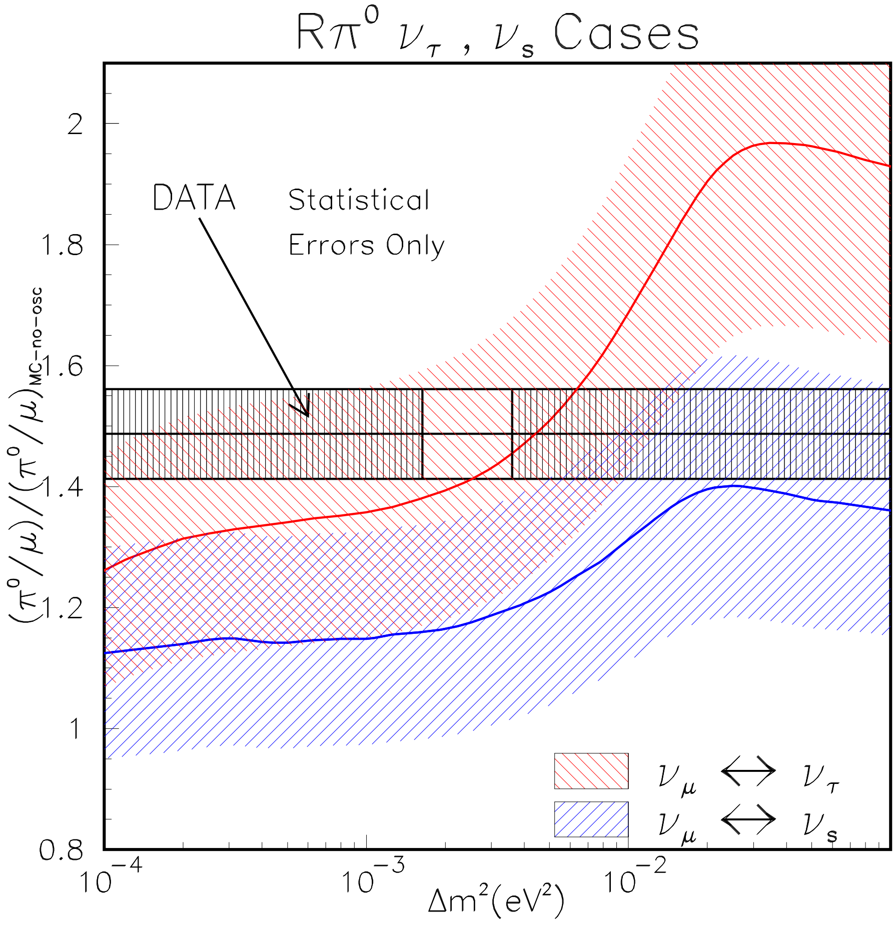

Figure 7.6: For maximal mixing, these are the predictions of R_{π^0} for $\nu_\mu \leftrightarrow \nu_\tau$ and $\nu_\mu \leftrightarrow \nu_s$. The R_{π^0} for data is shown with statistical errors only. All of the systematic error is shown on the predictions. The error bars are 1 σ. The empty box on the bar corresponding to the data R_{π^0} is the Super–Kamiokande 95 % confidence limit from the single-ring sample [97, 92].

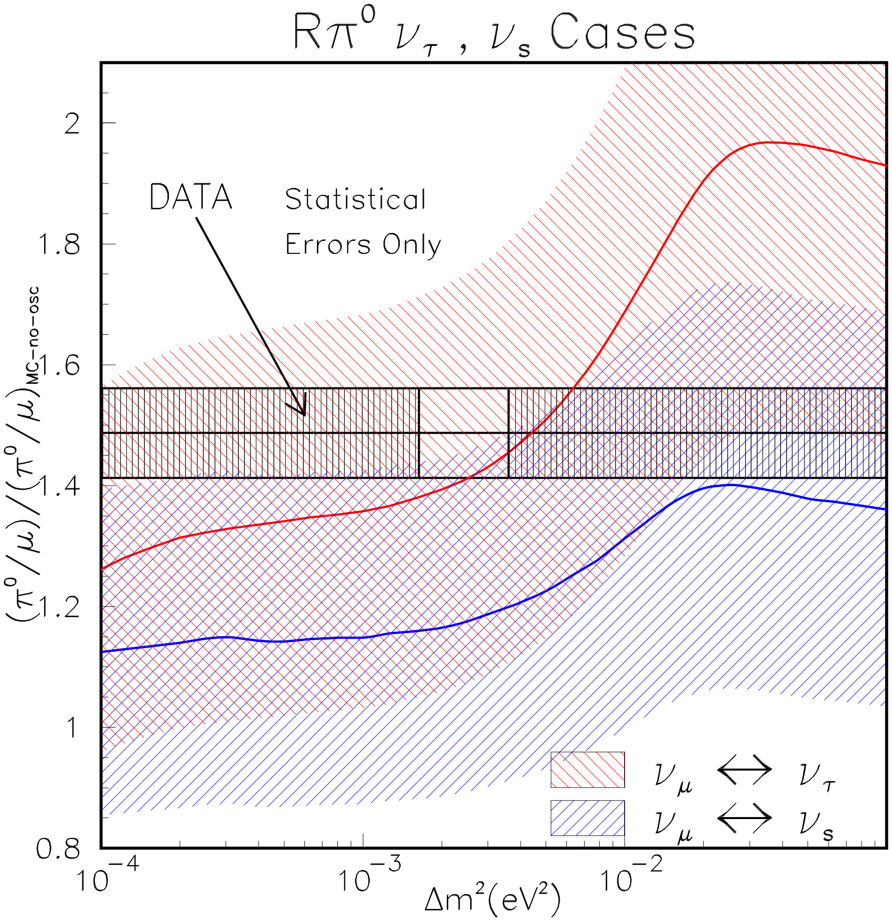

Figure 7.7: The same as Figure 7.6 but without using the result from the 1kt detector. The uncertainties are prohibitive.

Chapter 8

Conclusions and Future

8.1 Conclusions

We have made a measurement of R_{π^0} :

$$R_{\pi^0} \equiv \frac{(\pi^0/\mu)_{data}}{(\pi^0/\mu)_{MC}}.$$

at the 1kt detector with neutrinos from the K2K beam and used it to reduce the systematic uncertainty on a $\nu_\mu \leftrightarrow \nu_\tau$ vs. $\nu_\mu \leftrightarrow \nu_s$ analysis of atmospheric neutrinos.

Our results are more consistent with the $\nu_\mu \leftrightarrow \nu_\tau$ hypothesis and with other results on this topic [32, 98]. The systematic uncertainty on R_{π^0} due to π^0 cross-section and nuclear re-interaction uncertainties is reduced from 23% to 13%.

The evidence is mounting the oscillation solution to the atmospheric neutrino problem is $\nu_\mu \leftrightarrow \nu_\tau$ and not $\nu_\mu \leftrightarrow \nu_s$. Solar neutrinos also seem to favor an active-active mixing between muon or tau and electron-type neutrinos. LSND was an appearance experiment and so also favors active-active mixing. There are two possible ways out of this conundrum. Since solar neutrinos are ν_e and LSND saw $\bar{\nu_e}$ appearance, perhaps the masses of neutrinos and anti-neutrinos are different. This would imply CPT non-conservation. The other way out is the excess the LSND experiment observed is not due to neutrino oscillation.

8.2 The Near Future

Two experiments will clear up this situation in the near future. First, the KamLAND experiment will probe the solar neutrino large mixing angle solution allowed region by searching for $\bar{\nu}_{\mathrm{e}}$ disappearance. Second, the MiniBooNE experiment will probe the LSND allowed region by searching for ν_{e} appearance.

8.3 Future

Many have worked hard for decades trying to detect and measure neutrinos. This labor bore fruit in 1998. The establishment of neutrino oscillation and neutrino mass is, in my view, the most exciting development in particle physics in the last twenty years. With this exciting result, we must energize ourselves for now more than ever, there is much work to do in the field of neutrino physics.

In the "simple" case, the LSND excess is not due to neutrino oscillation and there are three light neutrinos with two Δm^2's and three mixing angles, we must measure all five of these parameters to great precision. In particular, we must nail down the Δm^2's to design future experiments to study CP non-conservation. As experimentalists, we must answer many fundamental questions. We must determine if neutrinos are Dirac or Majorana particles. We must measure the Δm^2's and mixing angles precisely, and we must measure the neutrino masses. These questions will no doubt keep us busy for many years to come.

Bibliography

[1] F. Reines and C.L. Cowan, Nature **178**, 446 (1956).

[2] W. Pauli, in *Open Letter to Radioactive Ladies and Gentlemen* (1930).

[3] Chadwicks and Pauli.

[4] M. Goldhaber, L. Grodzins, A.W. Sunyar, Phys. Rev. **109**, 1015 (1958).

[5] R. Shrock, Phys. Lett. 96B, 159 (1980); R. Shrock, Phys. Rev. D24, 1232, 1275 (1981).

[6] Ch.Weinheimer, presentation at Neutrino 2000.

[7] V.Lobashev, presentation at Neutrino 2000.

[8] Mainz Neutrino Mass Experiment homepage: http://www.physik.uni-mainz.de/exakt/neutrino/en_index.html

[9] K. Assamagan, *et al.*, PSI note R-87-01.2 (2001).

[10] K. Assamagan, *et al.*, Phys. Rev. D **53**, 4065 (1996).

[11] M. Athanas, *et al.*, Phys. Rev. D **61**, 052002 (2000).

[12] R. Barate, *et al.*, Eur. Phys. J. **C2**, 395-406 (1998).n

[13] K. Hagiwara, *et al.* (Particle Data Group), Phys. Rev. D **66**, 010001 (2002).

[14] B. Pontecorvo, Sov. Phys. JETP bf 6, 429 (1957).

[15] R. Davis, Harmer, and K.C. Hoffman, Phys. Rev. Lett. **21**. 1205 (1968).

[16] John Bahcall's homepage: http://www.sns.ias.edu/$\tilde{j}$nb/

[17] J.N. Bahcall, Phys. Rev. Lett. **22**, 300 (1969).

[18] T. Kirsten, *et al.*, Proc. Neutrino '96, (1996).

[19] V.N. Gavrin, *et al.*, Proc. Neutrino '96, (1996).

[20] K.S. Hirata, *et al.*, Phys. Rev. Lett. **63**, 16 (1989).

[21] S. Fukuda, *et al.*, Phys. Lett. B **539**, 179 (2002).

[22] J. Boger, *et al.*, Nucl. Inst. and Meth. A **449**, 172 (2000).

[23] Q.R. Ahmad, *et al.*, Phys. Rev. Lett. **87**, 071301 (2001).

[24] Presentation by M. Vagins at ICHEP 2002, http://www.ichep02.nl/index-new.html .

[25] IMB atmospheric neutrinos. D. Casper *et al.*, Phys. Rev. Lett. **66**, 2561 (1991). R. Becker-Szendy *et al.*, Phys. Rev. D **46** 3720 (1992).

[26] K.S. Hirata *et al.*, Phys. Lett. B **205**, 416 (1988); K.S. Hirata *et al.*, Phys. Lett. B **280**, 146 (1992).

[27] M. Aglietta *et al.*, Europhys. Lett. **8**, 611 (1989).

[28] K. Daum *et al.*, Z. Phys. C **66**, 417 (1995).

[29] W.W.M Allison *et al.*. Phys. Lett. **B391**(1997) 491.

[30] A. Aguilar, *et al.*, Phys.Rev. D **64**, 112007 (2001).

[31] The LEP collaboration and the LEP electroweak working group. J. Dress *et al.*, Lepton and Photon Interaction at High Energy, Rome, Italy, July, 2001.

[32] S. Fukuda, *et al.*, Phys. Rev. Lett. **85**, 3999 (2000).

[33] K. Ishihara, PhD. thesis, University of Tokyo, (1999).

[34] T. K. Gaisser and M. Honda, to be published Ann. Rev. Nuc. and Part. Sci. **52**, December 2002.

[35] Webber WR, Golden RL, Stephens SA. *Proc. 20th Int. Cosmic Ray Conf.* 1:325 (1987)

[36] Seo E-S, et al. *Astrophys. J.* 378:763 (1991)

[37] Pappini P, et al. *Proc. 23rd Int. Cosmic Ray Conf.* 1:579 (1993)

[38] Bellotti R, et al. *Phys. Rev.* D60:052002 (1999)

[39] Boezio M, et al. *Astrophys. J.* 518:457 (1999)

[40] Menn W, et al. *Astrophys. J.* 533:281 (2000)

[41] Sanuki T, et al. *Astrophys. J.* 545:1135 (2000)

[42] Alcarez J, et al. *Phys. Lett.* B490:27 (2000)

[43] Ryan MJ, Ormes JF, Balasubrahmanyan VK. *Phys. Rev. Lett.* 28:985, E1497 (1972)

[44] Asakamori K, et al. *Ap. J.* 502:278 (1998)

[45] Ivanenko IP, et al. *Proc. 23rd Int. Cosmic Ray Conf.* 2:17 (1993)

[46] Apanasenko AV, et al. *Astropart. Phys.* 16:13 (2001)

[47] Kawamura Y, et al. *Phys. Rev.* D40:729 (1989) (1989)

[48] Asaoka Y, et al. *Phys. Rev. Letters* 88:51101 (2002)

[49] Cutler DJ, Groom DE. *Astrophys. J.* 376:322 (1991)

[50] M. Honda, *et al.*, Phys. Rev. D **52**, 4985 (1995).

[51] V. Agrawal, *et al.*, Phys. Rev. D **53**, 1314 (1996).

[52] S.H. Ahn, *et al.*, Phys. Lett. B **511**, 178 (2001).

[53] H. Sato, Proc. Particle Accelerator Conference (1999); K. Takayama, ICFA Beam Dynamics Newsletter No.20, (1999).

[54] A. Suzuki *et al.*, Nucl. Inst. and Meth. A **329**, 299 (1993).

[55] Honda, *et al.*, Phys. Rev. D **52**, 4985 (1995); G. Barr *et al.*, Phys. Rev. D **39**, 3532 (1989); V. Agrawal *et al.*, Phys. Rev. D **53**, 1314 (1996);

[56] C.H. Llewellyn Smith, Phys. Rep. **3** (1972) 261.

[57] D. Rein and L.M. Seghal, Ann. Phys. **133** (1981) 79.

[58] D. Rein and L.M. Seghal, Nucl. Phys. **B223** (1983) 29.

[59] M. Nakahata, *et al.*, J. Phys. Soc. Jpn. **55** (1986) 3786.

[60] "GEANT Detector Description and Simulation Tool", CERN Program Library W501 3 (1994).

[61] T.A.Gabriel *et al.*, ORNL/TM-11185; C.Zeitnitz and T.A.Gabriel, Nucl. Instr. and Meth. A **349**, 106 (1994).

[62] H.J. Grabosch *et al.*, Z.Phys. C **41**, 527 (1989).

[63] V. Bernard, L. Elouadrhiri and U.G. Meissner, J. Phys. G **28**, R1 (2002).

[64] S. Barish *et al.*, Phys. Rev. D **16**, 3103 (1977).

[65] S. Bonetti *et al.*, Nuovo Cimento **38**, 260 (1977).

[66] M. Pohl *et al.*, Nuovo Cimento **26**, 332 (1979); N.Arimenise *et al.*, Nucl. Phys. B **152** 365 (1979).

[67] S. Belikov *et al.*, Z. Phys. **320**, 625 (1985).

[68] C.H. Albright *et al.*, Phys. Rev. D **14**, 1780 (1976).

[69] L.A. Ahrens *et al.*, Phys. Rev. Lett. **56**, 1107 (1986).

[70] G. Radecky *et al.*, Phys. Rev. D **25**, 116 (1982).

[71] T. Kitagaki *et al.*, Phys. Rev. D **34**, 2554 (1986).

[72] W. Lerche *et al.*, Phys. Lett. **4**, 510 (1978).

[73] D. Rein, Z. Phys. C **35**, 43 (1987).

[74] N.G. Kelkar, *et al.*, Phys. Rev. C **55**, 1964 (1997).

[75] T. Sjostrand, CERN-TH.7112/93 W5035/W5044.

[76] M. Gluck, E. Reya, and A. Vogt, Z. Phys. C **67**, 433 (1995).

[77] S.J. Barish *el al.*, Phys. Rev. D **17**, 1 (1978).

[78] H. Sarikko, Neutrino 1979, 507 (1979).

[79] S. Barlag *et al.*, Z. Phys. C **11**, 283 (1982).

[80] Paul Musset and Jean-Pierre Vialle, Phys. Rep. C **39**, 1 (1978).

[81] J.E. Kim *et al.*, Rev. Mod. Phys. **53**, 211 (1981).

[82] L.L. Salcedo *et al.*, Nuc. Phys. A **484**, 557 (1988).

[83] G. Rowe *et al.*, Phys. Rev. C **18**, 584 (1978).

[84] B.R.Martin and M.K.Pidcock, Nuc.Phys. B **126**, 266 (1977).

[85] B.R.Martin and M.K.Pidcock, Nuc.Phys. B **126**, 285 (1977).

[86] J.S. Hyslop *et al.*,Phys. Rev. D **46**, 961 (1992).

[87] D.A. Sparrow, Proc. of the Conf. on the Intersection of Particle and Nuclear Physics, 1019 (1984).

[88] H.W. Bertini, Phys. Rev. C **6**, 631 (1972).

[89] Lindenbaum, *et al.*, Phys. Rev. **105**, 1874 (1957).

[90] M. Nakahata, *et al.*, J. Phys. Soc. Jap. **55**, 3786 (1986).

[91] *The ZEBRA System*, CERN Program Library Long Writeups Q100/Q101.

[92] Y. Fukuda, *et al.*, Phys. Lett. B **433**, 9 (1998); Phys. Lett. B **436**, 33 (1998).

[93] *Machine Vision : Theory, Algorithms, Practicalities* (Academic Press, San Diego, 1997).

[94] M. Shiozawa, PhD. thesis, University of Tokyo, (1999).

[95] D. Casper, Proc. NuInt '01 to be published. Available from: http://neutrino.kek.jp/nuint01/

[96] NuInt '01, http://neutrino.kek.jp/nuint01/

[97] Y. Fukuda, *et al.*, Phys. Rev. Lett. **81**, 1562 (1998).

[98] M. Ambrosio *et al.*, Phys. Lett. B **517**, 59 (2001).